On Packaging of MEMS

Simulation of transfer moulding and packaging stress and their effect on a family of piezo-resistive pressure sensors.

by

Rudolf H. Krondorfer

ACKNOWLEDGMENTS

PREFACE

Micro Electro Mechanical Systems (MEMS) produced to date include IR detectors, accelerometers, pressure sensors, micro lenses, actuators, chemical sensors, gear drives, RF devices, optical processor chips, micro robots and devices for biomedical analysis. The track for tomorrow has already been set and products like 3D TV, physician on a chip, lab on a chip, micro aircraft and food safety sensors will be developed when the technology matures and the market is ready.

Todays MEMS fabrication is typically based around a silicon substrate and borrow batch fabrication processes from the IC industry. Many of the developed MEMS products have never left a laboratory environment because they are fragile in the macro environment. The way to deal with this is to provide proper packaging so that they can be handled. This poses one of the major challenges in the MEMS industry. Not many packaging techniques have been commercially developed for MEMS and companies that have overcome the packaging problems very seldom reveal their packaging techniques. Functional problems that could be associated with a MEMS structure are often amplified by the package. The reason for this is often associated with packaging stress. Packaging stress related problems is what has kept many promising products from emerging on the market. Even the commercially available pressure sensors and accelerometers have packaging stress problems, but most of them have been overcome. A first step towards solving these challenges is to localise, quantify and understand the critical packaging stresses that act in a packaged MEMS device.

The goal of this work was to understand how packaging stresses act in a plastic moulded MEMS chip. The work has been threefold; simulation of transfer moulding, static stress analysis of the plastic capsule after moulding and modelling of the piezo-resistive behaviour of a MEMS pressure sensor.

This dissertation is divided into 9 chapters. **Chapter 1** introduces the concept of level-0 and level-1 packaging and looks at different techniques of obtaining the different packaging levels. It introduces the Small Outline Package (SOP) which is the package that has been simulated in this dissertation.

Chapter 2 gives the background in the theory that has been used to complete this work. It starts by discussing the chemistry and mechanics of thermosetting polymers. Then the rheological behaviour of Epoxy Moulding Compounds (EMC) in a transfer moulding process is discussed.

The experimental results from the thermomechanical material characterisation of the EMC are presented in **Chapter 3**. The material was found to have a T_g of 130^oC and coefficient of linear expansion of $8\Delta 10^{-6}$ /^{o}C and $31\Delta 10^{-6}$ /^{o}C below and above T_g respectively. It was further found that the material showed linear viscoelastic behaviour. Stress relaxation tests were run to obtain the relaxation coefficients needed for accurate modelling. The material was found to behave in a thermo rheologically simple manner and the WLF shift function was used to describe the time-temperature superposition principle.

Chapter 4 addresses the applicability of the plastic processing simulation code, C-Mold, for simulations of MEMS packaging in a SOP. It was found that the 2.5D simulation technique used by the software was inadequate for simulating the polymer filling of the SOP in question. This conclusion was drawn because 3D flow effect were observed in the moulding cavities. The cause for the 3D flow effect was the height of the SOP which was relatively large in order to accommodate for the MEMS device. However, the software proved to be very useful for balancing the runner system.

Chapter 5 starts with the development of a novel method for calculating the accurate piezo-resistance for implanted silicon piezo-resistors. The method let each finite element in a piezo-resistor region represent one resistor in a resistor network. The total resistance was then found by simple resistor summation. This method was then utilized on a silicon diaphragm pressure sensor, which had four piezo-resistors implanted into the top surface. The resistors on the diaphragm formed a Wheatstone bridge and the change in piezo-resistance, as a result of applied pressure and hence change in the stress field, was transformed into an electrical signal by proper post processing. The model was built from the design specifications of a commercially manufactured die. The results were compared to the production measurements and matched the data within one standard deviation. It was found that the level-0 package had an effect on the output signal. This work is believed to be the first to report an estimation of the distortion effect that a level-0 package has on a sensor signal with temperature.

Chapter 6 presents the model of the complete MEMS pressure sensor component encapsulated by EMC in a SOP. The EMC was treated as being elastic and temperature dependent. The method that was developed and calibrated in Chapter 5 was used as an indirect measure of the accuracy of the FEM model. It was evident that the package had a profound effect on the sensor signal. This was consistent with the actual measured data. The match of the signal data was not satisfactory. The signal values for two of the four service temperatures lay outside 3 standard deviations of the experimentally measured results. The estimated sensitivity of the die also fell outside 3 standard deviations for three of the four service temperatures.

A special vector plot was developed to understand how the pressure, or packaging stress, from the EMC effected the signal and sensitivity of the sensor die. The numerical simulations were done assuming a stress free temperature of 175°C, the moulding temperature. The packaging stress was found to increase with decreasing temperature. This was the effect of the subsequent increase in $\div T$ as the service temperature decreased.

The signal at zero pressure was found to shift as a function of temperature. This was caused by the packaging stress and a corresponding stress-field-shift on the diaphragm. The origin for this shift was an uneven packaging stress between the front and the back side of the sensor die. At -7°C, the pressure on the front and the back was 30 and 20MPa respectively. This caused an uneven bending moment on the membrane long sides and resulted in a shift in the stress field.

Chapter 7 elaborated the model one step further by treating the EMC as a viscoelastic material. The result of using the viscoelastic material model showed a reduction in the packaging stress due to stress relaxation. Viscoelastic materials are temperature and strain-history dependent. It was therefore necessary to run the model through the same processes posed by the manufacturing of the MEMS and SOPs. These included a set of thermocycles between -40°C and 125°C before the signals as a function of temperature and pressure were taken. The thermocycles were found to have a positive effect on signal shifting. Less signal distortion was seen with more cycles. The estimated and measured signal- vs. temperature-values matched within two standard deviations. The estimated sensitivities did not match the experimental measurements any better than those obtained for the elastic case. It was also found that sensitivity was nearly independent on packaging stress, but significantly dependent on pressure loading conditions.

The use of the viscoelastic model gave an improvement in simulated signal accuracy over the elastic model. It became clear that the EMC had to be treated as a viscoelastic material.

Chapter 8 concerned the change in material properties of the EMC and the impact this had on the FEM results. It was found that the behaviour of the MEMS pressure sensor was greatly affected by such changes.

Chapter 9 present the concluding remarks of this study.

LIST OF PUBLICATIONS

Conferences

1. Krondorfer, R. H. and Ullvensøen, J. H., "Simulation of Transfer Molding", *Proc. of 38th IMAPS Annual Conference,* Oslo, pp. 304-310, 2001
2. Krondorfer, R. H. and Lommasson, T. C., "Direct Calculation of Sensor Performance in a FEA Model," *Proc. 1st Sensors Conf.,* Orlando, FL, pp. 2013-2019, June 2002.
3. Krondorfer, R. H., Kim, Y. K. and Lommasson, T. C., "FEA simulation of package stress in transfer molded MEMS pressure sensors", *Proc. of EuroSIME2003,* Aix-en-Provence, France, pp. 165-169, 2003.

Journals

4. Krondorfer, R. H., Kim, Y., Kim, J. and Lommasson, T. C., "FEA simulation of package stress in transfer molded MEMS pressure sensors", **submitted on 30th of September 2003 for publication in Elsivier's Micro-electronics Reliability Journal.**

CONTENTS

CHAPTER 1

INTRODUCTION TO MEMS PACKAGING

Micro Electro Mechanical Systems (MEMS) has been called the second silicon revolution, with benefits far beyond what has been seen with the first silicon revolution in integrated circuits [8]. Packaging has been one of the main inhibiting factors for this revolution. MEMS are often application specific, requiring custom packages that are not commercially available. Devices may also need media compatible packages that can protect the device from harsh environments in which the MEMS device may operate. Packaging techniques used in MEMS borrow heavily from those developed for microelectronics. Similarities include hermeticity and chip-level integration techniques such as Multi-Chip-Modules (MCMs) [7]. Differences include a unique set of failure modes due to the mechanical nature of MEMS that are still not very well understood [5]. To date, most of what is known about MEMS packaging remains proprietary and published literature is scarce. Although the challenges of MEMS packaging has been known for some time, little published research has been achieved to compile data and work towards meeting these challenges [8]. A disproportionality exists between the resources spent on packaging of MEMS and the time spent on MEMS packaging research. The cost of MEMS packaging typically account for a significantly amount of the production price of the device. Figures as high as 75-80% has been quoted [9].

New devices are developed continuously offering great promises for miniaturization of existing actuators and sensors, as well as novel devices not previously possible to manufacture. Currently it is the problems associated with the packaging of these devices that is limiting their market application. The commercially available pressure sensors and accelerometers are devices that has been relatively simple to package.

There is a philosophical difference between the packaging of ICs and the packaging of MEMS. The purpose of IC packaging is to provide physical support for the chip, provide an electrical interface to activate chip(s) in the system, supply signal, power and ground interconnections and allow proper heat dissipation [10]. Also a package must effectively isolate the chip physically from its environment. One of the fundamental differences between microsystem packaging and IC packaging is that the microsystem generally interact with the environment in which it is placed [11]. An additional constraint imposed on the microsystem is that it must protect the environment from its own materials and operation, so that no undesirable reaction with or contamination of the environment occurs [3]. This is especially important for sensors used in biomedical [1], pharmaceutical and food processing [2] applications.

IC packaging technology has gone from dual-in-line packages (DIPs) in the late 1970s to quad flat packages (QFPa) in the 1980s and ball-grid arrays in the 1990s (Figure (1.1))

Smaller Size

Higher Pin Count

Smaller Size, Weight

SOP

SOJ

S-SOP

TSOP

QFJ
(PLCC)

Fine
Pitch
Bonding

QFP

TQFP

TAB

PIH 1000

BGA

CSP

MCM

DIP/PGA

SLIM

Year   1970s   1980s   1990s   2000-2010
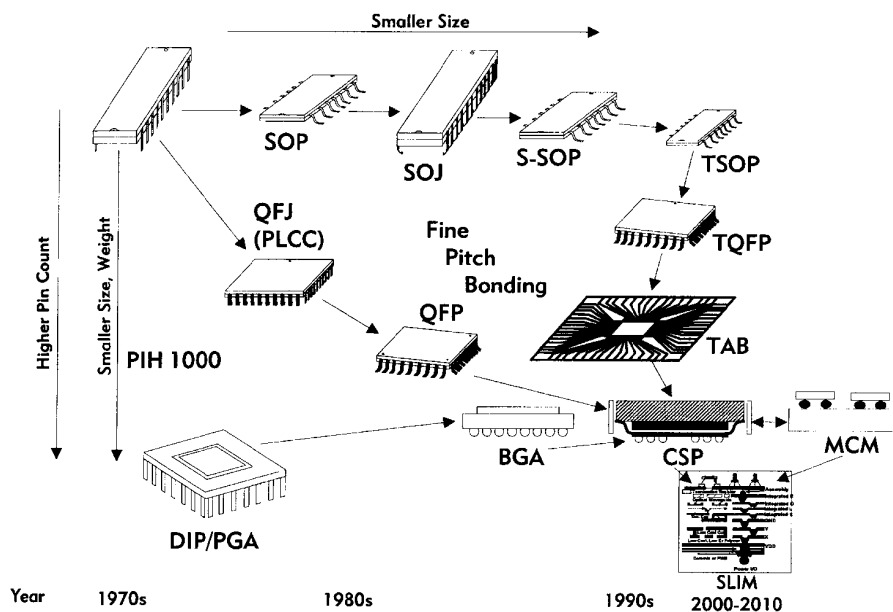
Figure 1.1   Single-chip package evolution leading to multichip packaging [74].

Commercially successful MEMS products are packaged in either a ceramic, metal can, or a plastic-package. This puts MEMS packaging back to the 1970s on the chart in Figure (1.1). This can be an advantage. The technology is mature, well understood and thoroughly tested. There are, however, new problems associated with MEMS that were never brought up or never critical for IC packaging. Many of these problems can be avoided by using ceramic, or metal-can packages. These packages perform well and are always the favourable choice from a reliability point of view. But they are only viable for low-volume production. Ceramic packages and metal-can packages are too expensive to be used in high-volume production. A cheaper way to package mass produced components is to use the well established technique of transfer moulding. But transfer moulding has some drawbacks. It is a harsh process and it uses a thermoset polymer. The polymer has a high thermal expansion coefficient and a relatively high modulus. This can result in high residual stresses after encapsulation and subsequent cooldown to room temperature. These residual stresses calls for the MEMS devices to be somehow protected before the transfer moulding. This protection is often achieved through a so called level-0 package. The level-0 package has multiple purposes and is introduced and discussed in the next section.

It is vital to understand the whole packaging process and the interaction of all the materials in the package to be able to design successful functioning packages.

1.1 OVERVIEW OF MEMS PACKAGING AND VARIOUS MEMS PACKAGES

It has become increasingly popular to divide MEMS packaging into two levels, level-0 and level-1. Level-0 is used to describe the package that creates the controlled environment surrounding the fragile micro mechanical parts, and level-1 is used to describe the traditional package containing the level-0 package and providing interconnects to the outside world.

2

1.1.1 Level-0 Packaging

The level-0 package is also often needed, because the micro mechanical parts often require hermetically sealed cavities which enables control of the ambient (gas pressure and gas composition.) These are factors that can be critical for the performance of the device [13]. Also, a controllable ambient allows tuning of the device performance. Hermeticity plays an important role in the reliability and the long-term drift characteristics of the device. In order to minimize damage during handling, the cavity is preferably realized at the same time as the device is fabricated, i.e. at wafer level [12]. Wafer level packaging is conveniently referred to as the level-0 package.
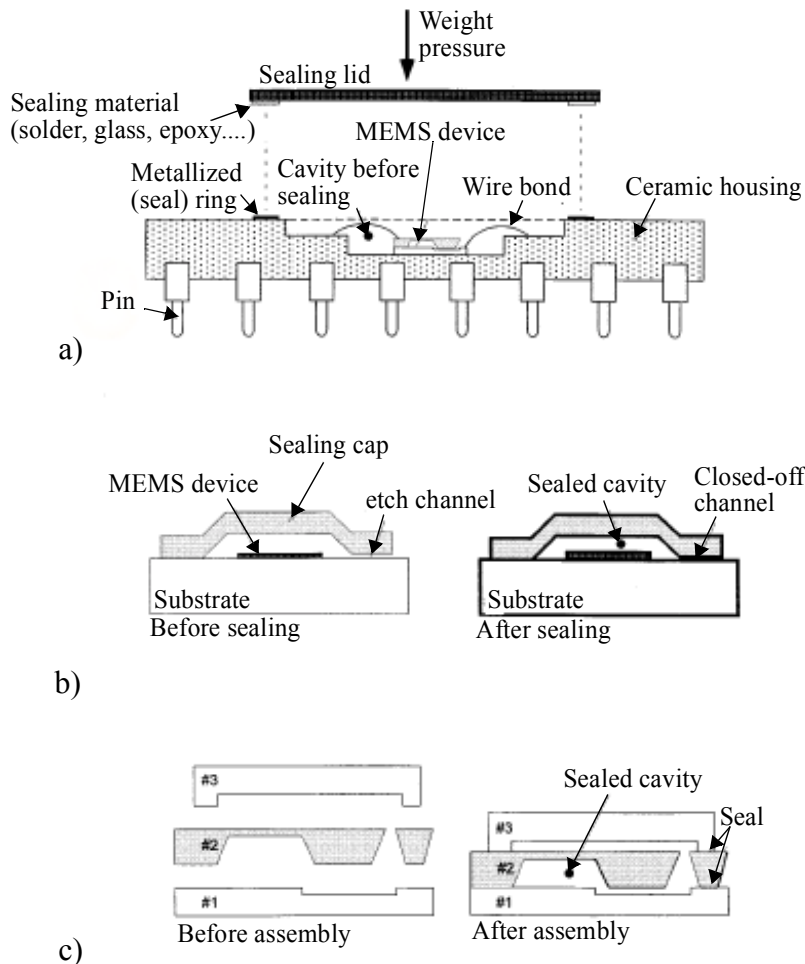
Figure 1.2   Examples of methods to realize hermetically sealed cavities based on: (a) lid sealing for ceramic (and metal can) packages [14], [15], (b) surface micromachining using reactive sealing techniques [16], [20], and (c) wafer stacking [17], [18], [21], [30].

Three approaches for level-0 packaging will be introduced here. The first approach relies on wafer bonding, the second approach is based on surface micromachining techniques, and the third approach is the Indent Reflow Sealing (IRS) technique. In the second approach, the cavity contains an access channel for the sacrificial layer etchant, as illustrated in Figure (1.2)b. After completion of the sacrificial layer etch, the channel is closed, thereby sealing the cavity.

The general idea of the wafer bonding approach is to cap the sensor or actuator structure with another chip in which a cavity is made or a standoff ring is implemented. In other words, a stack of chips or wafers is built, as illustrated in Figure (1.2)c. This package technique was used to package the MEMS devices in this work and is often called a glass-Si-glass tri-stack. For the bonding of one chip (or wafer) to the other chip (or wafer) several methods exist: anodic bonding of glass to silicon [18], [19], [23], silicon direct bonding (SDB) [23], [24], [25], glass direct bonding [26], (eutectic) solder bonding [17], [21], [27]- [28], and bonding using low-temperature glasses ("frit" seals) [29], [30] or polymer adhesives [31], [32]. The process and materials employed determine the hermeticity and controllability of the cavity ambient. The third approach for level-0 packaging, IRS, has been developed with the aim to remove all the drawbacks of the two aforementioned methods [12]. The process flow in essence resembles the flow shown in Figure (1.2)c, thereby implementing a solder joining technique holding all of the aforementioned attributes.
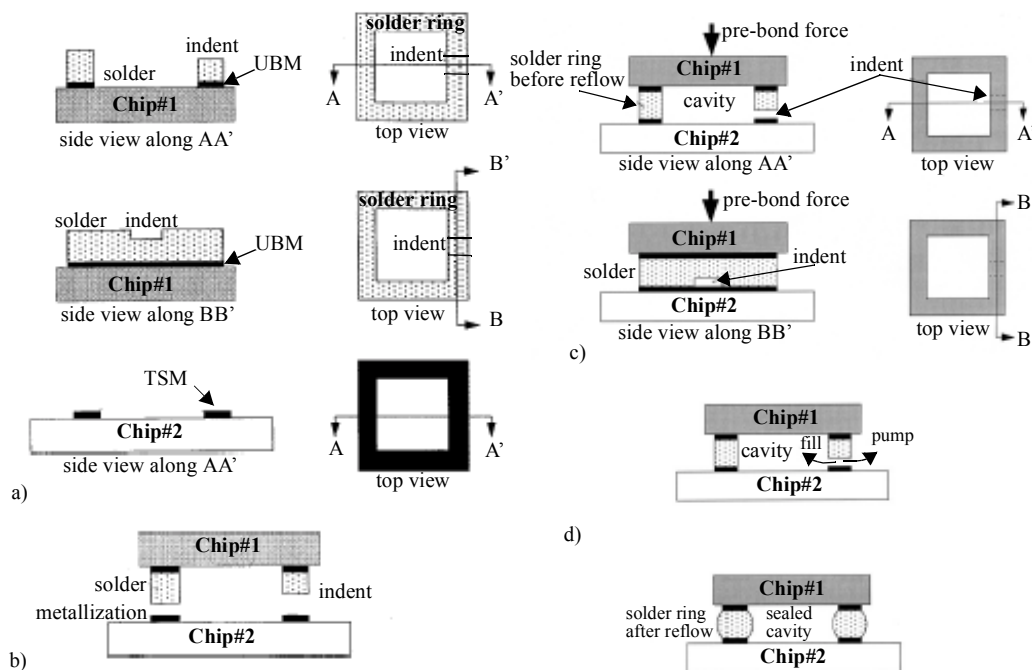
Figure 1.3 Generic process flow of the IRS process. (a) Preparation of chip#1 with under bump metallization (UBM) and solder layer with indent and chip#2 with the top surface metallization (TSM). (b) After pretreatment and flip-chip alignment. Generic process flow of the IRS process. (c) After pre-bonding (or sticking) of the chips on a flip-chip alignment and bonding apparatus. (d) In reflow oven: purge, pump vacuum, and (optionally) fill with desired gas. (e) After solder reflow and sealing [4].

All these level-0 packages are usually mounted on a leadframe for encapsulation or mounted on a printed circuit board for glob top encapsulation.

1.1.2 Level-1 Packaging

The level-1 package is often just a conventional electronic plastic package consisting of lead-frame, die-bonding, wire-bonding and moulding to provide a housing for handling, mounting and board level interconnection.

It is also possible to create the controlled environment, for a MEMS device, at packaging level-1. The different techniques include ceramic packages where encapsulation is achieved through a lid-sealing process of the cavity containing the MEMS device (and/or electronic) chip [14] (Figure (1.2)a). Other approaches are based on the sealing of a metal (can) package [15]. Cavity formation during level-1 packaging is an established method and allows a certain flexibility with respect to the composition of sealing gas and sealing pressure, but on the other hand, requires the use of expensive ceramic or metal can packages.

The low cost plastic package that this dissertation looks at is achieved through transfer moulding. For the MEMS devices to sustain the harsh moulding process, they have been level-0 packaged at wafer level. Packaging at wafer level protects the MEMS device from exposure to contamination during wafer dicing and subsequent cleaning. The level-0 package should be designed and fabricated at the same time the device is fabricated.

1.2 TRANSFER MOULDED PLASTIC ENCAPSULATED DEVICES

MEMS devices are sensitive to the residual stresses that develop during curing and cooldown of the polymer after transfer moulding. It is important to understand how these stresses interacts with the MEMS device to be able to reduce and/or control them by various means. The residual stresses are often a function of temperature so that sensors designed to operate in thermally changing environments need to be designed to operate over a range of stress values.

The packaging of a MEMS device is more complex than it was for its forerunner, the IC. Often a MEMS package actually contains both a transducer or actuator and an IC to handle the sensor signal. This in turn means that MEMS packaging faces the same problems that IC packaging once did plus, it faces problems that are new and unique to the MEMS part of the system.

The packaging of microsystems have been reviewed in multiple papers over the years, including [3], [6], [8], [64], [65] and [66].

Many papers have taken up the issues of packaging stress from plastic encapsulation. A series of papers were published on the residual stresses of plastic quad flat packages (PQFP) [56], [67], [68]. The papers concerned the stress analysis of the PQFP's by using FEM. The thermo-mechanical stresses were analysed and compared to measured data. It was suggested that a side buffer on the IC made from a soft material, like a silicon gel, could significantly reduce packaging stress in that particular package. Another result that came through was that cure shrinkage had to be considered as it accounted for a significant amount of the total shrinkage of the resin. This was not an issue for this work because the moulding compound used exhibited insignificant chemical shrinkage.

The three papers above used simple cooldown analysis from moulding temperature to room temperature as the loading condition. A stress free condition was assumed at the moulding temperature. The materials were all treated as linear elastic. Wang et. al [69] took the analysis technique two steps further by introducing temperature dependent material properties and a full process model. The epoxy encapsulant was treated as elastic-plastic. By doing so, Wang et. al found that larger and more realistic stresses were calculated by introducing a full process model rather than by assuming one stress free temperature for the whole structure.

Using correct constitutive behaviour and properties of the materials are essential for accurate modelling. Some work has been done to look at the constitutive behaviour of epoxy moulding compounds. Researchers in Japan showed that the material behaves viscoelastically with a strong temperature dependence [57], [71].

Measured viscoelastic material properties for EMCs was reported by Harper et al. [80] and Kenner et al. [81]. The EMCs were found to behave differently from "regular" polymers. A non conventional shift function (conventional being shift functions like WLF & Arrhenius) was obtained when the time-temperature superposition principle was used. Harper et al. [80] could not describe the shift by one single conventional shift function, but used a combined WLF and Arrhenius relation.

Li and Tseng published a paper on guidance for designing packages with low stress and low deformation [33]. The paper considered different gluing techniques, glob topping, geometrical issues and the epoxy moulding compound. This is the only paper found by the author of this dissertation that treats packaging stress of thermoset encapsulated microsystems, both theoretically and experimentally. The paper was published in january 2001 and sited no reference to other work on similar topics.

1.3 THE PLASTIC PACKAGE STUDIED IN THIS WORK

The MEMS package studied in this dissertation contains a level-0 packaged pressure sensor and an Application Specific Integrated Circuit (ASIC). The level-0 package is a glass-Si-glass tri stack anodically bonded together at high temperature. The micro mechanical structure was formed in the silicon. The level-1 package was the Small Outline Package (SOP) which is a surface mountable version of the well known Dual Inline Package (DIP). Figure (1.4) shows a schematic of the MEMS.
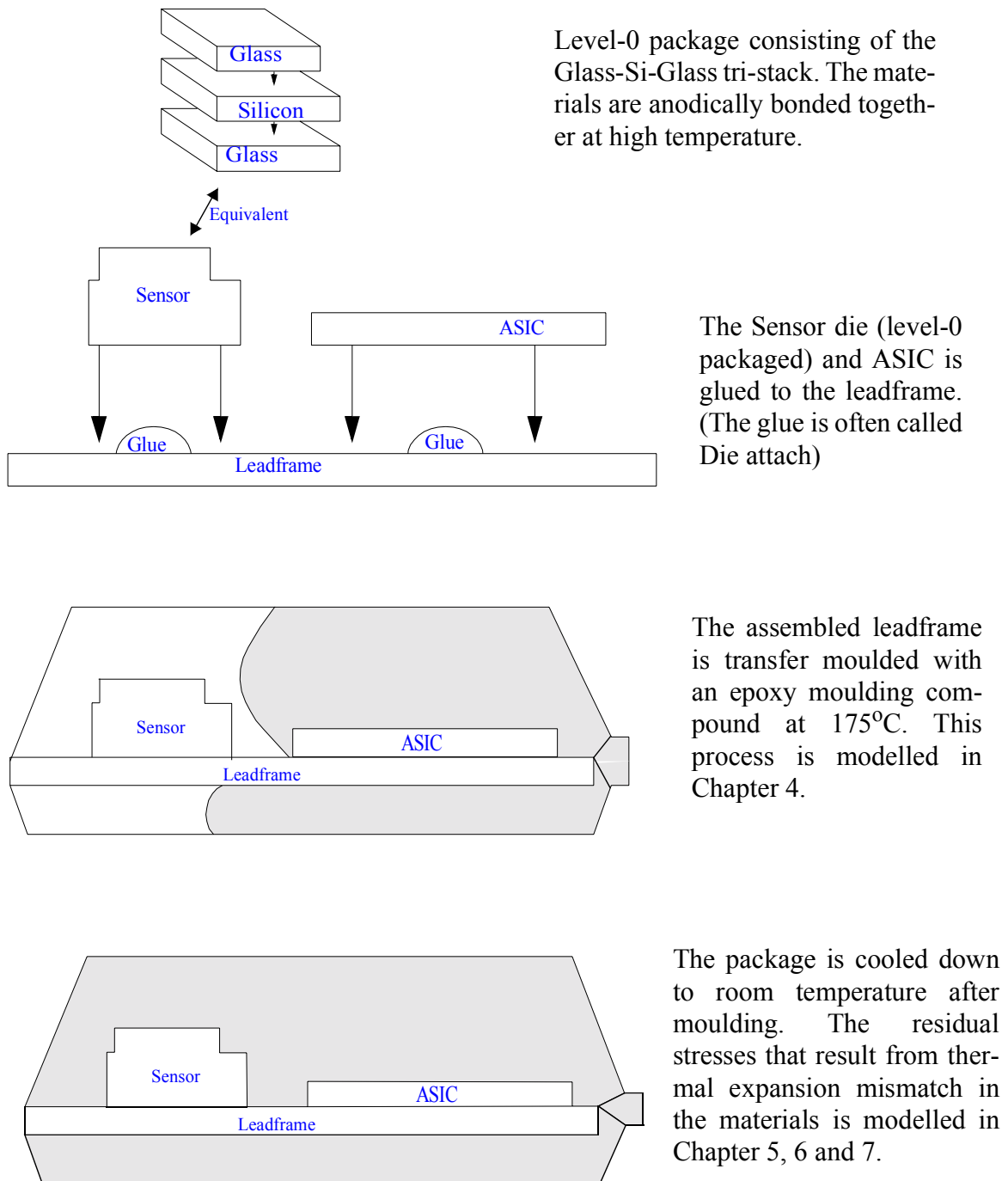
Level-0 package consisting of the Glass-Si-Glass tri-stack. The materials are anodically bonded together at high temperature.

The Sensor die (level-0 packaged) and ASIC is glued to the leadframe. (The glue is often called Die attach)

The assembled leadframe is transfer moulded with an epoxy moulding compound at 175$^{\rm o}$C. This process is modelled in Chapter 4.

The package is cooled down to room temperature after moulding. The residual stresses that result from thermal expansion mismatch in the materials is modelled in Chapter 5, 6 and 7.

Figure 1.4   Schematic of the MEMS studied in this dissertation.

BASICS

The goal of the work presented in this dissertation was to predict and quantify the stresses that act on a transfer moulded encapsulated MEMS device. The encapsulation material used is a thermosetting Epoxy Moulding Compound (EMC). The compound in this work is based on a biphenyl epoxy resin system, see Appendix E. This chapter gives an overview of the theoretical foundations needed to appreciate and follow the work.

2.1 CURING OF THERMOSETTING POLYMERS

Thermosetting resins are those that change irreversibly under the influence of heat from a fusible and soluble material into one which is infusible and insoluble through the formation of a covalently crosslinked, thermally stable network [34].

The use of thermoset materials in plastic packaging takes advantage of their low initial viscosity and their ability to sustain very high temperature without flow when polymerized. These materials can withstand high temperatures, e.g. during soldering, without gross deformation.

Figure (2.1) below shows a schematic 2-D representation of thermoset curing, starting with A-stage monomers (a); proceeding through simultaneous linear growth and branching to a B-stage material below the gel point (b); continuing with the formation of a gelled but incomplete crosslinked network (d); and leading finally to the fully cured C-stage thermoset (c).
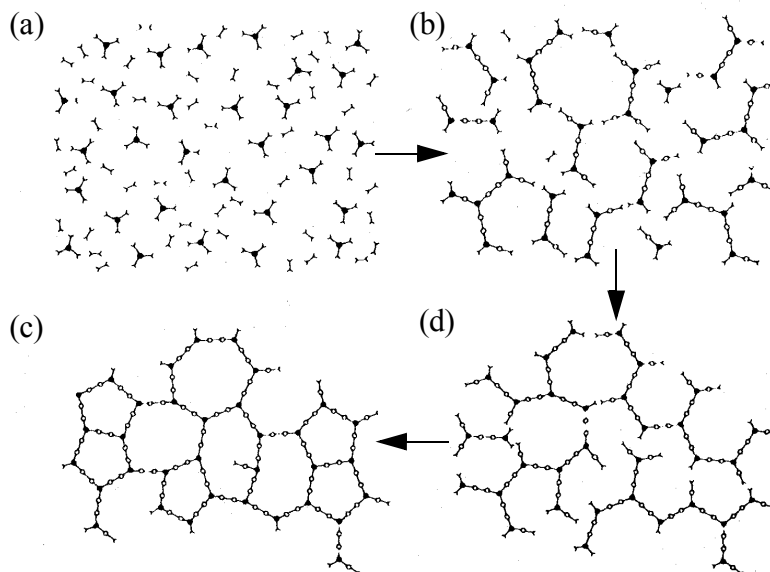
Figure 2.1   Schematic 2-D curing representation of thermoset cure [35]

The degree of chemical conversion at which the three-dimensional structure first appears is known as the *gel point* and the phenomenon is known as *gelation* [36].

2.1.1 Chemical Considerations

As the reaction proceeds, the molecular weight of the growing chains increases rapidly, promoting a rapid increase in viscosity. In this regime, the reaction is chemically-controlled. At the gel point, cross-linking occurs, and the polymer chains are irreversibly transformed from a viscous liquid to a viscoelastic gel. Gelation conditions are dependent on effective functionality, reactivity and reactant stoichiometries. Prior to gelation, the sample is still soluble in suitable solvents, but after the gel point is reached, the network will not dissolve, but swells as it imbibes the solvent. Advances in the glass transition temperature of the growing polymer chains occur simultaneously as the network crosslink density increases during cure. Should the glass transition temperature at any point become greater than the cure temperature, the mobility of the growing chains is severely depressed and conversion to the network structure ceases, i.e. reaction becomes diffusion-controlled. This process is known as vitrification, and is marked by the formation of a partially cured glassy network whose glass transition temperature is coincident with the maximum cure temperature achieved. Vitrification is a reversible transition which may occur at any point during the curing process and leads to a decrease in the reaction rate. Typically, a post-cure step is performed at a higher temperature to ensure that complete curing and the ultimate glass transition temperature are attained.

2.1.2 Mechanical Considerations

During curing, the material transforms from a viscous fluid (low shear stiffness) in its uncured state, to a viscoelastic or elastic solid (with high shear stiffness) in its fully cured state. Significant residual stresses might develop on cool-down to room temperature. The magnitude of the stresses depends on, among other factors, a reduction in specific volume (cure, chemical or polymerization shrinkage), viscoelastic stress relaxation effects and the actual process parameters. In addition, the exothermic heat generated during polymerization and shear heating during processing could result in complex temperature and cure gradients, and might even raise the internal temperatures to levels that might induce material degradation.

Illustrated in Figure (2.2) is a simplified representation of the changes in specific volume and stiffness during cure.
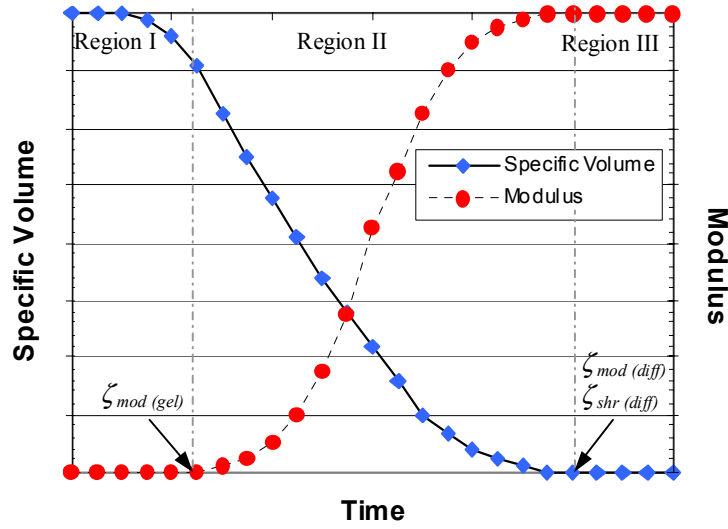
Figure 2.2   Cure shrinkage and Modulus development during cure [42].

The curing process is separated into three distinct regions [42]. In Region I, the polymer is in the B-stage condition, uncured and assumed to behave as a viscous fluid (negligible stiffness). Region II denotes the curing stage, where a significant increase in modulus and a reduction in specific volume (cure shrinkage) begins to occur. The modulus development is assumed to begin at the gel point, denoted by $\zeta_{mod\ (gel)}$, and is assumed to be complete once the polymer is fully cured or diffusion limitation inhibits its further modulus development at $\zeta_{mod\ (diff)}$. The polymer cure shrinkage is assumed to behave similarly, with the actual change in specific volume occurring until it becomes diffusion controlled, $\zeta_{shr\ (diff)}$. Physical aging has not been taken into account here. The justification for this is that physical aging is a process of rearrangement of the molecular structure over time. In the present study, where the material was subjected to repeated thermocycles reaching above T_g, in the relatively short time scale, physical aging will not contribute to the shrinkage. In general, the regions for modulus development and cure shrinkage do not coincide, and are unique for each thermosetting system. Region III marks the end of the curing process and no further chemical shrinkage occurs. In this region, the polymer exhibits the traditional viscoelastic behaviour at higher temperatures and approaches elastic behaviour at lower temperatures. Therefore, the only mechanism contributing to changes in the specific volume are considered to be thermal expansion effects. The total curing shrinkage as a function of temperature is shown in Figure (2.3). The figure corresponds to a complete moulding cycle. The sample at point A is a mixture of resin and curing agent at room temperature. The sample is heated to moulding temperature and begins to react at point B. The moulding and in-mold-cure is finished at point C. From point C, the sample is cooled to room temperature (point D) through the glass transition, T_g, (point E).
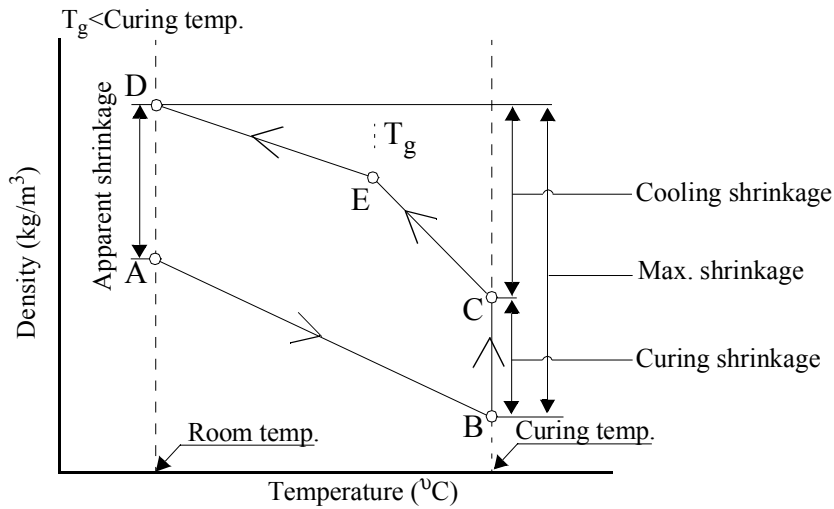
Figure 2.3   Density change in curing cycle of epoxy resins [63].

An important parameter of polymeric materials, both thermosets and thermoplastics, is the glass transition temperature, usually denoted T_g. This is the temperature, above which, longer-range cooperative motions of the polymer chains become sufficient to allow the material to deform in response to an external load.

The glass transition temperature, T_g, is characterized by a steep drop in modulus. At temperatures below T_g the plastic will be a hard solid. This is known as the *glassy plateau*. There is a distinct difference between thermoplastics and thermosets at temperatures above T_g. Thermoplastics drops to a rubbery plateau where temporary molecular entanglements provide a mechanical response that is similar to a lightly crosslinked material. Under constant strain, however, these entanglements disengage, allowing the material to flow. At still higher temperatures, the relaxation time for disentanglements is shorter, the viscosity is lower and hence the material flows more readily. Thermoset materials also have a glass transition temperature, but their mechanical behaviour at temperatures above T_g is that of a crosslinked rubber: they can sustain deformation, often with high elastic recovery, but cannot flow. A plot of glass transition temperature for thermoset epoxy is shown in Figure (2.4). Higher degree of crosslink densities will increase the modulus level of the rubbery plateau of a crosslinked material and will normally increase the glass transition temperature.
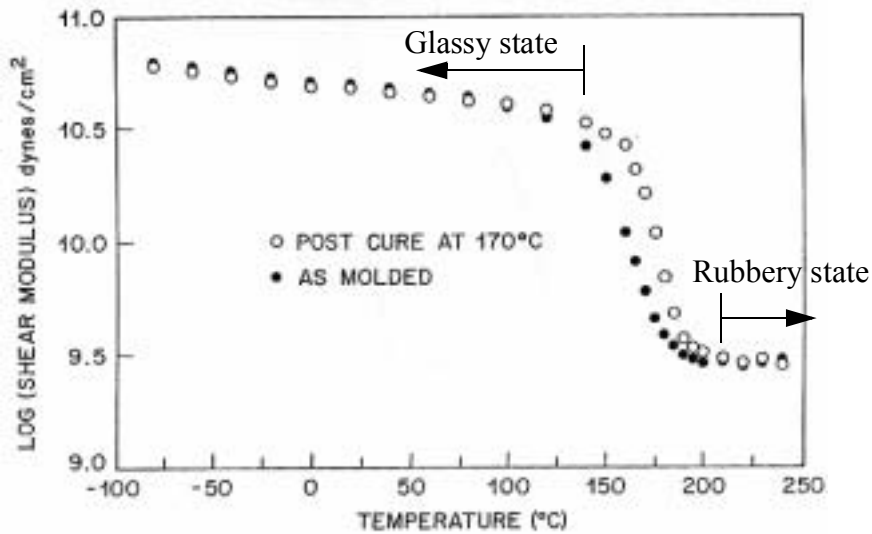
Figure 2.4   Plot of modulus vs. temperature for a thermoset material [41]. Note that 1 dyne/cm^2 = 0.1 Pa.

2.2 RHEOLOGY OF POLYMERS

Part of the dissertation was to investigate the capabilities and applicability of the polymer processing Computational Fluid Dynamics (CFD) code, C-Mold, which was used for simulating transfer moulding for MEMS packaging.

Polymeric materials are characterized by a complex rheology that strongly influences their processing. Their rheology is dependent on their molecular weight and molecular architecture and amount of filler. The rheology is also strongly influenced by process parameters such as the shear rate, temperature and residence time for curing materials.

Only a few special rheological issues of importance to thermosetting polymer processing will be mentioned here. A discussion on the general topic of polymer rheology can be found in textbooks [41], [75], [76].

2.2.1 Temperature Dependence

Of great importance to electronics packaging is the dependence of viscosity on temperature. Most processing operations are non isothermal, with large changes in temperature during the process. For this reason, it is important to quantify the temperature dependence of the viscosity so as to properly control flow induced forces.

2.2.2 Shear and Conversion-Induced Heating

It is well known that the thermal and rheological properties of EMC strongly depend on the extent of conversion which, in turn, is affected by the thermo-mechanical treatment imposed on the material during processing. The C-Mold software incorporates these effects [46].

2.3 THEORY OF FLOW SIMULATIONS OF THERMOSETS

The effect of the simultaneous processes of chemical reaction and physical flow of the polymer during processing have been successfully combined into a mathematical model by a research group at *AC Technology, Ithaca, New York, US*. A series of papers has been published on this development, including [46]-[49]. This model describes a thermosetting epoxy system during

13

transfer moulding and constitutes the fundamentals used in the CFD software which was used in this dissertation. This section gives an overview of the theories.

2.3.1 N-th Order Kinetics

Thermosetting polymers change both the mechanical and the chemical properties from the onset of the reaction to the moment they are set. Shear induced heating and contact to the heated mold walls will contribute to the cure rate. This extra effect can be included by keeping track of the cure state of the polymer during processing. Several theories have been developed to estimate the rate of reactive group conversion, $\dot{c}$. One of the most successful rate laws proposed for epoxies is the phenomenological rate law [45];

$$\dot{c} = \left(K_1 + K_2 c^m \right)\left(1 - c \right)^n \tag{2-1}$$

where

$$K_1 = A_1 \exp\left(\frac{E_1}{T} \right)$$
$$K_2 = A_2 \exp\left(\frac{E_2}{T} \right) \tag{2-2}$$

and K_1, K_2 are reaction constants; A_1 and A_2 are Arrhenius constants; and E_1 and E_2 are the corresponding energies of activation. The parameters n and m are associated with the reaction rate order, which is $n+m$.

2.3.2 Reactive Polymer Viscosity

As mentioned earlier, viscosity depends on a number of different parameters. The CFD software used in this dissertation, employs a modified Cross based model (Equation (2-5)) to describe the viscosity as a function of temperature, shear rate and state of cure [79]. The modified Cross models can predict the shape of a general flow curve including the asymptotic values of viscosity at very low and very high shear rates. The effect of curing on viscosity is included by multiplying the original Cross model by a gradually increasing term, $f(c)$, as a function of the fractional conversion, c, and the fractional conversion at the gel point, c_{gel};

$$f(c) = \left(\frac{c_{gel}}{c_{gel} - c} \right)^{C_1 + C_2 c} \tag{2-3}$$

where c is the degree of cure determined by Equation (2-1), c_{gel} is the degree of cure at which the polymer gels and the viscosity becomes infinite. C_1 and C_2 are the curing-dependent constants.

Equation (2-3) was put forward by Castro and Macosko ([77] and [78]). Other relations for $f(c)$ exists, but Equation (2-3) has become the most favoured one because there are more experimental data that support it.

The viscosity increases dramatically as the degree of cure approaches the gelation level and $f(c)$ goes to infinity. This is evident from Equations (2-3) and (2-4).

$$c < c_{gel} \qquad \eta(\dot\gamma, c) = \eta(\dot\gamma_0, c_0) \tag{2-4}$$

where

$$\eta(\dot\gamma) = \frac{\eta_0(T)}{1 + \left(\dfrac{\eta_0(T)\dot\gamma}{\tau^*}\right)^{1-d}} \tag{2-5}$$

and

$$\eta_0(T) = B\exp\left(\frac{T_b}{T}\right) \tag{2-6}$$

$$c > c_{gel} \qquad \eta(\dot\gamma) = \infty \tag{2-7}$$

In the above Equations (2-4) through (2-7), τ^* represents the shear stress at which shear thinning behaviour begins to occur. T_b is a constant that represents the temperature sensitivity of the zero-shear rate viscosity, $\eta_0(T)$. B is a function that enable vertical shift of the viscosity function.

2.4 VISCOELASTIC BEHAVIOUR OF POLYMERS

Solid polymers can show viscous response and flow under applied stress, typically over longer time periods. With polymers this behaviour, known as *creep,* is important in design considerations. Another mechanical response of polymer is their rate dependence, the stress depends not only on the strain but also on the rate of strain.

Two mechanical tests that are used to assess viscoelastic behaviour are the creep test and the stress relaxation test. In the creep experiment illustrated in Figure (2.5), a constant stress is instantaneously applied to a material and the strain is recorded as a function of time. There will be some immediate strain, as well as some continuing increase in strain due to viscous response. After some time, as the stress is removed and the degree of elastic recovery is measured, the unrecoverable strain is known as the *permanent set.*

This work is concerned with thermosets and the progress of conversion can be seen as an increase in molecular weight. The effect of molecular weight and crosslinking on creep behaviour are illustrated in Figure (2.6).
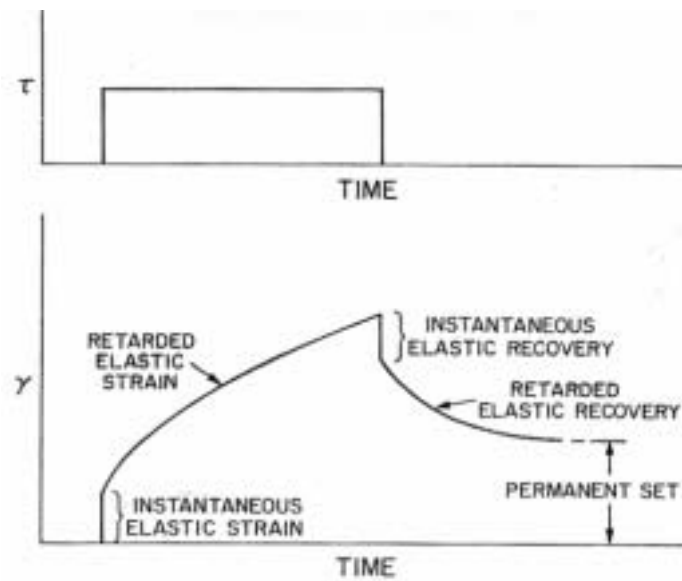
Figure 2.5   Creep test results [41].
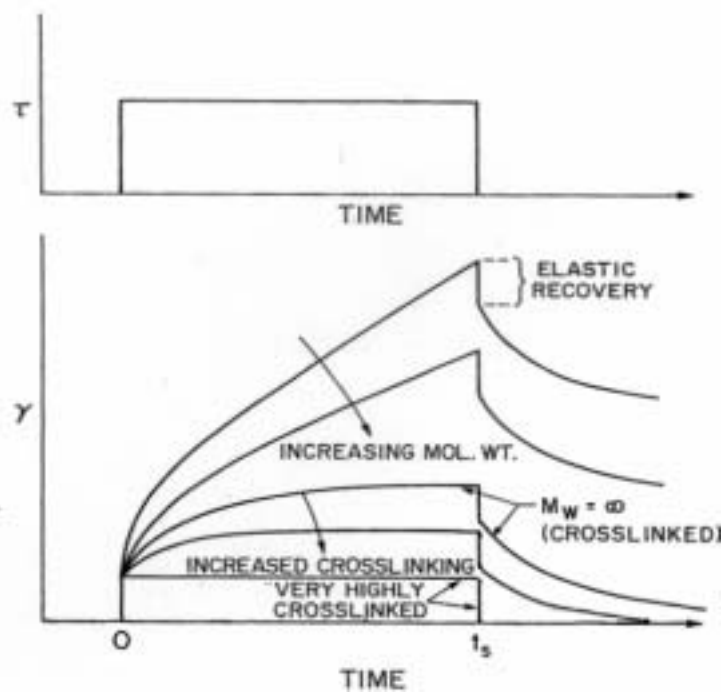
Figure 2.6   The effect of increasing molecular weight and increasing crosslink density on the creep behaviour of polymeric materials [41].

In the stress Relaxation experiment shown in Figure (2.7), an instantaneous strain is applied to the material, and the stress is measured as a function of time with the strain held constant. The time dependent stress divided by constant strain can be expressed as a time dependent relaxation modulus, *E(t)*. The effect of molecular weight and crosslink density on the relaxation modulus are illustrated in Figure (2.8).
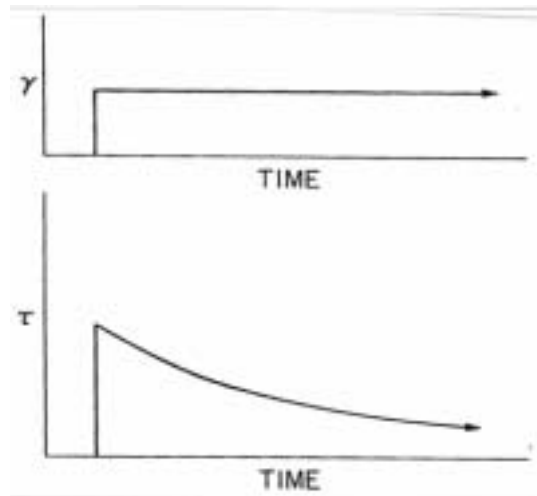
Figure 2.7   Illustration of the stress relaxation test [41].
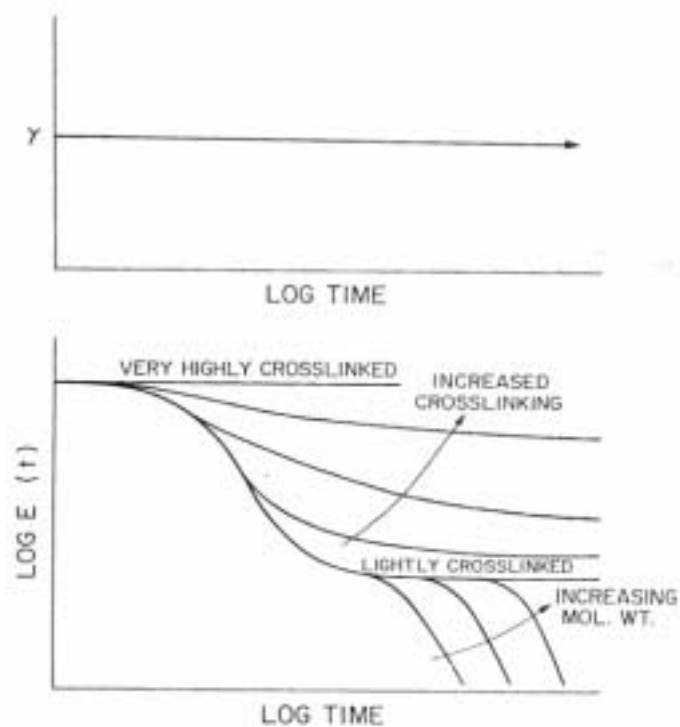
Figure 2.8   The effect of increasing molecular weight and increasing crosslink density on the stress relaxation experiment plotted in terms of the relaxation modulus [41].

   For plastic packaging of microelectronics, it is important to be aware of the mechanical response of polymer materials, particularly their creep and stress relaxation behaviour. Adding fillers to polymer materials produces a composite response of both the filler and the polymer. Since most fillers have high modulus, compounds shows significantly reduced creep and stress relaxation.

17

2.4.1 Time and Temperature-Dependent Behaviour of Linear Viscoelastic Materials

Creep is defined as the time-dependent change in strain following a step change in stress (ϑ_o), and for a linear viscoelastic material, it is expressed in the form $v(t) = J(t)\vartheta_o$, where $v(t)$ is the creep strain and $J(t)$ is the creep compliance (strain per unit stress). The complementary of creep is stress relaxation. Stress relaxation is the time-dependent change in stress following a step change in strain (v_o), and is expressed in the form $\vartheta(t) = G(t)v_o$, where $\vartheta(t)$ is the stress and $G(t)$ is the stress relaxation modulus. In many cases both these phenomena may provide equivalent information for studies of both fundamental viscoelastic properties and performance in practical applications. To facilitate a clearer understanding of these time-dependent phenomena, the variation of creep compliance and stress relaxation modulus over a wide time-scale is illustrated in Figures (2.9)a and (2.9)b respectively. In Figure (2.9)a, at very short times, the compliance, J_o, is that of a glassy solid and is independent of time; while, at very long times, the compliance,

(a)

(b)
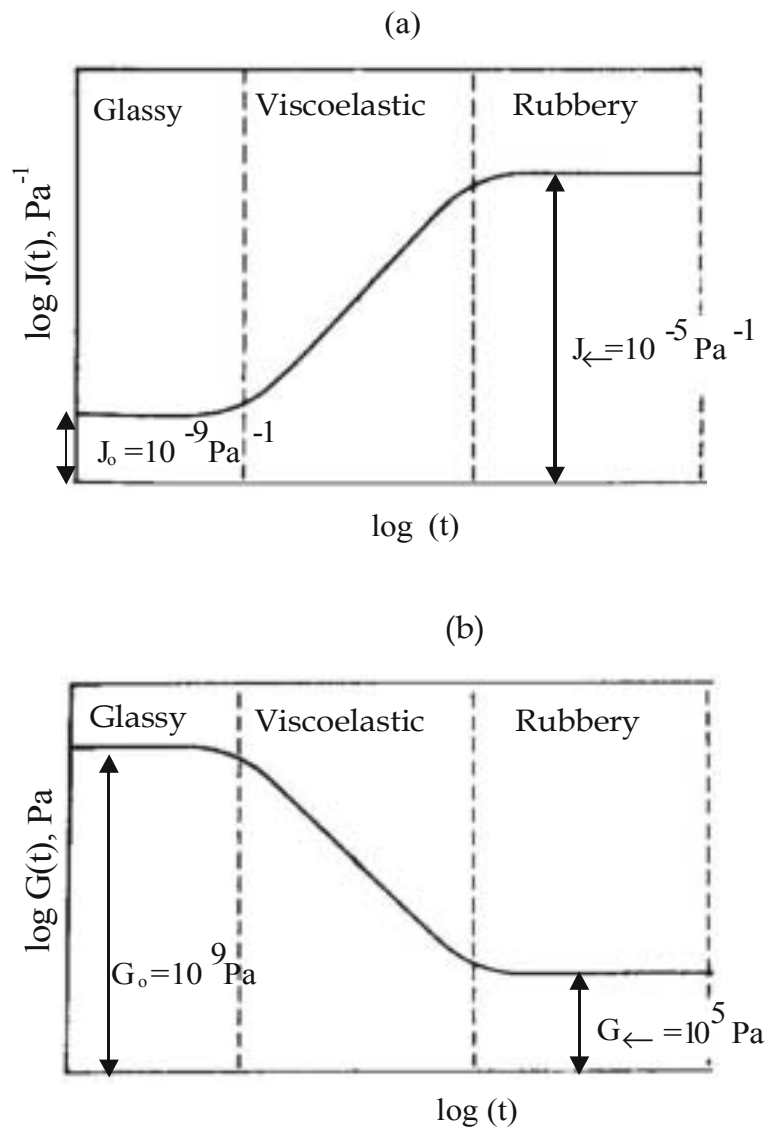
Figure 2.9 (a) Creep Compliance, J(t), and (b) Stress Relaxation Modulus, G(t), as a function of time (log-log plot) [43]

$J_{\leftarrow}$, is that of a rubber-like solid and is also time-independent. At intermediate times, the com-

pliance lies between these extremes and is time-dependent, so that the behaviour is viscoelastic. Similarly, in Figure (2.9)b, the stress relaxation modulus shows the same three regions of glassy, viscoelastic and rubber-like behaviour, where the glassy and equilibrium (or long-term) moduli, G_o and $G_\leftarrow$, are independent of time.

Besides the dependence on time, the mechanical behaviour of polymers are significantly affected by temperature also. This was discussed in Section 2.1.2 and shown in Figure (2.4).

The description of the linear viscoelastic response for some polymers to small stresses is greatly simplified by the application of the Boltzmann Superposition Principle and the Time-Temperature Superposition.

The Boltzmann Superposition Principle states that strains are a linear functions of stress, so that the total effect of applying several stresses is the sum of the effects of applying each one separately. Application of the superposition principle makes it possible to predict the mechanical response of an amorphous polymer to a wide range of loading conditions from a limited amount of experimental data. The principle applies to both static and time-dependent stresses.

The Time-Temperature Superposition (TTS) principle states that an increase in temperature accelerates molecular and segmental motion. This brings the system more rapidly to equilibrium or apparent equilibrium and accelerates all types of viscoelastic processes. A convenient way of formulating this temperature effect is in terms of the ratio $a_T(T)$ of the time constant (*relaxation time*) of a particular response ϑ (e.g E-modulus) at temperature T to its value ϑ_0 at a convenient reference temperature T_0, or $E(T,t) = E(T_o, \bullet)$, where $\bullet = t/a_T(T)$ is the reduced time, and T and t are the temperature and time respectively [44]. For many cases, $a_T(T)$ does not vary with ϑ, so that changes in temperature shift the distribution of relaxation times to smaller or greater values of ϑ but does not otherwise alter it. In other words, the behaviour at high temperatures and high strain rates is similar to that at low temperatures and low strain rates.

One of the most common functions relating shift factor and temperature is the WLF (Williams, Landel, Ferry) equation, which has the following form [37] & [38]:

$$\log a_T / T0 = \log \frac{t}{\bullet} = \frac{-C_1 / T - T_0 0}{C_2 + / T - T_0 0} \tag{2-8}$$

Recommended further literature on the whole subject of the mechanical response of polymers include [39] and [40].

2.4.2 Phenomenological Models

Mechanical models consisting of springs and dashpots have proven useful for modelling the mechanical behaviour of linear viscoelastic materials. Many complex models have been proposed [44] to accurately describe a material behaviour. The approach used most often is to use

an array of Kelvin models in parallel for simulating creep, and an array of Maxwell models in parallel for simulating stress relaxation (Figure (2.10)).:
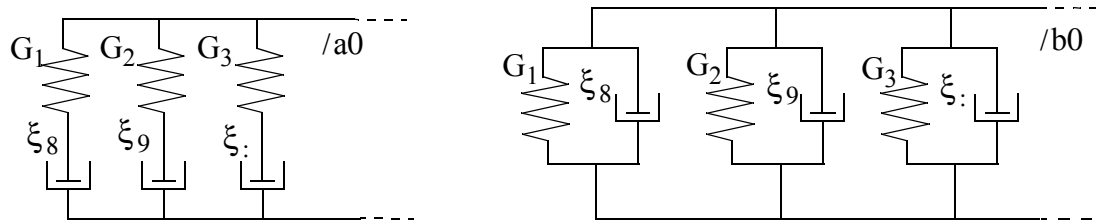
Figure 2.10   (a) Generalized Maxwell model, and (b) Generalized Kelvin-Voigt model

The response from a series of Maxwell elements can be expressed in the following form

$$G(t) = G_0 + \sum_{i=1}^{N} G_i \exp(-t/\tau_i) \tag{2-9}$$

where, N is the number of Maxwell elements and τ_i are the relaxation times.

2.4.3 Integral Representation of Constitutive Equations

The basis for the integral representation of the linear viscoelastic behaviour for multi-step loading situations is again the Boltzmann Superposition Principle. Accordingly, for creep loading under an arbitrary time-dependent stress $\sigma(t)$, the creep strain at time t is given by:

$$\varepsilon(t) = \int_0^t J(t-\tau)\frac{d\sigma(\tau)}{d\tau}d\tau \tag{2-10}$$

In a complementary manner, for a stress relaxation situation under an arbitrary time-dependent strain $\varepsilon(t)$, the stress at any time t is given by:

$$\sigma(t) = \int_0^t G(t-\tau)\frac{d\varepsilon(\tau)}{d\tau}d\tau \tag{2-11}$$

Therefore, provided the creep compliance (J) and the stress relaxation modulus (G) are known, the creep strain and stress relaxation in equations (2-10) and (2-11) can be calculated for arbitrary loading conditions. Note that for linear viscoelastic materials, the creep compliance and stress relaxation modulus are related through a convolution integral (equation (2-12)), and are therefore inter-convertible.

$$\int_0^t G(t-\tau)J(\tau)d\tau = t \tag{2-12}$$

All of the above equations (2-10)-(2-12) were written for simple uniaxial deformations. Generalizing now to three-dimensional multi-axial stress and strain states, the integral representa-

20

tion for isotropic linearly viscoelastic materials may be expressed in terms of the deviatoric and hydrostatic components (analogous to isotropic linear elasticity) as:

$$s_{ij}(t) = 2\int_0^t G(t-\tau)\frac{\partial d_{ij}(\tau)}{\partial \tau}d\tau$$

$$\omega_{ii}(t) = 3\int_0^t K(t-\tau)\frac{\partial \kappa_{ii}(\tau)}{\partial \tau}d\tau$$

(2-13)

where $G(t)$ and $K(t)$ are the time-dependent shear and bulk stress relaxation moduli, s_{ij} and d_{ij} are the deviatoric and ω_{ii} and κ_{ii} are the dilatational stress and strain respectively.

2.5 OTHER PHYSICAL PROPERTIES RELEVANT TO PLASTIC PACKAGING

Other physical properties of polymer materials are important to microelectronics packaging.

2.5.1 Thermal Conductivity

Polymers have significantly lower thermal conductivities than metals, ceramics and glasses used in electronics. This can cause problems in maintaining a moderate temperature in heat dissipating devices. If a device generates more heat than acceptable, some auxiliary heat dissipation mechanism, such as external cooling fins, can be added.

2.5.2 Heat Capacity

Plastics have higher heat capacities than most other packaging and device materials. Heat capacity is often a strong function of temperature, so listed values often do not describe the complete parameter space and should be read with caution.

2.5.3 Coefficient of Thermal Expansion

The coefficient of thermal expansion (CTE) is one of the more important physical parameters of packaging materials because mismatch in thermal expansion among the different materials within the package can contribute to significant restrained shrinkage stresses. These stresses can reach levels that cause fracture of; the moulding compound, the passivation layers of the device, or the device itself. The CTE changes at thermodynamic transitions, such as the glass transition temperature of polymeric materials, or phase transitions such as crystallization. The different regions of the plot of CTE vs. Temp. are denoted ζ with the appropriate subscript. The region at lowest temperature is ζ_1 and the next higher region is ζ_2 and so on. For EMC's, the CTEs above and below T_g are the ones of importance. These are shown in the plot on Figure (2.11).

21
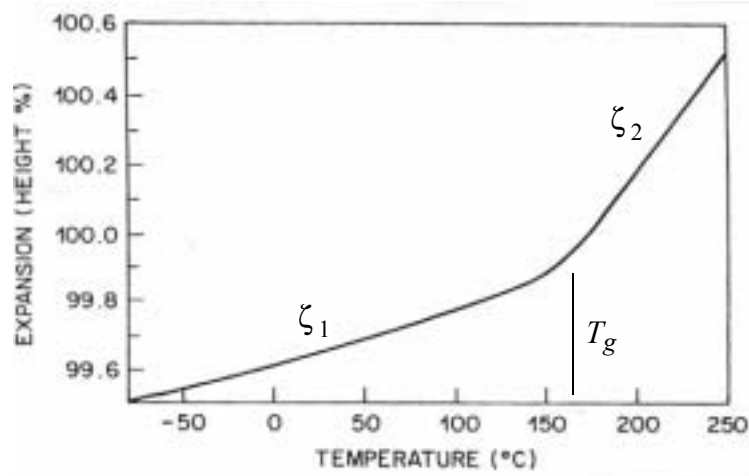
Figure 2.11   Plot of expansion vs. temperature for an epoxy moulding compound, showing the two regions of different coefficient of thermal expansion above and below the glass transition temperature [41].

Matching the coefficients of thermal expansion as closely as possible minimizes the thermal shrinkage stresses that are encountered. This strongly influences the selection of leadframe materials, epoxy moulding compounds, filler types and filler levels. It is also apparent that selecting polymeric materials that will remain below their glass transition temperature provides a material with the lower ζ_1 values. The modulus is higher below T_g, however, in some cases the temperature induced stresses can actually be higher, since the shrinkage stresses depend on the product of the difference in the coefficients of thermal expansion, the modulus of the plastic and the temperature difference.

2.6 EPOXIES

Postmolded packaging of IC devices requires a low initial viscosity of the compound so it can flow over the leadframe and wire bonds without causing significant deformation. Other requirements are a high modulus and high heat distortion temperature in the final state to withstand mechanical operations such as trim and form, and solder attachment to a printed circuit board. Thermoset polymers are uniquely suited for these needs because they polymerize to a thermally intractable material from a resin exhibiting an initial low-viscosity. Epoxies are also well suited because of low curing shrinkage and high T_g. Thermoplastics are normally not suited as they often have a fairly high melt viscosity that could damage the device as it flows over and around it. Also, their softening temperatures, T_m and/or T_g, are normally too low for solder operations.

2.6.1 The Formulation of Epoxy Moulding Compounds

The formulation for most epoxy moulding compounds consists of a complicated and often proprietary mixture of epoxy resin, hardener (or curing agent), catalyst(s), fillers, flame retardants, flexibilizers, coupling agents, mold release agents, and colorants.

2.6.2 Epoxy curing

The epoxy resins get their name from the presence of epoxide groups that are present in the polymer before crosslinking. The epoxy resins are cured by many types of materials, including polyamines. Figure (2.12) shows a Biphenyl resin structure (a) and a diamine hardener (b). The chemical reaction with amines involves opening the epoxide ring to give a η-hydroxyamino linkage. The principles of the reaction can be seen in Figure (2.13).

a)   b)
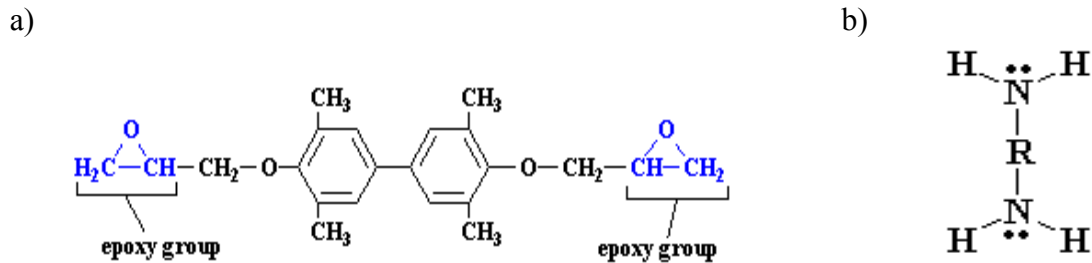
Figure 2.12   a) Biphenly-based epoxy resin system and b) diamine hardener.
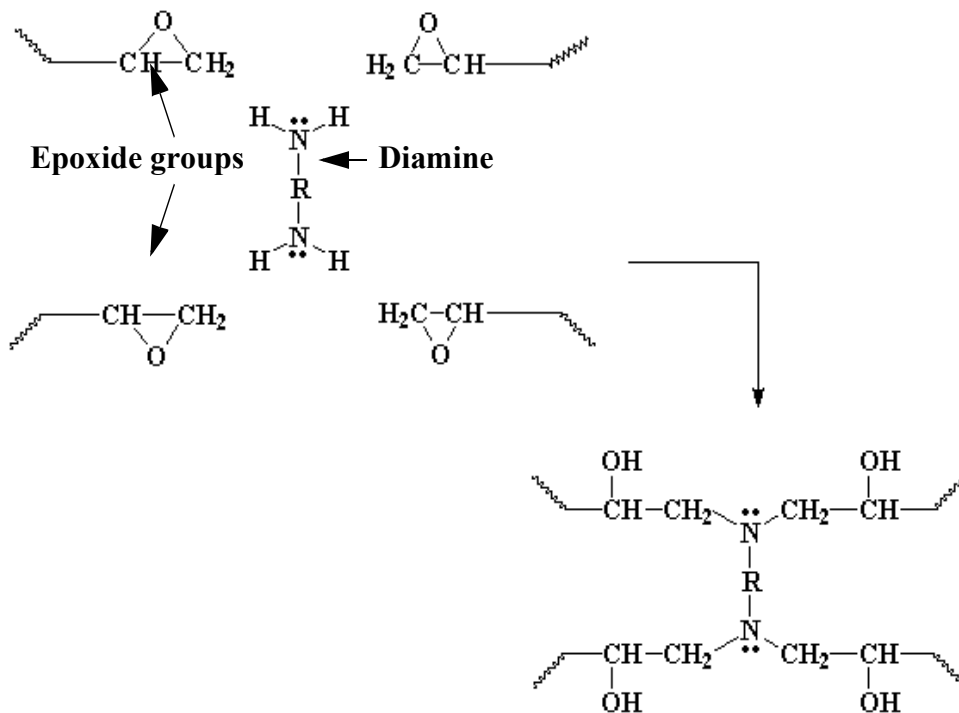
Figure 2.13   Schematic of the cross-linking reaction

2.7 TRANSFER MOULDING OF AN SMALL OUTLINE PACKAGE (SOP)

Transfer moulding is probably the most used process for plastic microchip encapsulation. The Transfer Moulding Machine performance can have significant effect on packaging productivity and yield. The effects of the machinery can also extend to reliability since accommodations made to compensate for faulty or inadequate machinery, such as low transfer pressure or low clamp pressure, can cause insufficient moulding compound density resulting in higher moisture ingress and uptake.

A transfer moulding machine is essentially a large mechanical clamp, usually driven hydraulically, which holds the mold closed during material injection and curing, and a hydraulic transfer ram or piston which pushes the moulding compound into the mold.
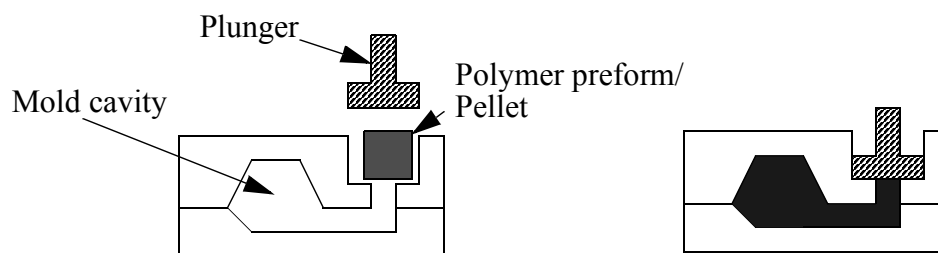
 Figure 2.14   Transfer moulding principle diagram.

More detailed information on transfer moulding can be found in [41], [45] and [60]. The following sections will briefly review the process characteristics of transfer moulding for plastic packaging of microelectronic devices.

2.7.1 Preheating

The purpose of the preheating step is to increase the temperature of the moulding compound to a temperature at which it can be pushed into the mold under the action of the transfer plunger. Typical preheat times are of the order of 8-30 seconds. Longer times can overly advance the polymerization reaction, reducing the flow length and flow time of the material in the mold and increasing the flow-induced stresses.

2.7.2 Transfer of Moulding Compound in The Mold

From the time the moulding compound is dropped in the mold to the time it sets in the mold cavities, it goes through a series of processes. Firstly it is crushed to make contact to the heated mold walls for better heating. It liquifies due to the increase in temperature. Then it is pushed through the runner and into the cavity via a gate. This process can be simulated using specially designed CFD softwares like the one used for part of this dissertation.

The transfer of the moulding compound into the mold is the most important process step with regard to moulding productivity and yield. It is during this process that the flow-induced stresses can cause wire sweep and paddle shift. High productivity moulding requires both skilful mold design and optimum process parameters. Ideally the design, process and material should all be integrated in an optimised configuration. The process characteristics of the mold filling step are

reviewed in this section. There are several distinct flow regimes during the transfer and each has been described separately.

2.7.3 Transfer Pot

The flow and heating in the transfer pot begins the transfer of the moulding compound into the mold. In most tool configurations, the pot is a simple cylindrical shape with a diameter between 10 and 70 mm. The runners emanate directly from the transfer pot in most designs, although distribution rings or enlarged runner entrances are also used. A review of the different transfer pot and runner configuration is provided in Figure (2.15). The distribution ring geometry shown in Figure (2.15)b provides a more uniform flow field in the transfer pot with no angular dependence, but it is unknown whether there is any benefit to this flow as compared to the direct runner coupling shown in Figure (2.15)a.
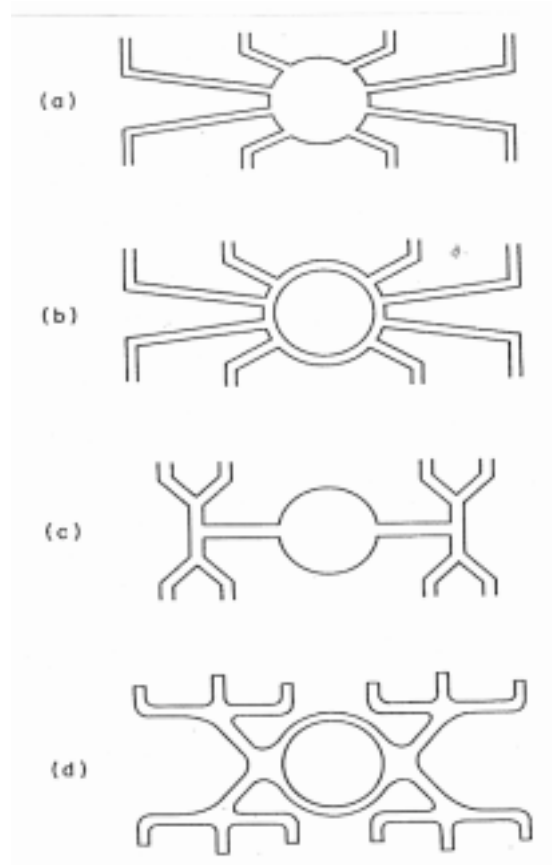
Figure 2.15   A variety of different transfer pot and runner entrance configurations: (a) direct coupling of runners to transfer pot, (b) runner coupling through distribution ring, (c) a manifold runner system where larger feed runners supply a smaller manifold which supplies smaller runner arms, (d) runner coupling through enlarged runner entrance with manifold.

The compound is preheated in the pot to the temperature of the moulding tool. Typical material residence times in the pot range from a few seconds for the material that is first extruded, up to 25 seconds for the last moulding compound that is transferred into the mold.

2.7.4 Flow in the Runner

The runner cross section will vary among different mold designs, but the general shape in cavity chase molds is that of a trapezoid. Semicircles and rounded trapezoids are also used in some designs. Four runner cross sections are provided in Figure (2.16). The trapezoidal geometry is easily machined and also provides easy ejection, but it is not optimum in terms of heat transfer or for any analytical treatment of heat transfer and flow behaviour. The approach of most investigators has been to combine both experimental and analytical approaches to determine important process information such as pressure drop and temperature increase during flow.
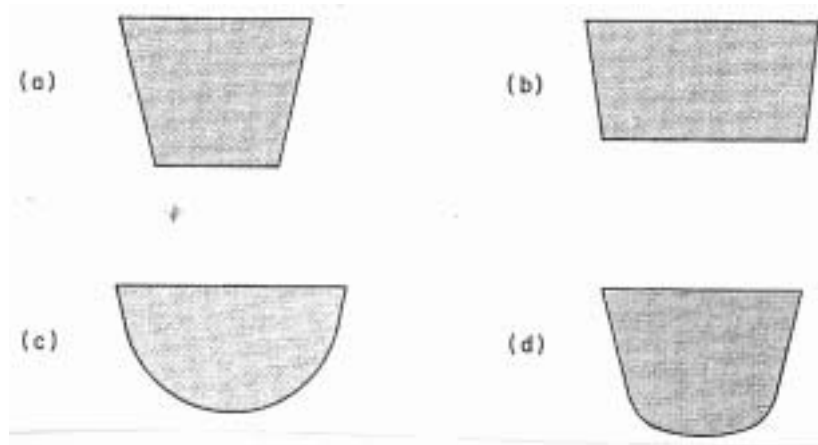
Figure 2.16   Typical runner cross sections of both cavity chase molds and aperture plate molds: (a) trapezoidal, (b) near-rectangular, (c) semicircular, (d) rounded trapezoidal. Typical runner widths are approximately 5mm with variations around this value.

For further information on the very important topics of *Pressure Drop in the Runner*, *Heating During Flow in the Runner* and *Viscosity During Flow in the Runner*, the reader is referred to [41] (p200-218).

2.7.5 Flow Through the Gate

The flow of the moulding compound through the gates determines the mold-filling profile to a large extent. Flow through the gates also has an influence on the temperature and viscosity of the moulding compound as it contacts the leadframe and device. Again, for further information on the very important topics of *Pressure Drop Through the Gate* and *Heating on Flow Through the Gate*, the reader is referred to [41] (p218-224).

2.7.6 Flow in the Cavity

The flow in the cavity determines the extent of the flow-induced stresses that are imposed in the leadframe and wire bonds, thereby affecting the moulding yield. The mold designer and operator have very little influence on the flow of moulding compound in the cavities once decisions on upstream variables, such as runner geometry, filling profile and moulding compound selection are made.

The leadframe will split the flow into two separate flow fronts moving across the cavity, one above and one below the leadframe as is shown in Figure (2.17). The existence of these two flow

26

fronts and the distance between them depends on many factors which include the flow porosity of the frame, the relative size of the cavities above and below the leadframe, the material rheology and the position where the moulding compound enters the cavity.
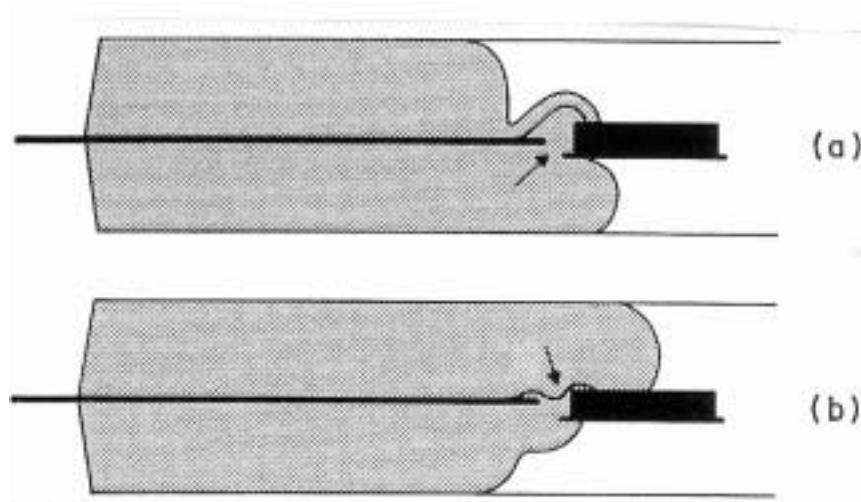
Figure 2.17   Cross section view of flow of the moulding compound in the cavity of the packaging mold showing the advancing flow front split into two separate fronts as it divides around the leadframe: (a) the preferred configuration for moulding wire bonded devices is for the flow in the lower cavity, the one without the wire bonds, to lead the flow in the upper cavity, (b) the less desirable configuration of the leading flow in the cavity half that contain the wire bonds.

2.8 MOULDING TOOL DESIGN CONSIDERATIONS

The moulding tool probably has more influence on the productivity and yield of plastic packaging than any other piece of production equipment. It is also one of the most expensive pieces of capital equipment, so mistakes are not easily obliterated by simply replacing an inferior tool. A production size moulding tool can easily cost more than a production moulding machine because of the high labour content of the custom designed and machined tool. There are numerous different types of tools for plastic packaging like *Cavity Chase Molds, Aperture Plate Molds, Multiplunger Molds etc.* Again the reader is referred to [41], [45] and [60] for more details on the subject.

   A tool design is very complicated and has to be designed and manufactured by experts in the field.

2.9 MATERIAL DESCRIPTION OF SILICON

Single crystal silicon has a diamond cubic lattice. The material is orthotropic elastic. Due to symmetry of the lattice, Hooke's law for the a cartesian coordinate system aligned with the <100> directions is written below:

$$
\begin{bmatrix} \omega_1 \\ \omega_2 \\ \omega_3 \\ \vartheta_4 \\ \vartheta_5 \\ \vartheta_6 \end{bmatrix} = \begin{bmatrix} C_{11} & C_{12} & C_{12} & 0 & 0 & 0 \\ C_{12} & C_{11} & C_{12} & 0 & 0 & 0 \\ C_{12} & C_{12} & C_{11} & 0 & 0 & 0 \\ 0 & 0 & 0 & C_{44} & 0 & 0 \\ 0 & 0 & 0 & 0 & C_{44} & 0 \\ 0 & 0 & 0 & 0 & 0 & C_{44} \end{bmatrix} \begin{bmatrix} \kappa_1 \\ \kappa_2 \\ \kappa_3 \\ \nu_4 \\ \nu_5 \\ \nu_6 \end{bmatrix}
$$

(2-14)

where C_{ij} are the elastic constants. Here use is made of the notation normally used for composite materials. $\omega_1, \omega_2, \omega_3$ are normal stresses, ϑ_4, ϑ_5, and ϑ_6 are the shear stresses. Correspondingly the normal and shear strains are denoted κ_i and ν_i respectively [85]. Complete plots of the elastic constants of single crystal silicon for all crystal directions can be found in [84].

2.10 PIEZORESISTIVITY IN SILICON

Piezoresistance is a small change in the bulk resistivity of a material induced by small mechanical stresses applied to the material. Most materials exhibit piezoresistivity, but the effect is particularly pronounced in some semiconductors. Monocrystalline silicon has a high piezoresistivity. Combining the high piezo-resistivity with its excellent mechanical and electrical properties, makes it a superb material for the conversion of mechanical stress into an electrical signal.

For a three-dimensional anisotropic crystal such as single-crystal silicon, the electrical field vector (κ) is related to the current density vector (j) by a 3x3 resistivity tensor [62]. Experimentally, the nine coefficients are always found to reduce to six, and the symmetric tensor is given by:

$$
\begin{bmatrix} \kappa_1^E \\ \kappa_2^E \\ \kappa_3^E \end{bmatrix} = \begin{bmatrix} \psi_1 & \psi_6 & \psi_5 \\ \psi_6 & \psi_2 & \psi_4 \\ \psi_5 & \psi_4 & \psi_3 \end{bmatrix} \begin{bmatrix} j_1 \\ j_2 \\ j_3 \end{bmatrix}
$$

(2-15)

where κ_i^E and j_i represent electric field and current density components respectively, and ψ_i represent resistivity components. By aligning the Cartesian axes to the (100) axes in a cubic silicon lattice, ψ_1, ψ_2 and ψ_3 will all be equal. This is because they represent resistance along the (100) axes and are denoted by ψ. The remaining components of the resistivity matrix, which represent cross-axis resistivity, will be zero because unstressed silicon is electrically isotropic. Upon applied stress, the resistivities change. The change in each resistivity component, $\div \psi_i$, are related to all the stress components. Any stress state can always be decomposed into tree normal components (ω_i) and three shear components (ϑ_i), as shown in Figure (2.18).
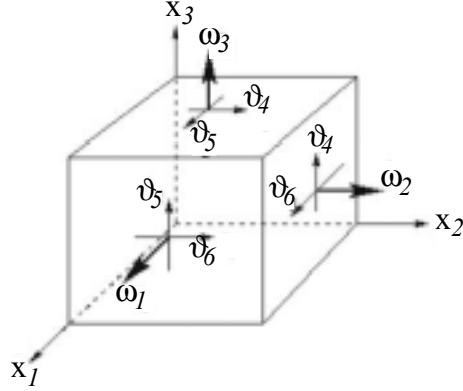
Figure 2.18   Definition of normal-(ω_i) and shear-(ϑ_i) stresses.

The change in the six components of the resistivity matrix (expressed as a fraction of the unstressed resistivity ψ) can then be related to the six stress components by a 36-element tensor. However, due to symmetry in the silicon material, with the $x_{1,2,3}$-axes aligned in the <100> directions, this tensor is populated by only three non-zero constants as shown in Equation (2-16):

$$
\begin{bmatrix} \psi_1 \\ \psi_2 \\ \psi_3 \\ \psi_4 \\ \psi_5 \\ \psi_6 \end{bmatrix} = \begin{bmatrix} \psi \\ \psi \\ \psi \\ 0 \\ 0 \\ 0 \end{bmatrix} + \begin{bmatrix} \div\psi_1 \\ \div\psi_2 \\ \div\psi_3 \\ \div\psi_4 \\ \div\psi_5 \\ \div\psi_6 \end{bmatrix} \quad 3\frac{1}{\psi}\begin{bmatrix} \div\psi_1 \\ \div\psi_2 \\ \div\psi_3 \\ \div\psi_4 \\ \div\psi_5 \\ \div\psi_6 \end{bmatrix} = \begin{bmatrix} \phi_{11} & \phi_{12} & \phi_{12} & 0 & 0 & 0 \\ \phi_{12} & \phi_{11} & \phi_{12} & 0 & 0 & 0 \\ \phi_{12} & \phi_{12} & \phi_{11} & 0 & 0 & 0 \\ 0 & 0 & 0 & \phi_{44} & 0 & 0 \\ 0 & 0 & 0 & 0 & \phi_{44} & 0 \\ 0 & 0 & 0 & 0 & 0 & \phi_{44} \end{bmatrix}\begin{bmatrix} \omega_1 \\ \omega_2 \\ \omega_3 \\ \vartheta_4 \\ \vartheta_5 \\ \vartheta_6 \end{bmatrix}
\tag{2-16}
$$

where ϕ_{ij} is the piezoresistive-coefficients with units of Pa^{-1} and may either be positive or negative and are sensitive to doping type, doping level and operating temperature.

It is evident that ϕ_{11} relates the resistivity in any direction to stress in the same direction, whereas ϕ_{12} and ϕ_{44} are cross-terms.

Equation (2-16) was derived in the context of a coordinate system aligned to the (100) axes and is not always convenient to apply. A preferred representation is to express the fractional change in an arbitrarily oriented diffused resistor by:

$$
\frac{\div R}{R} = \phi_l\omega_l + \phi_t\omega_t
\tag{2-17}
$$

where ϕ_l and ω_l are the piezo-resistive coefficient and stress parallel to the direction of the current flow in the resistor (i.e. parallel to its length) and ϕ_t and ω_t are the values in the transverse direction.

In this work, the resistors are aligned in the <110> direction, which results in [53]:

$$\phi_l = \frac{1}{2}/\phi_{11} + \phi_{12} + \phi_{44}0$$

$$\phi_t = \frac{1}{2}/\phi_{11} + \phi_{12} - \phi_{44}0$$

(2-18)

CHAPTER 3

THERMOMECHANICAL MATERIAL CHARACTERISATION

This chapter deals with the material characterisation of the epoxy moulding compound used for the plastic package in question. Realistic modelling and analysis of the mechanical performance and reliability of electronic packages requires accurate material data to comply with the corresponding constitutive relations. Polymeric materials pose some significant problems due to their inherent temperature and time-dependent material properties.

The temperature dependence of the static modulus and Coefficient of Thermal Expansion (CTE) of the fully cured EMC was studied here.

3.1 COEFFICIENT OF THERMAL EXPANSION

Expansion versus temperature was measured using the Mettler Toledo Thermomechanical Analyser (TMA). The result can be seen in Figure (3.1) below. The temperature derivative of the expansion is defined as the coefficient of thermal expansion (CTE), ζ, and has the units of ($^oC^{-1}$). The sample height was 2.5mm, hence $L=2.5$.

The point of deflection on the curve is often assumed to be the glass transition temperature, T_g, of the polymer. From this experiment, T_g was found to be approximately 115^oC. A DMA scan from -25^oC to 175^oC (5^vC/min.) at 1Hz showed a T_g of 130^oC from the point of deflection of the loss modulus (Figure (3.2)).
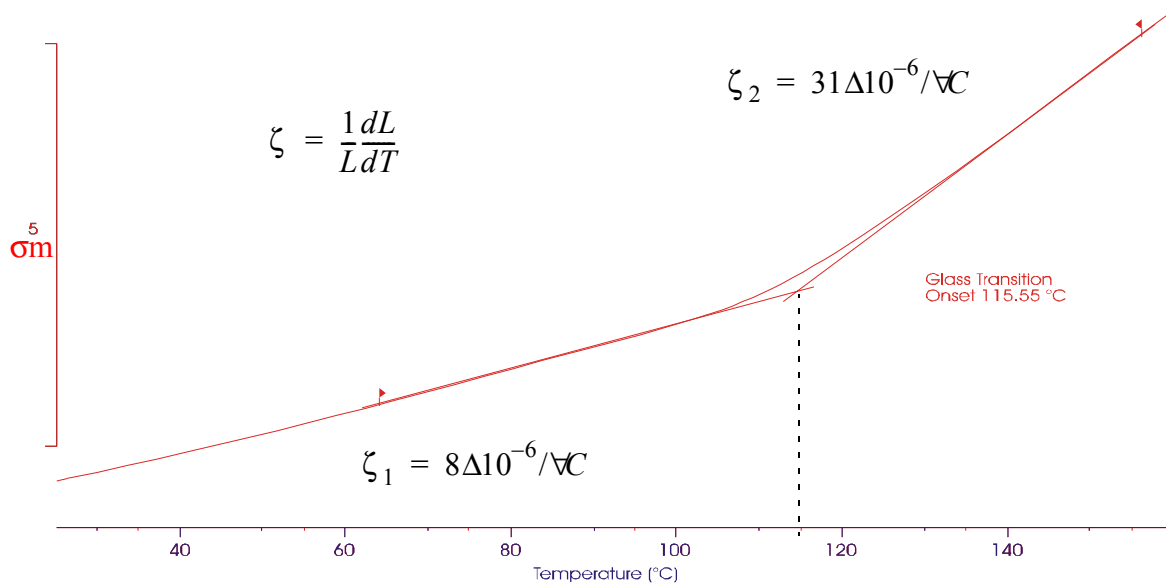
Figure 3.1   Experimental data from thermal expansion measurements.
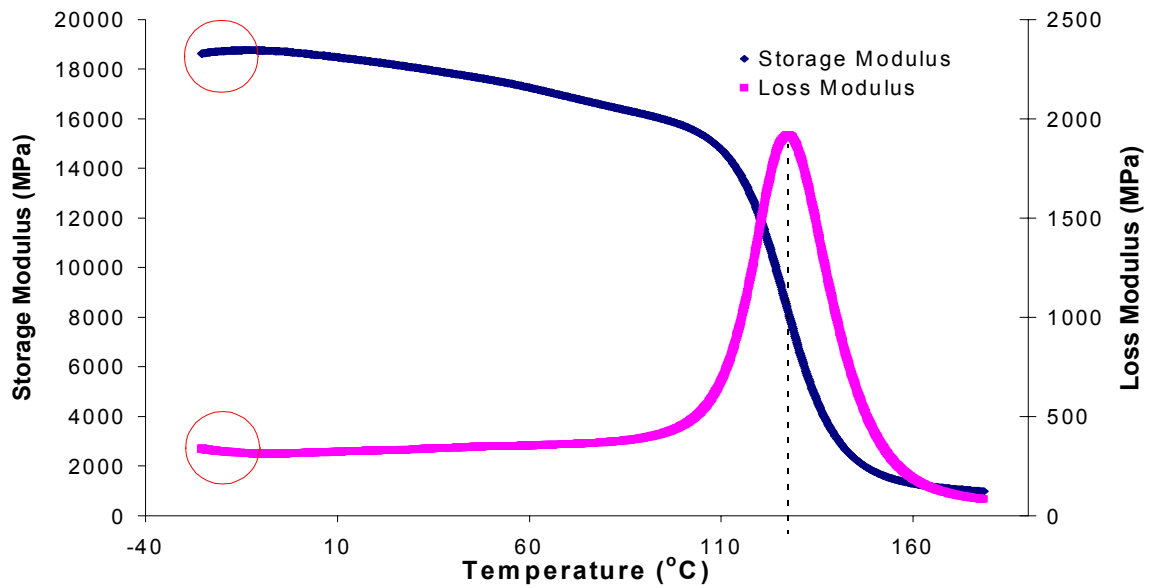
Figure 3.2   DMA results. Note that the anomaly in the left end side of the graphs are caused by non-uniform temperature of the specimen at the start of the measurements.

3.2 STRESS RELAXATION MODULUS

The TA Instrument's Dynamic Mechanical Analyser (DMA) 2980 with the single cantilever clamp was used to conduct the viscoelastic stress relaxation experiments. Moulded and fully cured samples of $50 \times 12 \times 2 mm^3$ were prepared for the experiment.

The raw stress relaxation data is shown in Figure (3.3). The data was replotted on a logarithmic time axis. A reference temperature was then chosen ($T_0 = 30^{o}$C) and all the data was shifted

horizontally with respect to this temperature. The result was the master stress relaxation curve and shift function shown below in Figure (3.4) and Figure (3.5) respectively.
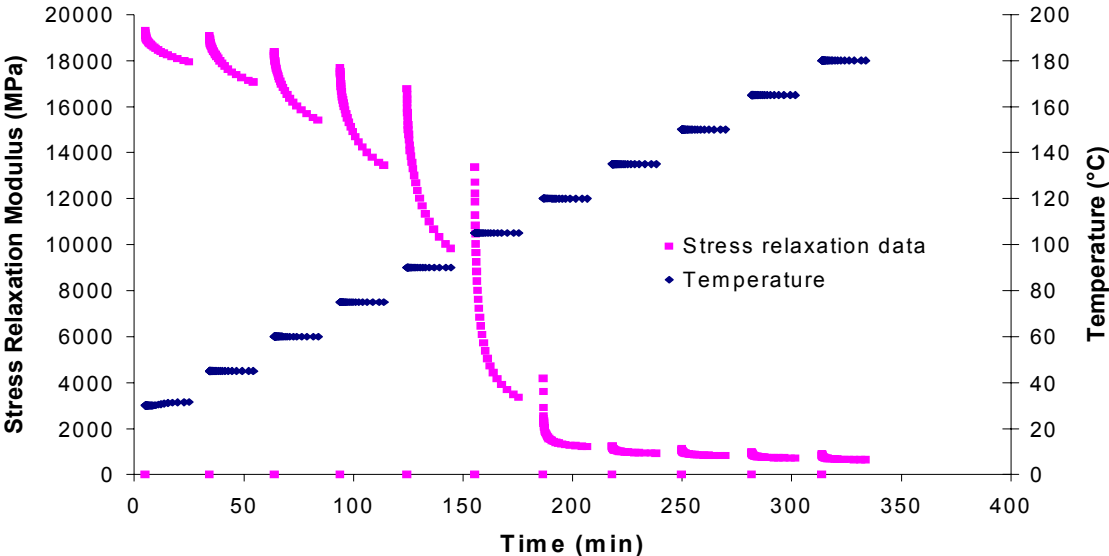
Figure 3.3   Raw stress relaxation data.
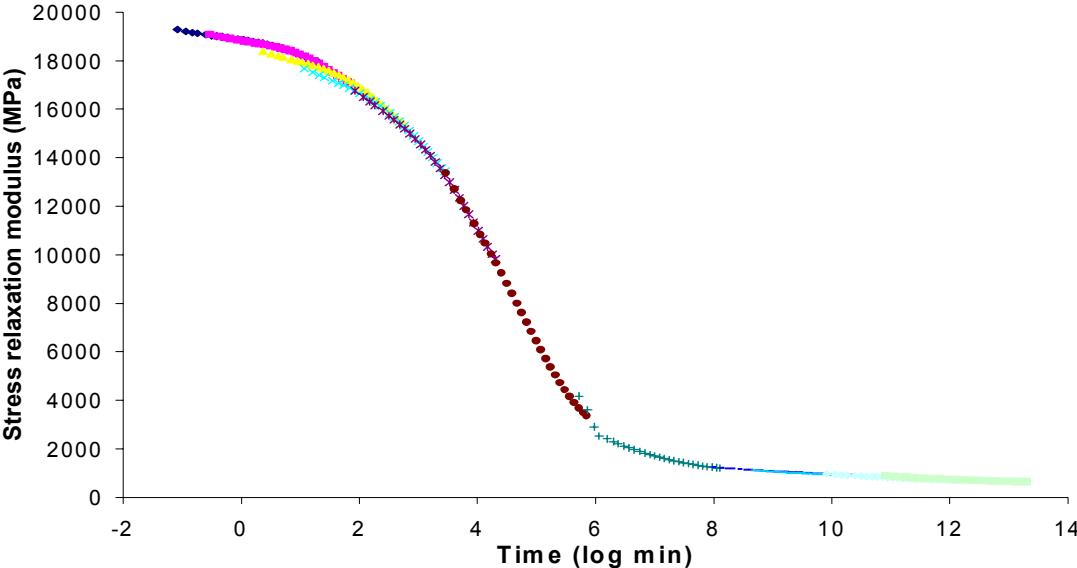
Figure 3.4   Stress relaxation modulus master curve.
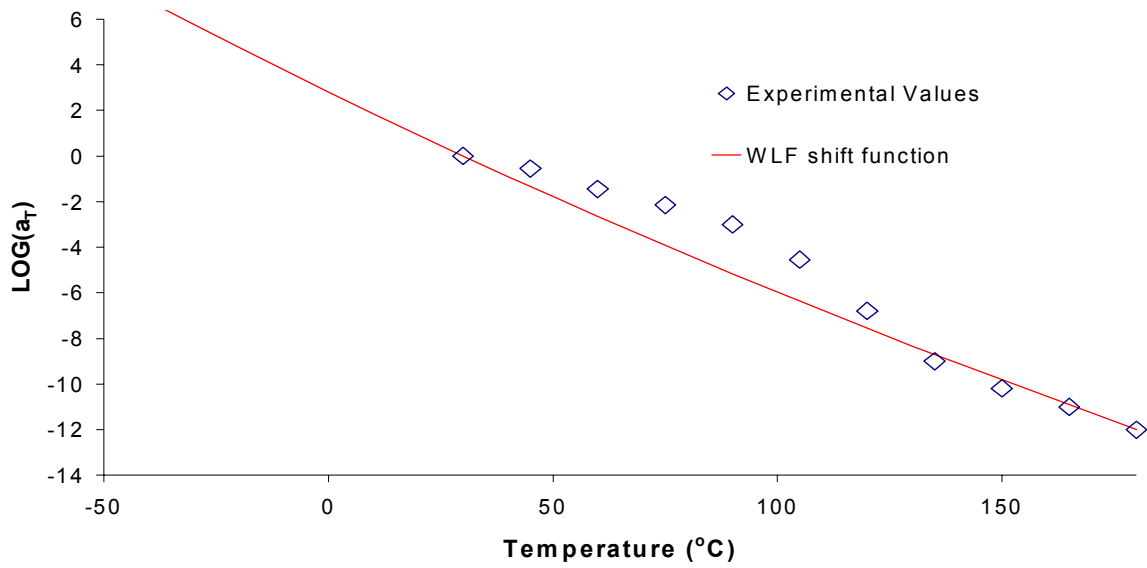
Figure 3.5   Shift function.

A series of parallel Maxwell elements, so called Prony series, were used to represent the relaxation spectrum. Ansys^{TM}, the Finite Element Method (FEM) code used for the static stress analysis, required an input of the following form:

$$G/t0 = G_{\leftarrow} + \sum_{i=1}^{6} G_i \exp\left(\frac{-t}{\vartheta_i}\right) \qquad (3\text{-}1)$$

where $G_{\leftarrow}$ is the fully relaxed modulus, ϑ_i is the relaxation time for the ith element. The values that were used for G_i and ϑ_i were found by non-linear curve fitting and are listed in Table (3.1) below. A maximum limitation of 6 terms makes the curve in Figure (3.6) not completely smooth.

Table 3.1: Prony series coefficients.

i	G_i	ϑ_i
$\leftarrow$	332	
1	573	19
2	791	298
3	1563	4819
4	2157	60451
5	1497	733008
6	386	94327507

The choice for a pre-defined shift function in the FEM code was limited to the WLF [36] or the Tool-Narayanaswamy [83]. The WLF was found to give the best fit to the experimental data. The WLF was input in the following form:

$$\log a_t = \frac{-a/T - T_0 0}{b + T - T_0}$$

(3-2)

The parameters that were found for the best fit of the WLF equation, with $T_0=303K$ are listed in Table (3.2).

Table 3.2: WLF parameters.

Parameter	Value
T_0	303K
a	-34
b	-586

The master curve at 30°C (303K) with the fitted Prony series is plotted in Figure (3.6) below. A satisfactory fit was obtained.
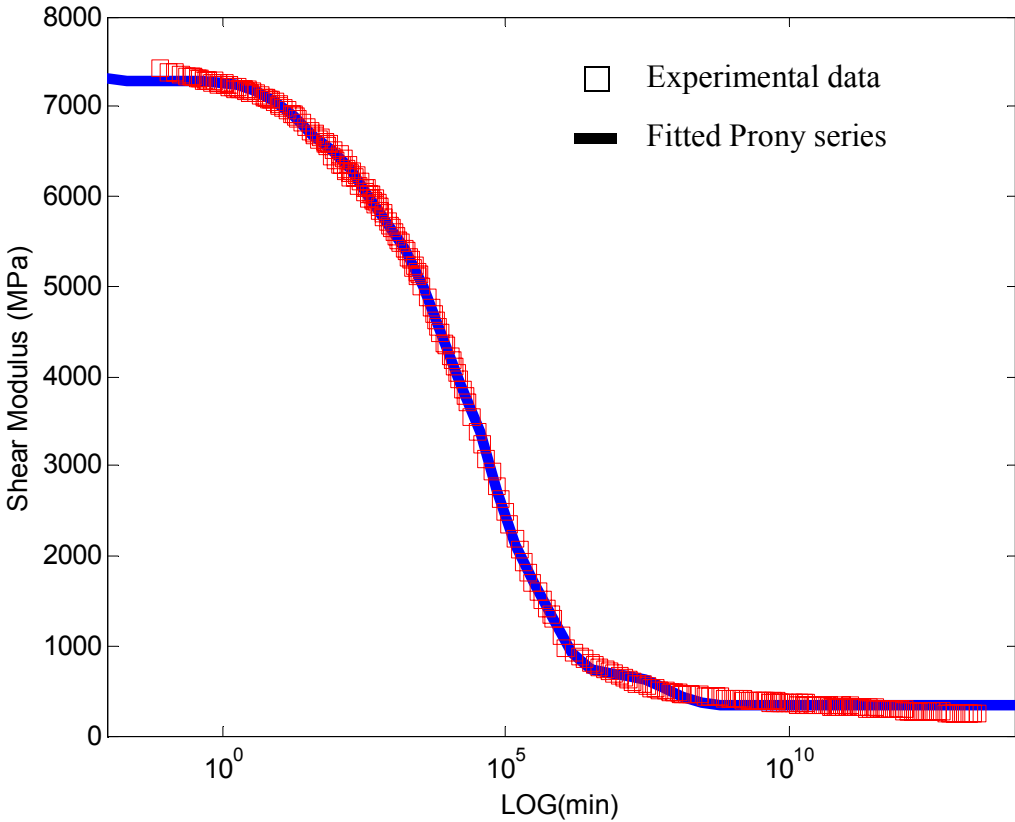
Figure 3.6   Plot of experimental (squares) and fitted (line) relaxation modulus.

CHAPTER 4

SIMULATION OF TRANSFER MOULDING

This chapter presents simulations of the transfer moulding process used to package the MEMS devices in question. The simulations were conducted to learn more about the moulding process in MEMS packaging. The predictions from the CFD software, C-Mold, were compared to experimentally determined melt-front advancement. The components were moulded under well defined process conditions. Two products with different topologies were chosen for the experiments. Both components had a mixture of thin- and thick-walled geometry. A favourable agreement between the simulations and the experiments was noted for one of the components. Lesser agreement was found for the other component.

Synchronous cavity filling was obtained by balancing of the runners.

The content and results of this chapter was published at the 38th IMAPS Nordic Annual Conference [87].

4.1 INTRODUCTION

To be able to predict possible problems with encapsulation already in the design phase has been a long sought-after possibility for engineers. Modern microelectronics companies have begun to introduce an increasing amount of sophisticated computer programs to accomplish their work and thus reducing time and money spent during the development and production set-up. Traditionally, the selection of the epoxy materials as well as the mold-design and process-design for microchip encapsulation has usually been determined based on experience and intuition. A method which can be costly and time consuming.

Modern software packages, both CFD and FEA, can together enligthen and help to solve many problems. There are numerous examples of the usefulness of such tools, amongst these are studies of packaging stress [56], [57], solder joint fatigue [58], thermal management [59] etc.

The motivation for the work presented in this chapter was to evaluate the usefulness of a plastic processing CFD in a MEMS production line. The objective was to evaluate if possible problems could be discovered in advance by the use of such tools. The melt front advancement was simulated using the commercially available C-Mold code. The results were then compared to a series of short-shots made in production. As described below, two products were chosen for the experiment.

Synchronous cavity filling can be highly desirable for multiple reasons, including polymer transfer control. Simulations were set up to investigate the possibility to achieve this.

4.2 TRANSFER MOULDING

Figure (4.1) shows a modern transfer moulding machine.
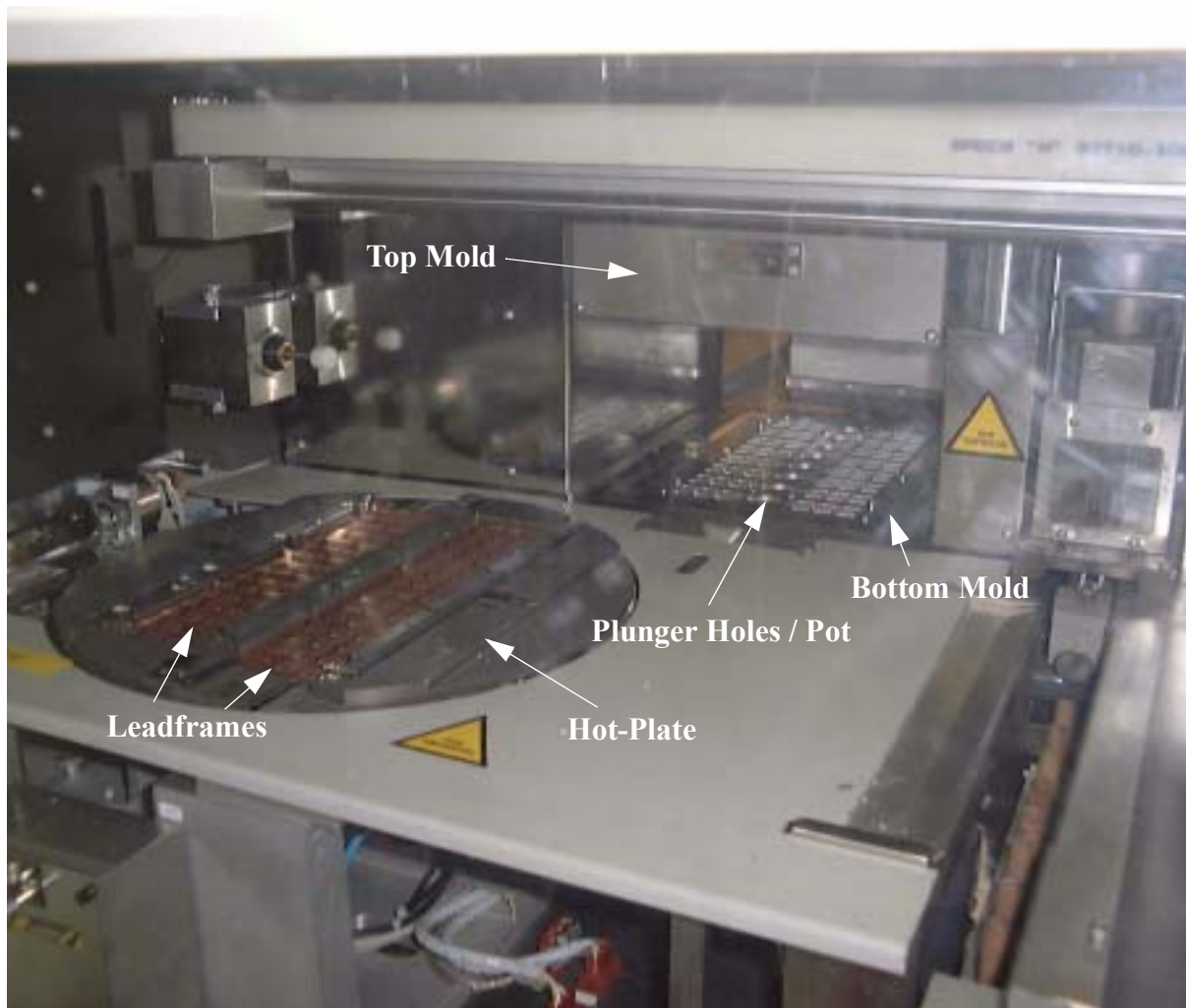
Figure 4.1   A modern Transfer Moulding machine with a hot-plate for preheating leadframes.

    The operation begins with the loading of chip-wire-leadframe assemblies into the transfer moulding machine. Two frames are placed on a hot-plate for preheating. From there they are transferred to the mold together with the EMC-pellets. The pellets are dropped in the transfer pot. The mold then closes and a delay of up to 15 seconds follows to let the moulding compound preheat to the moulding temperature. Next comes the injection, or transfer, of the moulding compound into the mold, followed by an in-mold curing period of typically 90 seconds. The mold then opens, the assemblies are ejected and the leadframes are picked up by a robot and brought to post curing. More information on transfer moulding can be found in [60] and [22].

4.3 EXPERIMENTAL

4.3.1 Material Data

The parameters for the cure kinetic model that was input to the plastic processing CFD software are shown in Table (4.1) (for details of the model see Section 2.3.1). The data was obtained at AC Technology Polymer Laboratory.

Table 4.1: Cure Kinetic Model Parameters

Parameter	Value
n	1.12428
m	0.36219
A_1	0.1
A_2	4511360
E_1	19981.9
E_2	8280.4
c_{gel}	0.644625

The parameters that were input to the modified Cross based viscosity model are shown in Table (4.2) (for details of the model see Section 2.3.2). These data were also obtained at AC Technology Polymer Laboratory.

Table 4.2: Reactive Polymer Viscosity Parameters

Parameter	Value
d	0.6114
ϑ^*	$7.3909\Delta10^{-5}$
B	0.1
T_b	4511360
C_1	19981.9
C_2	8280.4

It is noted that the material samples that were used at the external lab were from a different material batch than the material that was used for the moulding experiments.

4.3.2 Process Conditions

The process conditions that were used in the software are shown in Table (4.3).

Table 4.3: Process Condition input to the software

Transfer pot temperature	175°C
Delay time in the pot	7s
Melt initial degree of cure	0.1
Fill time	8s
Hold time	90s

4.3.1 FEM Simulation

The plastic processing CFD software enabled modelling of runners, cooling channels, polymer inlets, wires, leadframe and a number of other features that contributed to the accuracy of the simulation. The CFD software was not capable of doing full 3D modelling, but used a so called 2.5D approach (layered shell elements.) The geometric 3D to 2D simplification done by the CFD software is illustrated in Figure (4.2). With these simplification, only half the thickness had to be integrated and solved during the solution phase.
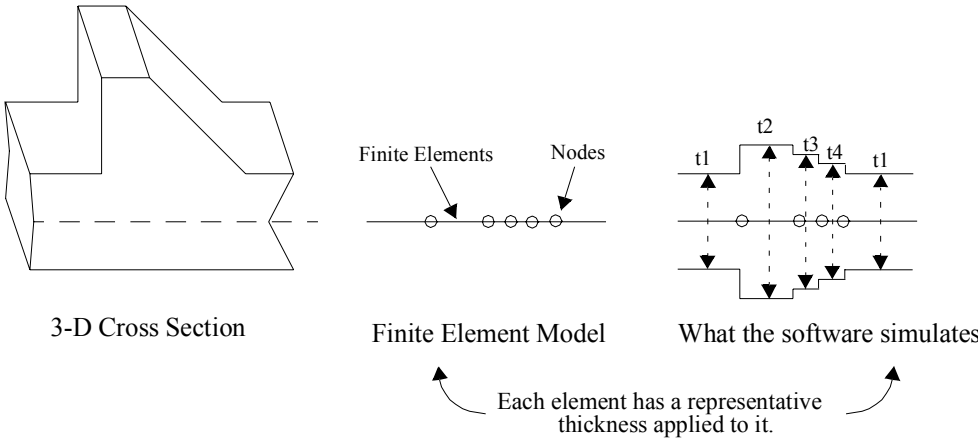
Figure 4.2   Illustration of geometric simplification done by the CFD software.

4.3.2 The Two Geometries.

Two products of different geometry was used for the experiment. It is important to understand the differences between the SOP used for MEMS and that used for ICs. Figure (4.3) and (4.4) clearly show that the MEMS device (sensor die) is about three times higher than the ASIC. This means that a SOP used for MEMS packaging has to be higher than that used for the ICs.

4.3.2.1 Geometry I.

The shape of Geometry I is shown in Figure (4.3). The amount of EMC on each side of the lead-frame was almost equal.
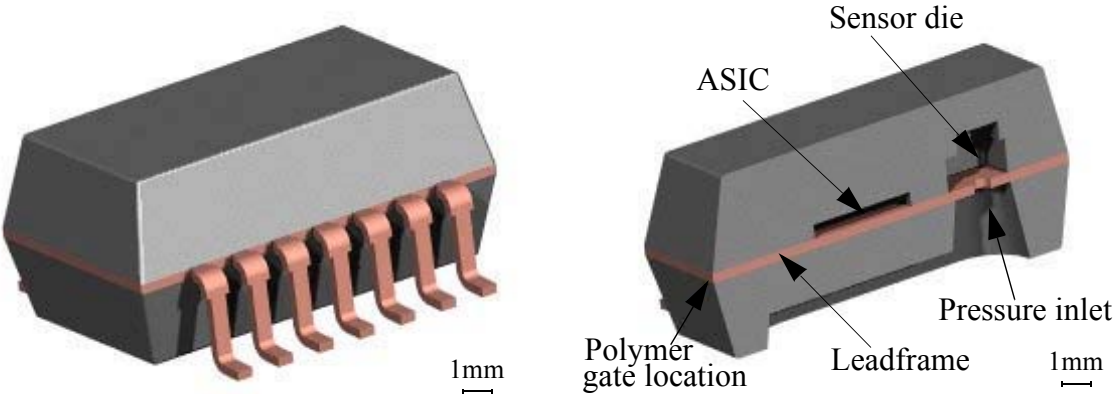
Figure 4.3   Geometry I with a x-section view.

4.3.2.2 Geometry II.

Geometry II had the shape shown in Figure (4.4). The amount of EMC below the leadframe was less than that above the leadframe. The schematic shows that the EMC below the leadframe is about half the thickness of that above the leadframe.
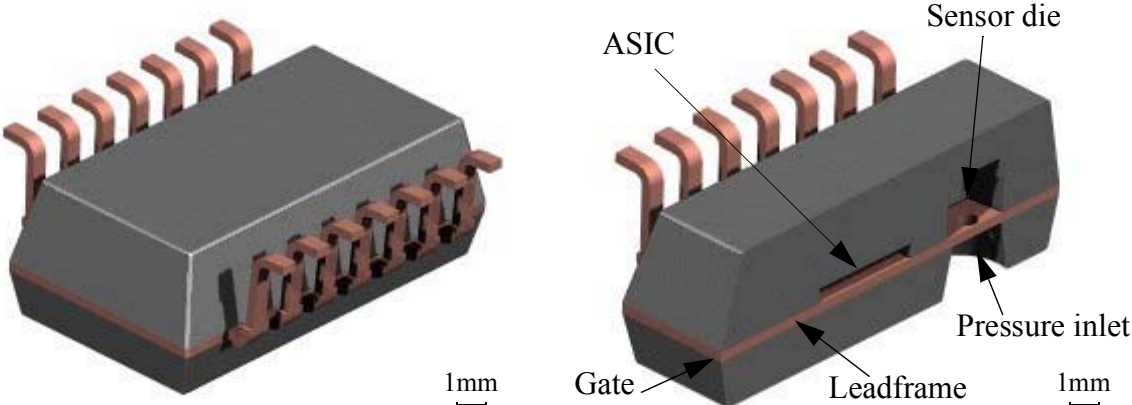
Figure 4.4   Geometry II with a x-section view.

4.3.3 The Model

Figure (4.5) shows that the chips were moulded in a multiplunger mold. Each plunger fed a total of 12 dies, 6 on each opposing leadframe. In other words, there were 8 equal and separate units consisting of 12 dies each (dashed rectangle). Each unit was associated with one plunger. The figure also shows that each unit had symmetry both horizontally and vertically with respect to the residual material from the transfer pot, the cull, (white dotted lines.) This meant that only 3 dies had to be modelled which reduced computational time without loss of information.
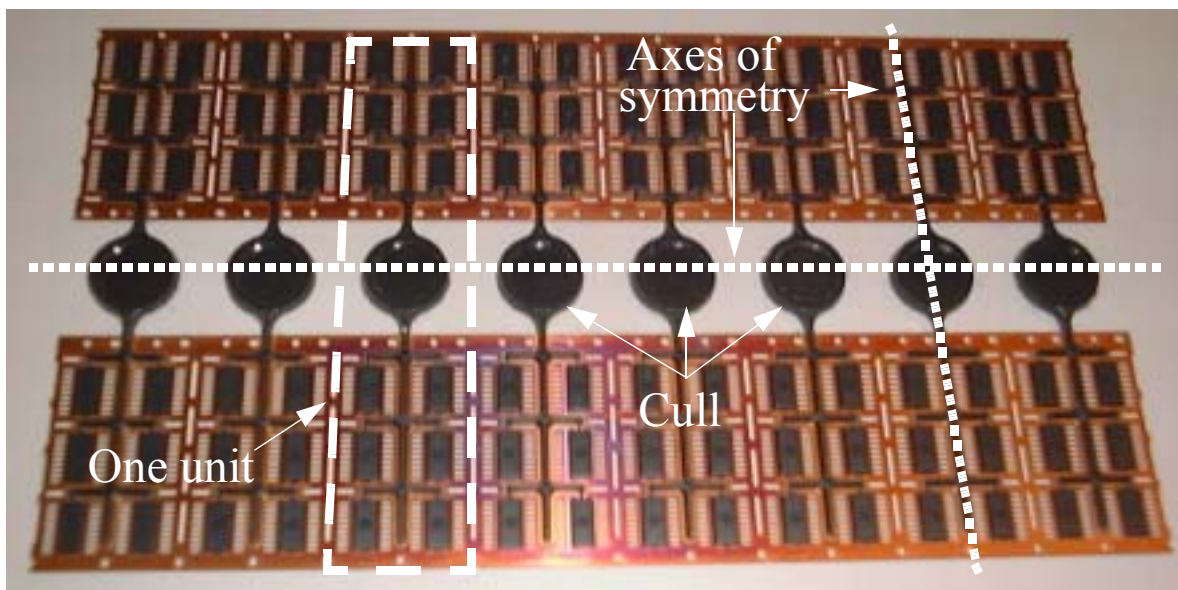
Figure 4.5   Leadframes after in-mold curing.

4.3.4 The Finite Element Mesh.

Figure (4.6) shows a plot of mesh thickness for geometry I. The mesh was thinner over the sensor and the Application Specific Integrated Circuit (ASIC) because there was less room (for the polymer) between them and the mold wall than between the leadframe and the mold wall.
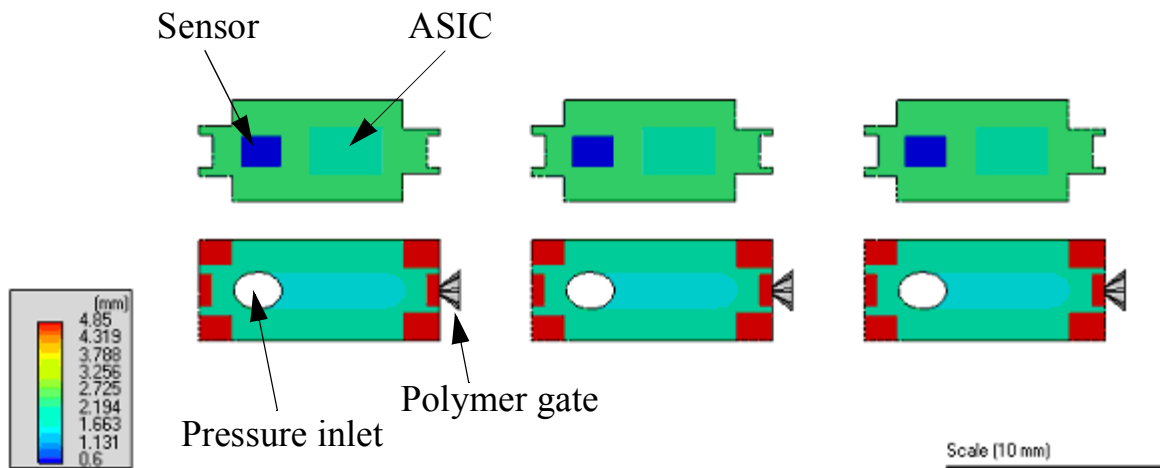
Figure 4.6   Mesh thickness for all three chips. Each colour represents a thickness. Note that the missing edges in the top cavities represents apertures in the leadframe.

The leadframe essentially divides the mold-cavity into two separate cavities, one above and one below it (see Figure (4.3) and Figure (4.4) for a reminder). In the CFD software this had to be modelled as two separate cavities because it used shell elements. A feature called *connectors* was used to couple nodes in one cavity of the model to the other. The ASIC and sensor can be observed in the top cavities, whereas the pressure hole and the gate are illustrated in the bottom cavities. The runner system is not shown in the plot. Figure (4.7) shows the element mesh. A fine mesh was used to best model sharp topological changes. Only triangular shell-elements with automatic meshing routine was available in the CFD software.
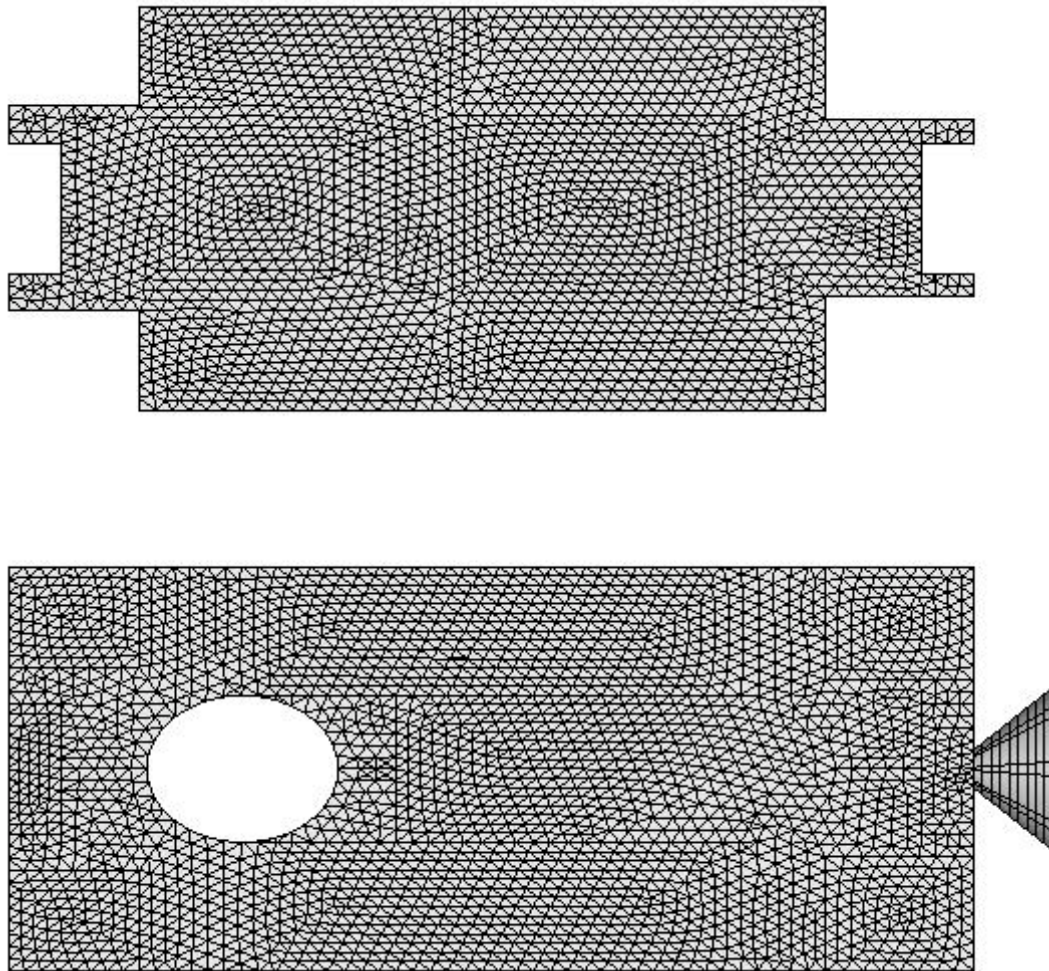
Figure 4.7   A fine element mesh was used trap the geometry irregularities.

4.3.5 The Mold Cavity Filling from the Theoretical Standpoint.

The CFD software is able to handle a three-dimensional, thin cavity system. The filling of the mold was modeled by a generalized Hele-Shaw (GHS) flow of an inelastic, viscous polymer melt or resin under non-isothermal conditions [46]. The solution was based on a hybrid finite-element/finite-difference method in order to solve for the pressure, flow and temperature fields, and a control-volume method to track the moving melt fronts [47]. It used finite elements to describe the planar coordinates whereas the gap wise and time derivatives were expressed in terms of finite differences [48].

The CFD software assumed thin walled components in line with the Hele-Shaw flow model. It also assumed a fully developed fountain flow. The definition of thin walled is not straight forward. It depends on the polymer Reynold's number (an hence the viscosity) as well as the height, width and length of the cavity and process parameters. The concept of Hele-Shaw flow refers to the flow between plates close together. It is understood that the width of the gap is much smaller than the typical dimensions of the flow. Since the separation between the surfaces are typically much smaller than the other dimensions, one expects the flow at a given point to

be mostly influenced by the local geometry. Therefore, the lubrication approximation can be applied [73]. The velocity component in the gap-wise direction is neglected and pressure is a function of planar coordinates only.

The high viscosity of a polymer melt justify the assumption of a fully developed Hele-Shaw flow where inertia and gravitational forces are much smaller than viscous forces. The flow kinematics are shear-dominated and the shear viscosity is taken to be both temperature and shear rate dependent. Because of these approximations, the generalized Hele-Shaw model can not predict the exact flow field near the advancing flow front or at the edges of the mold. The equations that describe the GHS polymer melt flow in a thin walled cavity is;

$$
\frac{\partial}{\partial x}\left(S\frac{\partial P}{\partial x}\right) + \frac{\partial}{\partial y}\left(S\frac{\partial P}{\partial y}\right) = 0 \tag{4-1}
$$

where S is the flow conductance which is defined as $S = \int_{0}^{h}\frac{z^2}{\xi}dz$, P - the pressure, x & y -

planar coordinates, z - gapwise coordinate, h - half-gap of the cavity and ξ - viscosity which is modelled by Equations (2-1) through (2-6). The equation is valid when assuming zero pressure along the meltfront and the flow rate through the gate is known.

It is noted that the governing equations neglect the effect of normal-stress and memory effects associated with fluid elasticity [49]. More information on computer aided plastic processing simulations and GHS can be found in [73].

4.3.6 Short-Shot Moulding.

Stopping the polymer transfer at prescribed positions during the polymer injection is called short-shot moulding. This technique was used to compare the production results to the simulated results. A short-shot session was performed for both products in question. Figure (4.8) illustrates the results for geometry I. Figures (4.9) show the result for geometry II.

Each shot is presented with the meltfront-advancement in the cavity below and above the leadframe. These are presented in the right and left small-photos respectively. The plot for the corresponding software simulations is presented below the short shot photos. The first shot in Figure (4.8) illustrates this further.
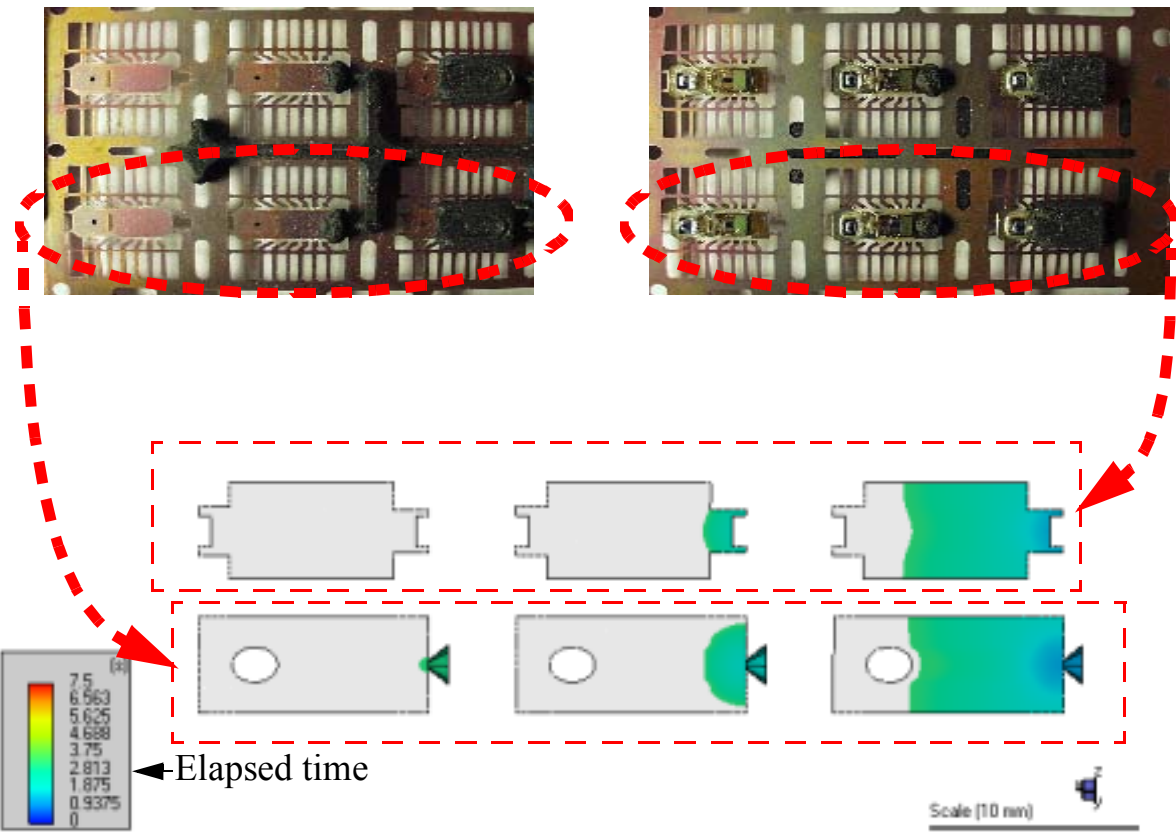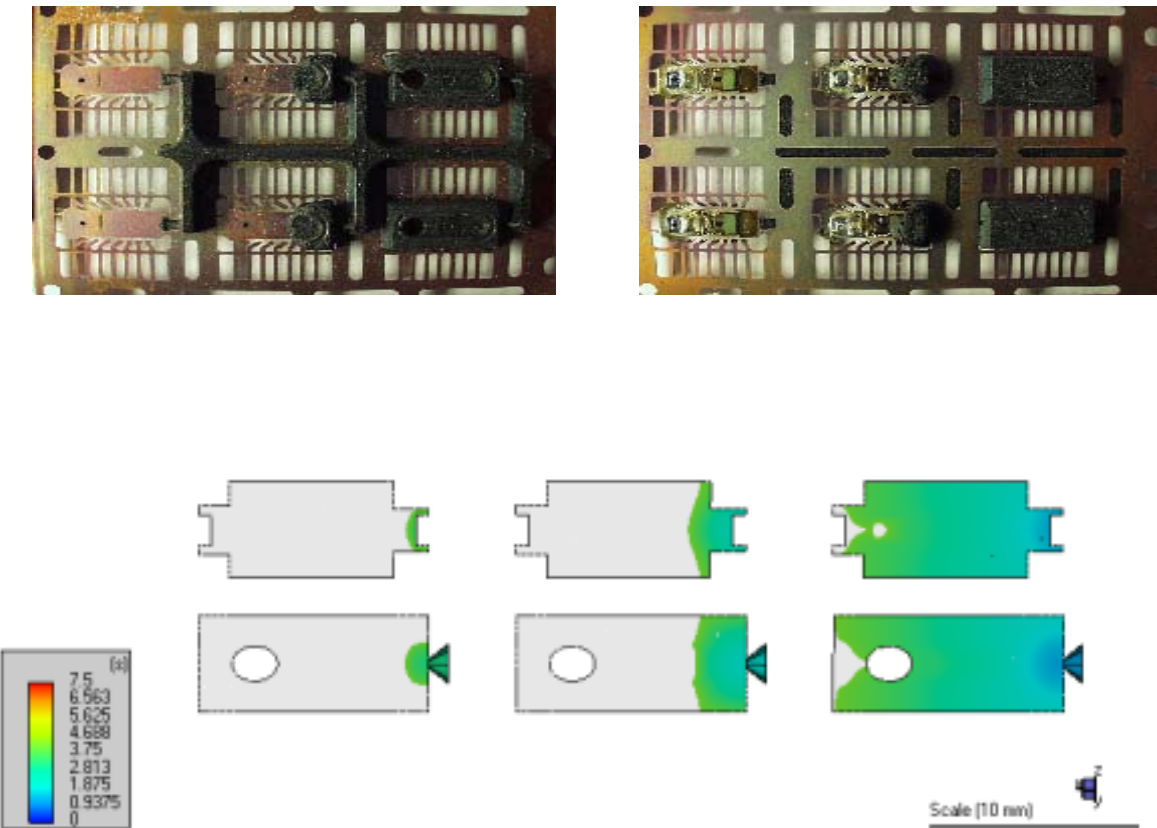
Figure 4.8   Short-Shot session for geometry I.

Shot 3
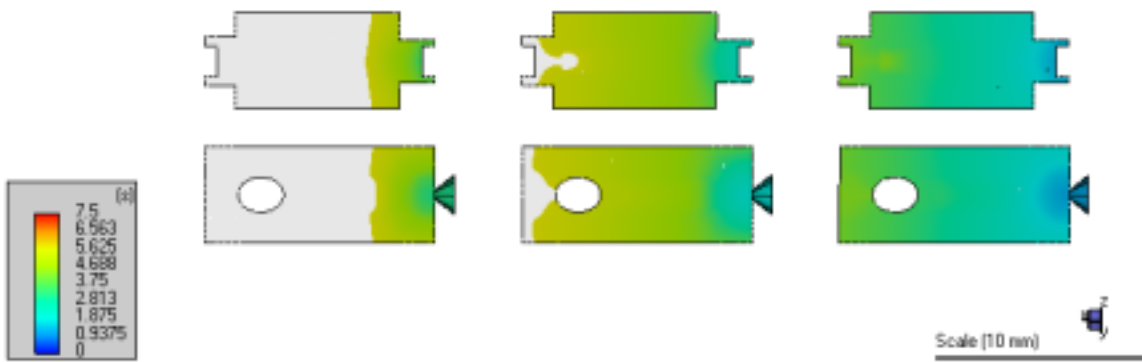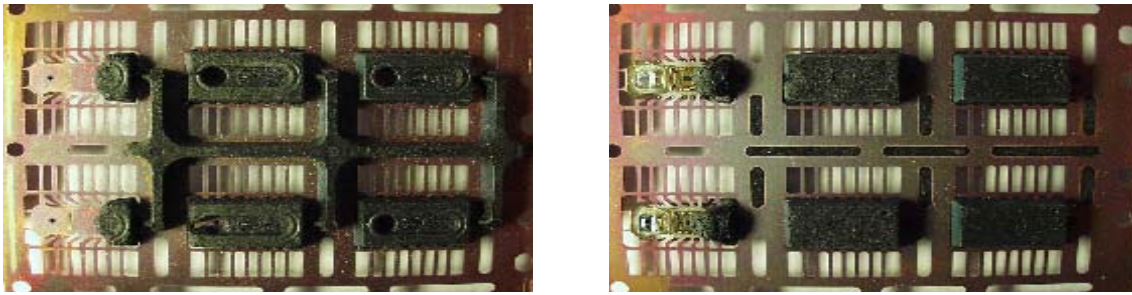
Shot 4
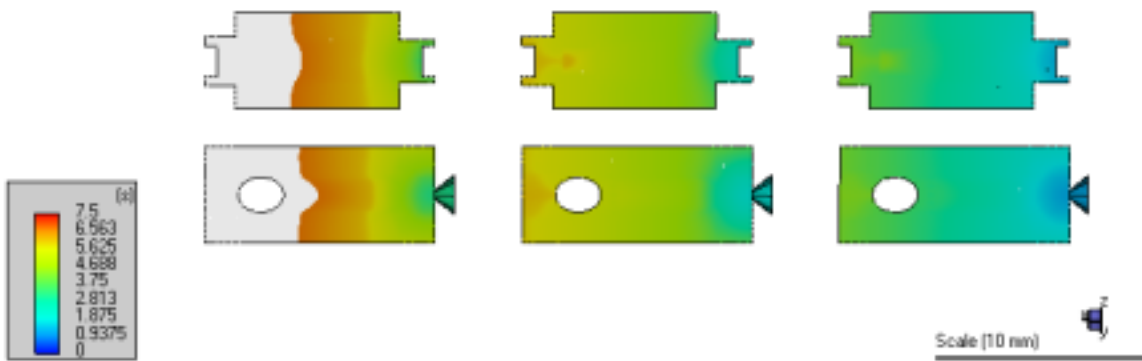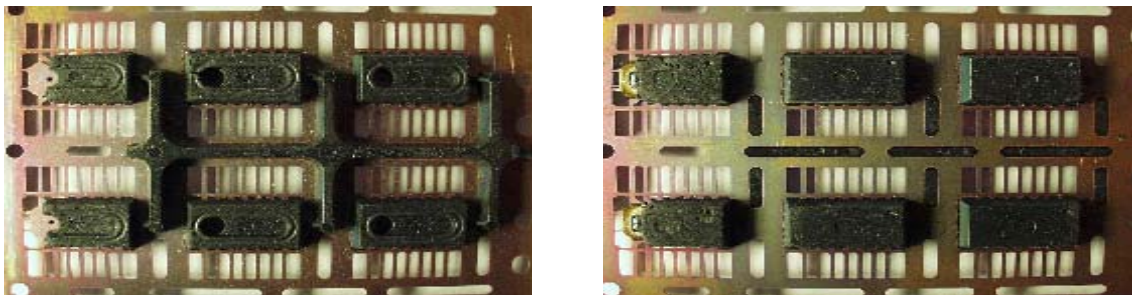
Figure 4.8   Short-Shot session for geometry I.

Shot 1
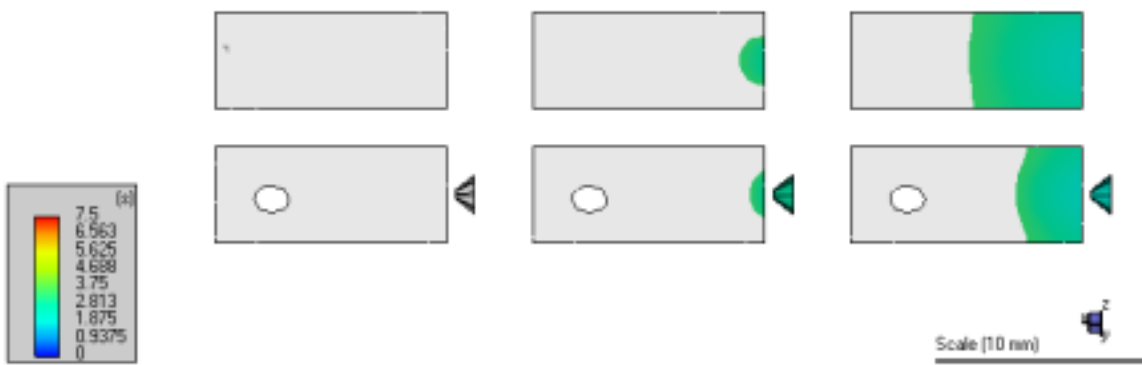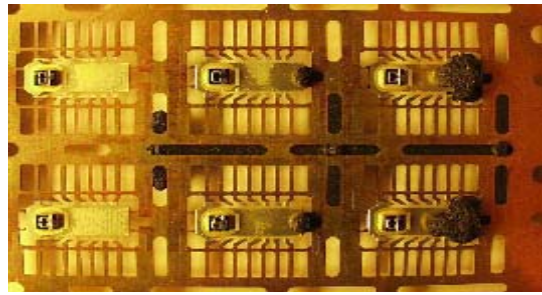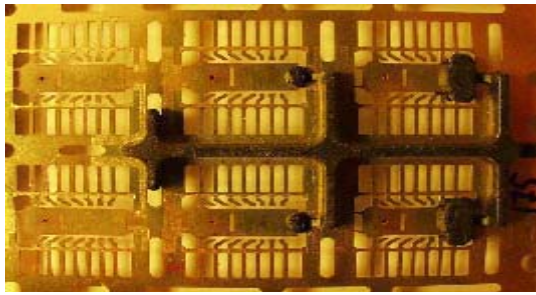
Shot 2
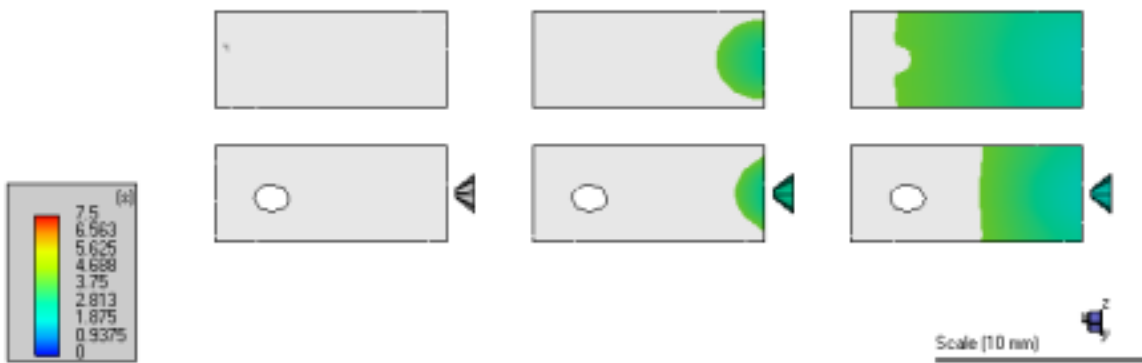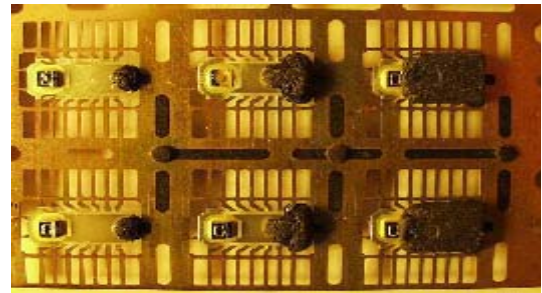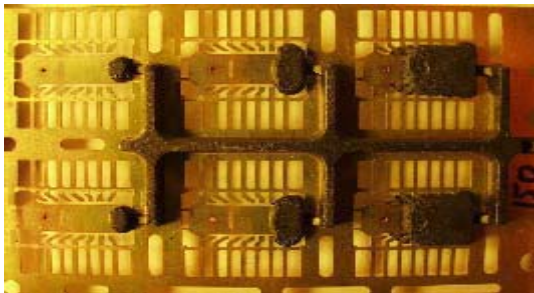
Figure 4.9   Shot-Shot session for geometry II.

Shot 3
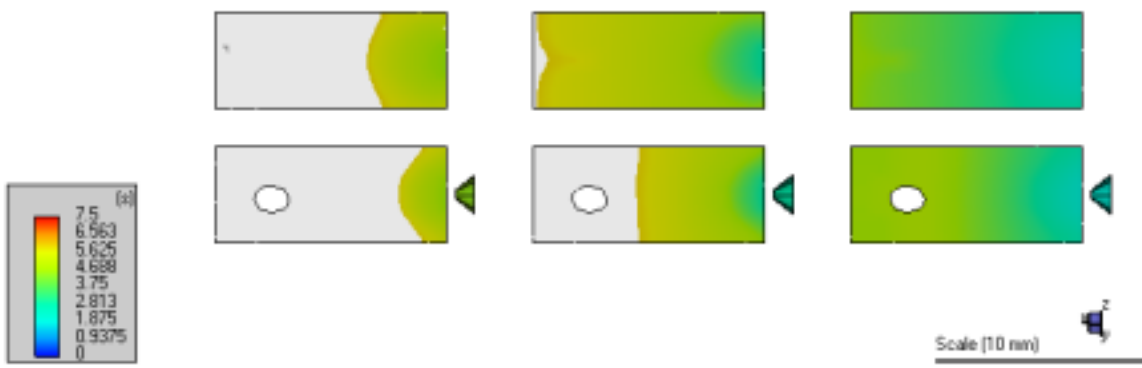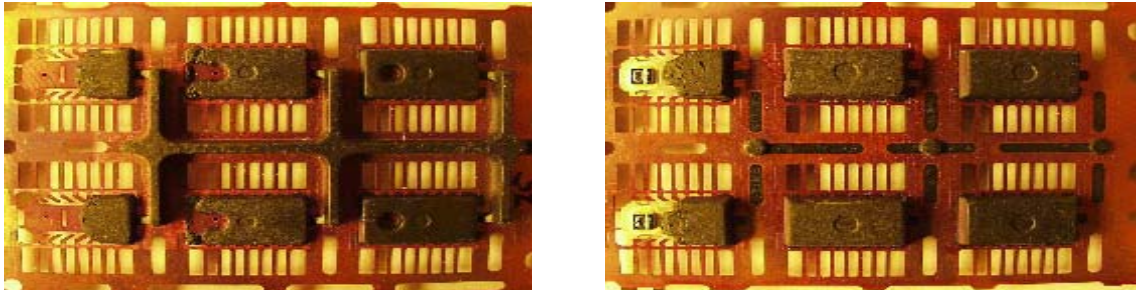
Shot 4
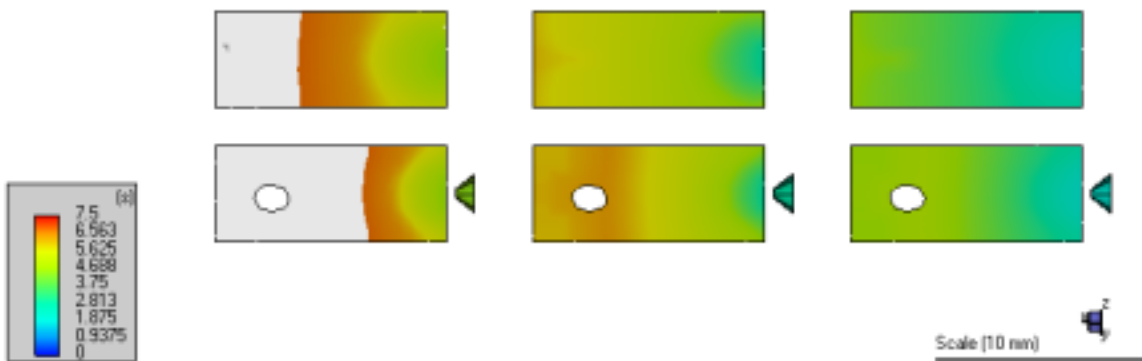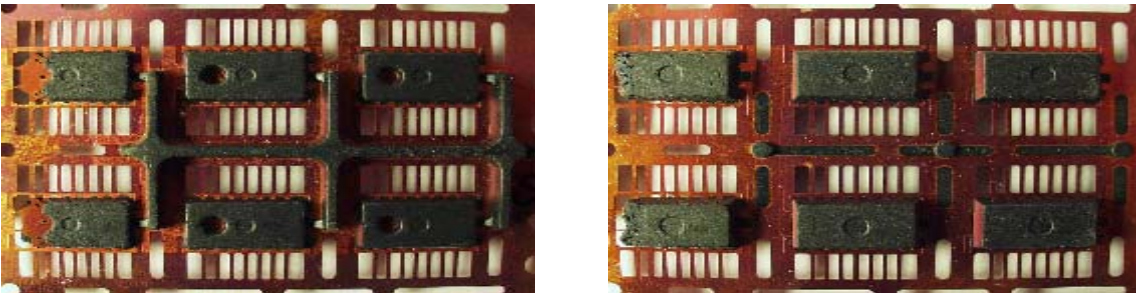
Figure 4.9   Shot-Shot session for geometry II.

4.4 RESULTS AND DISCUSSION

4.4.1 Melt-Front Advancement

4.4.1.1 Geometry I.

Figure (4.8) shows pictures of the shots made on the transfer moulding machine with the corresponding simulated results. Moulding and simulation agreed to a satisfactory level. Slight deviations were observed, like in shot 4. The discrepancies between the short-shots and the simulations were minor and did not affect any conclusions.

4.4.1.2 Geometry II.

Figure (4.9) shows that the top cavity filled much quicker in the simulations than in the Moulding experiment. The discrepancies between the simulated result and the experimental results for geometry II were much larger than for geometry I. None of the short-shots matched the simulations. A closer inspection of the short-shots revealed that the flow patterns and the shape of the flow-fronts in the top and bottom cavities respectively were completely different (discussed later).

An analytical solution [73] to the velocity profile of a simple flow in the cavity given in Figure (4.10) was utilized to determine its sensitivity to thin/thick walled structures. Isothermal conditions and a Newtonian flow was assumed.
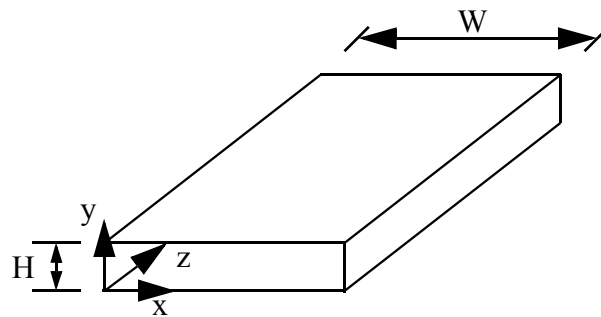
Figure 4.10   Schematic of thin walled cavity.

The governing equation was set up for v_z:

$$-\frac{\partial P}{\partial z} + \sigma\left[\frac{\partial^2 v_z}{\partial x^2} + \frac{\partial^2 v_z}{\partial y^2}\right] = 0 \tag{4-2}$$

where $\partial p / \partial z$ is a constant. The boundary conditions are:
$$v_z|_{x=0} = 0$$
$$v_z|_{x=H} = V_z$$
$$v_z|_{y=0} = 0$$

$$v_z / W3y0 = 0$$

which had the following solution [73]:

$$v_z = -\frac{H^2 \in P}{2\sigma \in z}\left[\bullet^2 - \bullet + \frac{8}{\phi^3} \overset{\leftarrow}{\underset{i=1333...}{\rule{1.5cm}{0.4pt}}} \frac{\cosh \Psi i\phi/\theta - 0.500\,\aleph u \beta}{i^3 \cosh//i\phi0\,\aleph 2a00}\sin/i\phi\bullet 0 \right] \tag{4-3}$$

where $\theta = x/W$, $\bullet = y/H$ and $a = H/W$ [73]. The velocity profile for v_z could then be plotted for different aspect ratios, a, of the cavity.

The cavities in geometry II were measured and found to be approximately 6x1.1x11mm for the bottom cavity and approximately 6x2.4x11mm for the top cavity. In terms of Equation (4-3), this gave the velocity profiles plotted in Figure (4.11) below.

a) Top cavity	b) Bottom cavity
Thick Walled, H/W=0.4	Thin Walled, H/W=0.15
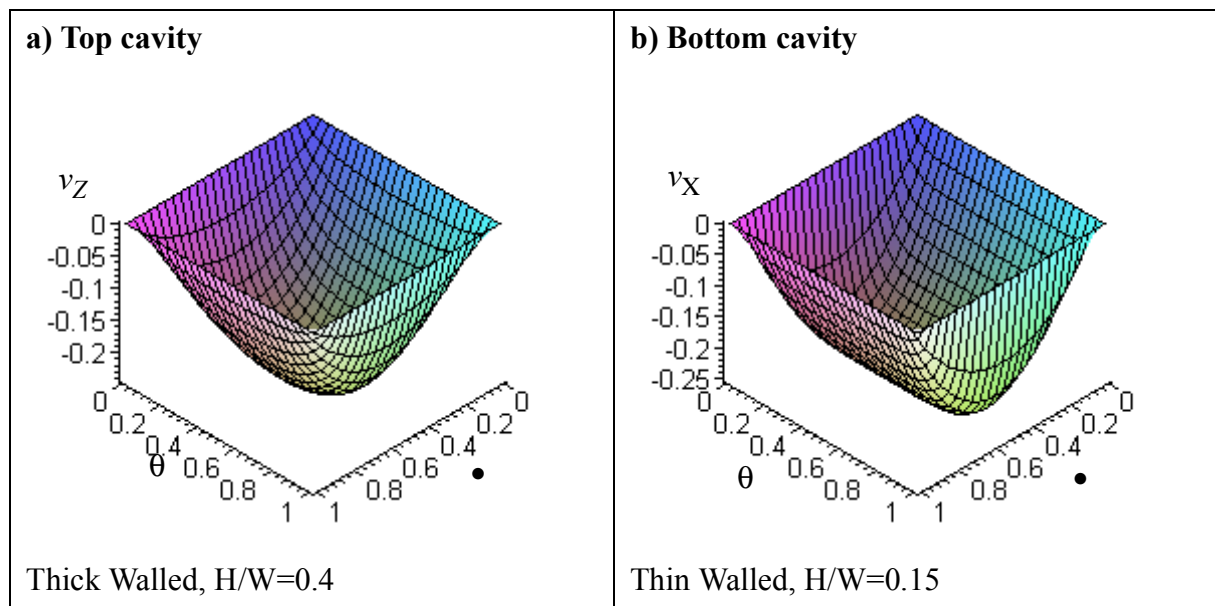
Figure 4.11   Comparison of polymer flow equation in Thick- and Thin walled cavities.

Figure (4.11) shows that edge effects are kept to a minimum by keeping the cavity narrow. It also show that for thicker walled cavities, the edge effects extend far into the flowfield.

An interesting difference in the flow pattern was observed when studying the flow fronts in top and bottom cavity of geometry II. Figure (4.12)a&b shows pictures of the flow fronts in the top and bottom cavities respectively.

a) Top cavity	b) Bottom cavity
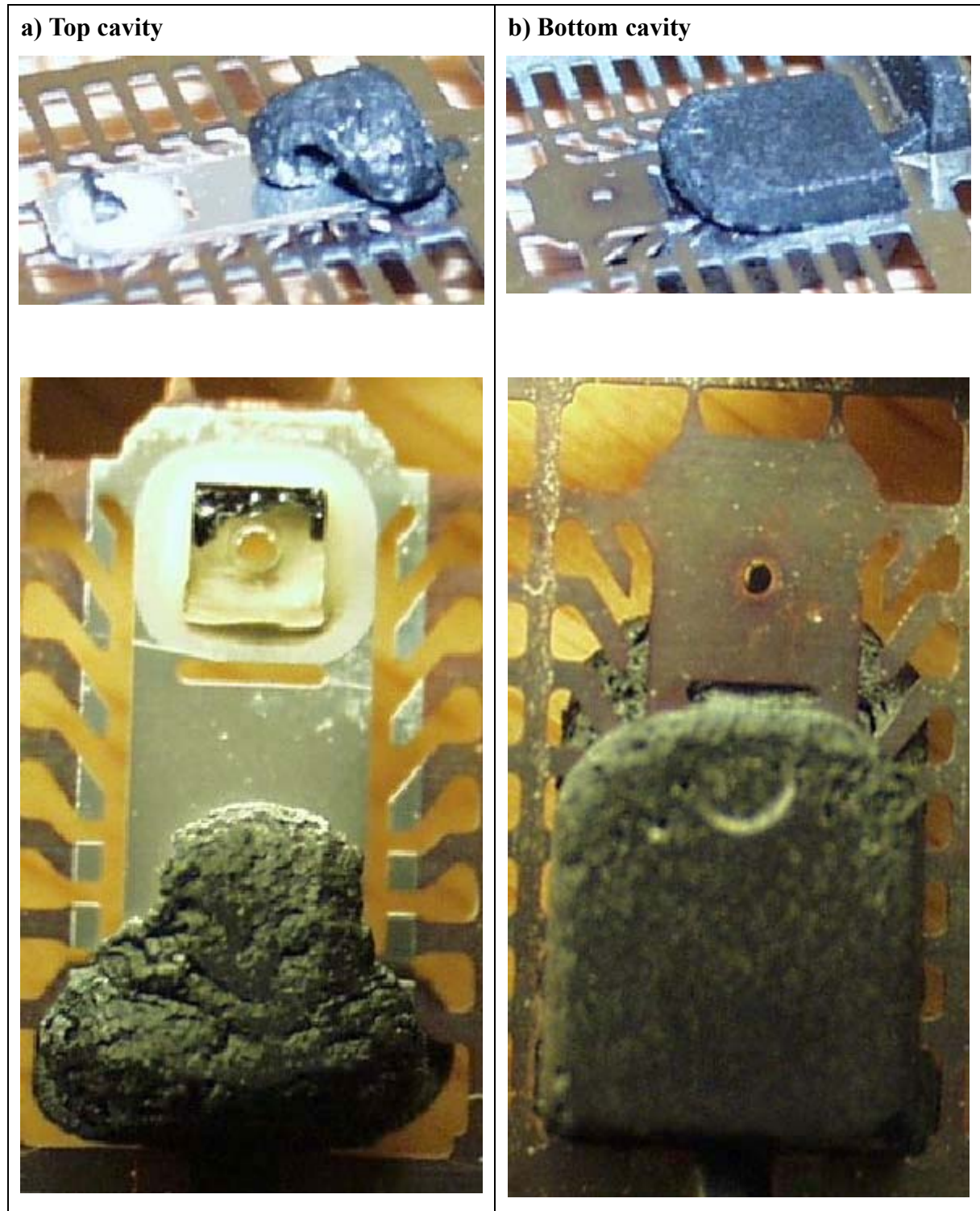
Figure 4.12   Flow patterns for geometry II from the experiment. Note that each column represent the same actual shot. The colour difference is due to different lighting.

The bottom cavity, (right column), showed a fully developed flow in a thin walled cavity. This complied with the GHS flow and one would expect the software to predict the flow well. Inspections revealed that the flow pattern complied to that predicted by the software. The absolute advancement of the melt front was, however, not correct due to issues with the top cavity not complying to GHS assumptions and the use of a common gate.

The top cavity (left photos) showed a flow that did not fulfil the GHS approximations. Out-of-plane velocity components, 3D effects, were clearly observed. This was a result of the thick walled cavity in combination with a limitations posed by the gate design.

Gate design has a large influence on the flow and hence the software predictions. The gates in the microelectronics industry have strict design rules for easy breakage and estetic reasons. This makes a working design undesirable to modify. The most common gate design used in Microchip encapsulation is the edge gate. These gates cause problems because of their sharp edges. These gates have been known to cause trouble in thermoplastic injection moulding. The problem is the discontinuity in the pressure field at the gate/cavity interface. The polymer is injected straight into an empty cavity, and jetting can occur [61]. Figure (4.13) shows a schematic of the jetting phenomena with one solution to the problem.
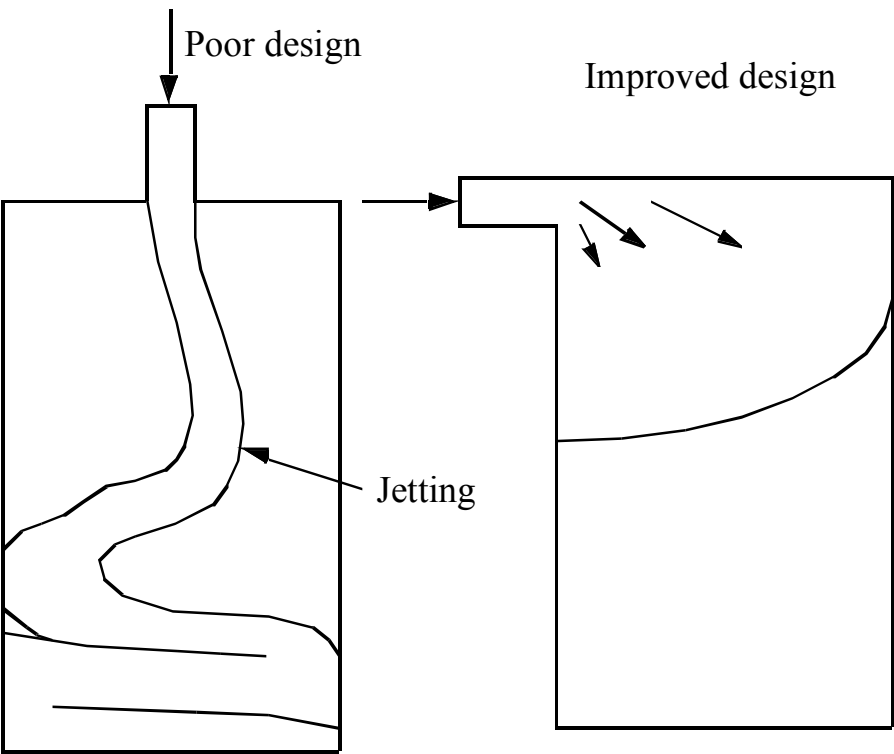
Figure 4.13   Schematic of the jetting phenomenon and one improved design.

The "curly" flow front observed in Figure (4.12) could be the result of this phenomena.

There are two common ways to overcome the jetting problem. One is to avoid the sharp edges of the gate to give the polymer room and time to expand. The other one is to force the polymer to impinge on an obstruction to break up the jet. Figure (4.13) shows how the mold-wall acts as the obstruction.

Figure (4.14) shows a short-shot from geometry II. Although the CFD software failed in predicting the flow, it did capture the effect of unbalanced filling in top and bottom cavity.
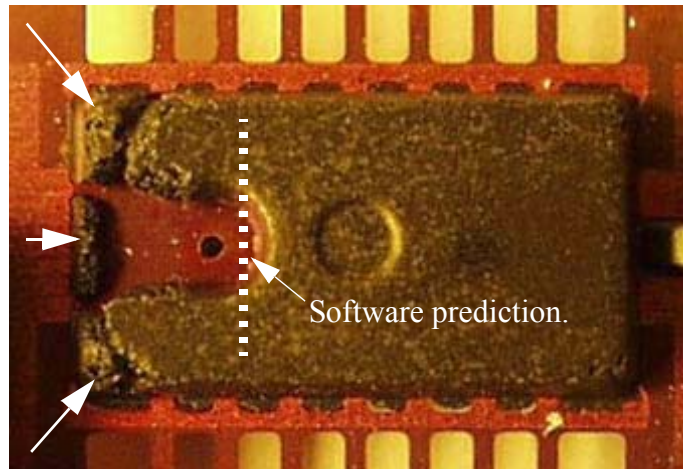
Figure 4.14   Picture showing that the top cavity is full and the polymer is coming down to the bottom cavity.

The white arrows indicate where the polymer came through the leadframe because the top cavity was full. This was predicted by the software, but the location of occurrence did not match. Figure (4.15) below shows a schematic of the flow situation discussed above. The situation is unwanted as it can trap air and cause internal and/or external voids in the plastic capsule.
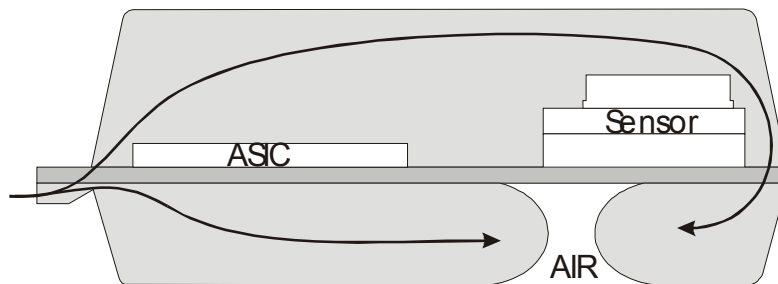
Figure 4.15   Schematic of the unbalanced filling observed for *geometry b*.

Geometry I showed very good agreement between experiments and simulations. Both top and bottom cavity of this chip were thick. Evidence of the "curly" flow was observed for both the top and bottom cavity of geometry I (not shown here). It was believed that the predictions were good regardless of the incompatibility to the GHS assumptions because the volumes of the top and bottom cavities were nearly the same.

4.4.2 Balancing the Filling of the Cavities

Balancing of the filling of the cavities is desirable for several reasons including:

- Meltfronts reach the different sections simultaneously.
- Longer average cavity fill times without increasing the total fill time.
- Equal compound property distribution for each cavity.

Problems relating to Glob-Top[1] being pushed off the sensor by flow-induced stresses from the passing EMC has sometimes caused problems. This was solved by decreasing the injection speed as the flow front reached the sensor. The problem was that the melt reached the sensors in each of the three chips at different times. This made it difficult to decide when to decrease the injection speed. One way to avoid this problem could be to fill each cavity at the same time, so called balanced filling.

The balancing itself can be done in many ways. The most obvious is to arrange the cavities radially around the transfer pot, but this would compromise too much of the efficiency. Other more compatible options include manipulating the cross section area of the runner to control the volume flow rates and pressure drops, progressive alteration of the sub-runners connecting the main runner to the gate or modifying the gate sizes to control the volumetric flow rate through them. The degree of modification plays an important role in choosing among the options, and this is where additional constraints apply. One of these is to maintain a uniform gate breakoff, both in appearance and in breakoff action. Excessively large gates will resist breaking and gouge a large chunk of the moulded body, leaving an unsightly gate vestige. More constraints like this needs to be taken into account before starting the balancing design. The best design gives a balanced filling yet satisfying all of the constraints with minimum degree of gate and runner modifications.

The software did not provide the option of automatic runner balancing for the Microchip Encapsulation module. The sub runners were modified manually until the filling was basically balanced. Figure (4.16) show the filling pattern after balancing. It is evident from the figure that the cavities filled almost simultaneously.
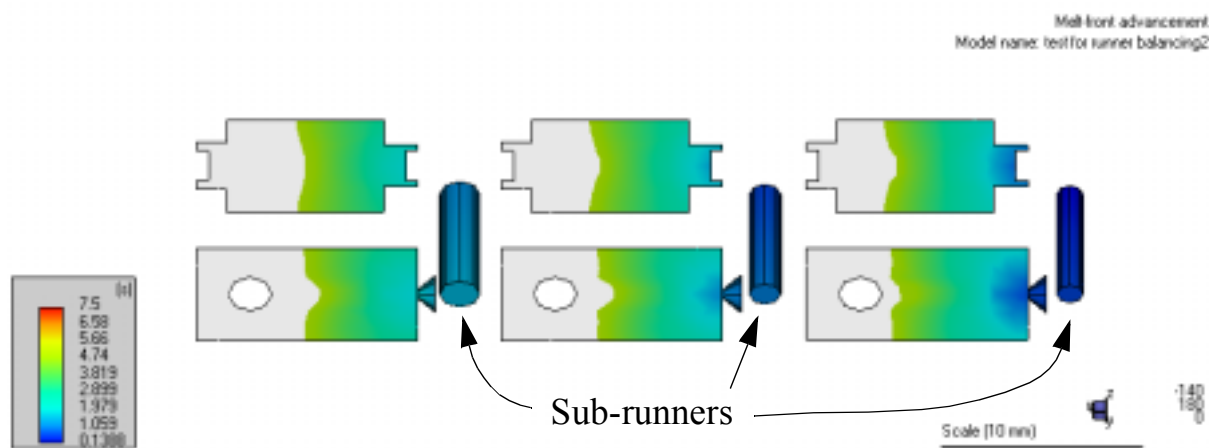
Figure 4.16   Balanced filling obtained by altering the sub-runner cross sectional areas for Geometry I.

---

1. Glob Top in normally a soft gel that is dispensed over fragile elements, in this case the MEMS transducer, to minimise and level out the stress acting on them from the package.

4.5 CONCLUSIONS

This chapter has shown that the CFD software C-Mold has limitations when used to predict mold filling for MEMS products. The geometry of the MEMS package violates the conditions required for the applicability of the GHS flow model. The gate design also present a problem in this respect. However, even with these limitations, the fitting of geometry I was well predicted compared to geometry II. This was explained from the fact that the volumes above and below the leadframe was balanced for Geometry I. A curly flow front was observed about 2/3 of the length of the cavity for both products. This was an indication of a non-zero velocity component in the gap-wise direction of the cavities. Such effects could not be simulated by the software. Geometry II had one cavity that was thin walled and it showed a good agreement with the simulations. It was concluded that the geometry of the MEMS packages in question was not suited for 2.5D simulation codes.

An automatic runner balancing routine did not exist within the software for the Microchip Encapsulation module. A balanced runner system was found manually by subsequently changing the sub-runner dimensions.

A CFD software capable of simulating 3D effects and free-surface problems would be more effective for MEMS device encapsulation modelling.

CHAPTER 5

CALCULATION OF PRESSURE SENSOR SIGNALS USING FEA

This chapter presents a novel method for obtaining accurate electrical sensor signals from a family of piezo-resistive pressure sensors. The method computes the resistance of the piezo-resistors by calculating the piezo-resistance in each finite element. Then an accurate total resistance is calculated as a function of pressure and temperature, from which the total transducer signal is calculated.

The main content and conclusions from this chapter was published at the 1st IEEE Sensors Conference [88]

5.1 INTRODUCTION

MEMS pressure sensors are used to monitor pressure in many areas such as medical and automotive [50] applications. One commercially available family of MEMS pressure sensors are fabricated from silicon and glass wafers, as shown in Figure (5.1). The silicon is etched to form a diaphragm. Implanted in the Si diaphragm are four piezo-resistors that are connected to form a Wheatstone bridge. The diaphragm is covered on top and bottom by borosilicate glass, as shown in Figure (5.2). This glass covering the diaphragm is denoted the level-0 package. On the top, the glass has an etched cavity above the Si membrane that forms a volume with a reference pressure. The bottom glass has a through hole that acts as a pressure inlet port.

A wide range of pressures are measured in automotive applications, ranging from 10 kPa to 180 MPa. This very broad span require different sensors for the different pressure ratings in order to have the needed sensitivities. To efficiently and successfully design a new pressure sensor for a specific application, a method has been sought that can predict the pressure sensor signal as a function of pressure and temperature before prototypes are manufactured.
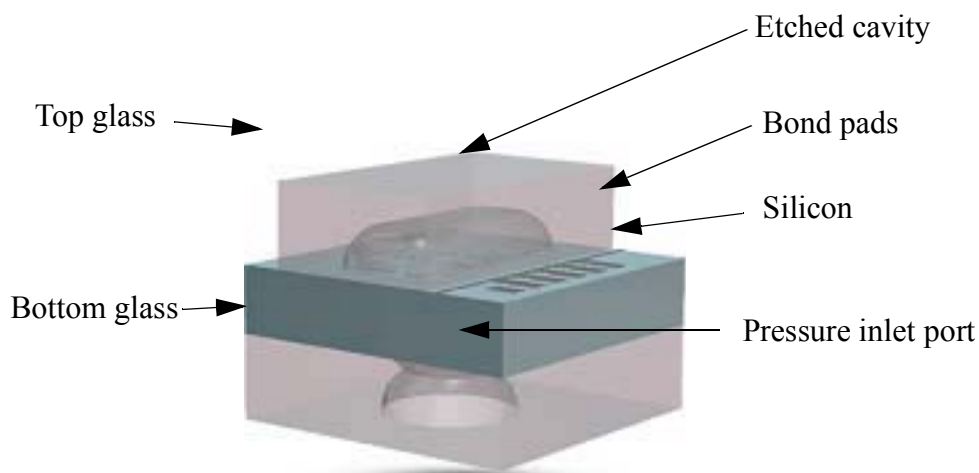
 Figure 5.1   Level-0 Packaged MEMS pressure sensor. Typical footprint of 1.5 x 2.0 mm and height of 1.5mm

The use of an analytical solution as developed by Gong and Lee [51], has too many limitations, including the exclusion of the level-0 packaging effect. The resistor layout varies significantly from one design to the other. The change in resistor location for different geometries is necessary to balance the bridge. A balanced bridge has a constant total resistance as a function of pressure and 2nd order piezo-coefficients cancelled.

Pressure measurements are made as follows: Gas pressure on the bottom side of the diaphragm causes deflection and hence stresses in the ion-implanted piezo-resistors in the top surface of the diaphragm. The concomitant change in piezo-resistance results in a change in the output signal of the Wheatstone bridge.

The objective of the method developed here was to make a relatively simple and accurate way to predict pressure sensor signals for the family of pressure sensors discussed above. The method established the relationship between the output from the Wheatstone bridge and the input pressure and operating temperature. This method was validated by comparison to the measured response of existing sensors. It can be used for designing new versions of the pressure sensors. Another possibility is to utilize it for parametric analysis. A third and novel use of the model is to indirectly measure packaging stress from the level-1 package.

5.2 THERMO-MECHANICAL SIMULATIONS

5.2.1 Material Modelling

5.2.1.1 Silicon and Borosilicate Glass

The material modelling was done using FEA software (ANSYS[TM] v6.1). Borosilicate glass (Corning 7740) was modelled as a linear isotropic material and silicon as a temperature dependent linear orthotropic material. The material data for Si is shown in Tables (5.1) and (5.2) and was found from reference [72]. The material data for glass is shown in Table (5.3). The two materials had different Coefficients of Thermal Expansion (CTE) even though glass was selected to match the CTE of silicon as closely as possible. This resulted in a CTE mismatch driven stress, as the operating temperature changed.

Table 5.1: Temperature dependent elastic constants for Silicon

	Temperature(°C)					
	-73	27	127	227	327	427
C_{11}	166.7E9	166.1E9	165.6E9	164.8E9	164.0E9	163.3E9
C_{12}	64.3E9	64.1E9	63.9E9	63.6E9	63.3E9	63.0E9
C_{44}	79.9E9	79.7E9	79.5E9	79.2E9	78.9E9	78.5E9

where C_{ij} are the elastic constants as defined in Section 2.9.

Table 5.2: Secant CTE for Silicon with reference temperature at 380°C.

Temperature(°C)	-40	-7	25	75	125
CTE (10^{-6}/°C)	3.27	3.37	3.45	3.56	3.65

Table 5.3: Material properties for glass.

Tensile Modulus (GPa)	62.75
Poisson Ratio	0.2
CTE (10^{-6}/°C)	3.25

5.2.1.2 Piezoresistivity in Silicon

Piezoresistivity is the fractional change in bulk resistivity induced by small mechanical strains applied to a material. Monocrystalline silicon has a high piezoresistivity and, combined with its excellent mechanical and electronical properties, makes a superb material for the conversion of mechanical deformation into an electrical signal. The resistance will change magnitude according to the following linear formula [52],

$$\frac{\div R}{R} = \phi_l \omega_l + \phi_t \omega_t \tag{5-1}$$

where ϕ_l and ϕ_t are the longitudinal and transverse piezo-resistive coefficients respectively as defined in Section 2.10. Table (5.4) below shows the piezo-resistive coefficient values used.

Table 5.4: Piezo-resistive coefficients as a function of temperature.

	Temperature			
	-7°C	25°C	75°C	125°C
ϕ_l ($1\Delta10^{-9} \text{Pa}^{-1}$)	0.7853	0.7048	0.6087	0.5367
ϕ_t ($1\Delta10^{-9} \text{Pa}^{-1}$)	-0.7251	-0.6508	-0.5621	-0.4956

The values were taken from reference [86]. It should be noted that the deflection of the diaphragm was large. A large strain solution was run in the FEA software.

In this work, Equation (5-1) was used to calculate the change in resistance for each finite element in the resistor. Finite elements with piezo-resistive properties were not directly available in the FEA software, but the resistance was obtained by proper post processing of the results. The stresses in the longitudinal and transverse direction, with respect to the current direction in the piezo-resistors, were extracted from each element within the piezo-resistor.

The total resistance of each piezo-resistor was calculated by considering each finite-element within the region of a piezo-resistor as a single resistor in a resistor network. The total resistance for a piezo-resistor was equal to the total resistance of the resistor network. All these calculations were done in the APDL macro language of the FEA software.

5.2.2 Geometry of the Model

The geometry of the finite element model was based on level-0 packaged sensor dies manufactured by SensoNor asa, see Figure (5.1). Figure (5.2) shows a mid-plane sectional view of the pressure sensor.
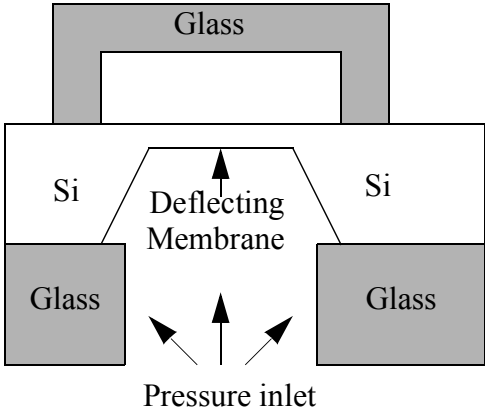
 Figure 5.2   Schematic of MEMS pressure sensor die.

An ideal sensor is symmetric along the mid-plane cross-section seen in Figure (5.2). Since this method was developed to take into account production inconsistencies like mask misalignment and etch time variability, a full model was built. The parametric input variables were mask dimensions, mask coordinates, including mask rotation, and etch time for the different masks. The outer dimensions, or the dimensions of the package, were also parameterized. Figure (5.3)a

shows a cross-section of the geometry model of the pressure sensor cut at the symmetry plane of an ideal sensor. Figure (5.3)b shows the silicon diaphragm with the implanted piezo-resistors.
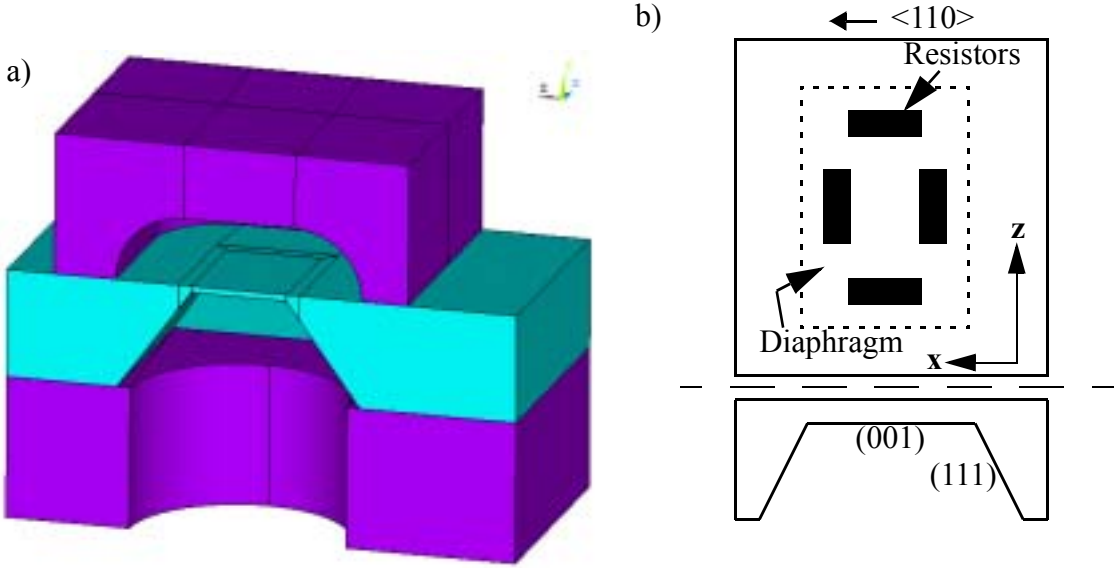
Figure 5.3   a) Solid model cross section, b) Sketch of membrane & resistors with portion of surrounding Si. The Miller indices are indicated on the sketch.

5.2.3 Finite Element Model

The resistors and most of the exterior of the level-0 package was hexahedral meshed with 20-node brick elements (Figure (5.5)). The rest of the geometry was meshed using 12-node tetrahedral elements (Figure (5.4)). The total number of elements was 15017 giving 44258 nodes.
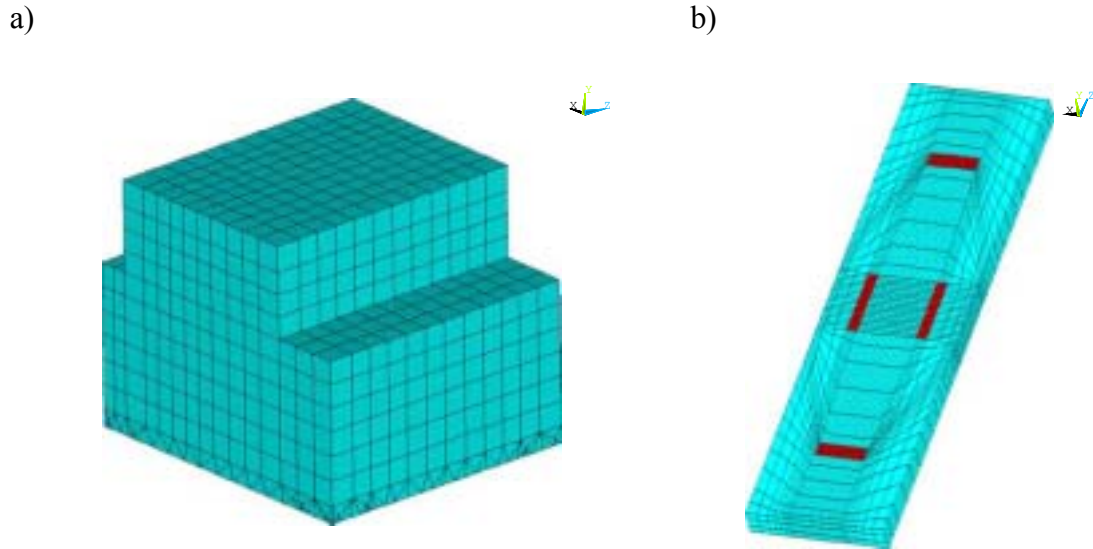
Figure 5.4   Element mesh for whole die (a) and for the membrane and resistors (b).

Figure (5.5) shows how each finite element in the piezo-resistors was treated as a single resistor. This is believed to be a novel approach for obtaining accurate piezo-resistivities in a pi-

ezo-resistors. The average x- and z-component stresses were found for each element. These
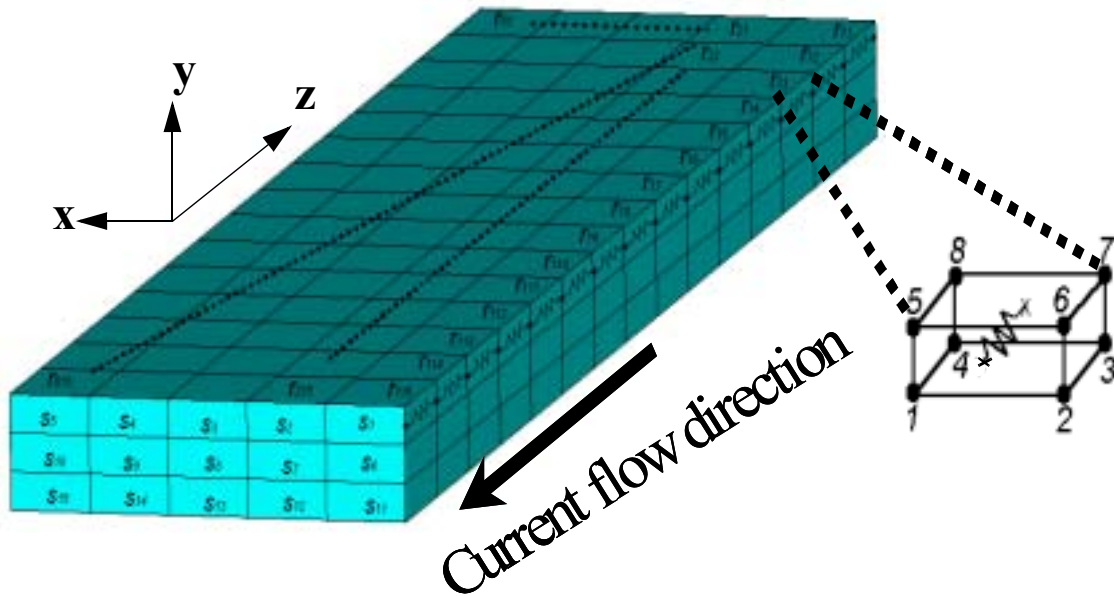
Figure 5.5   One piezo-resistor divided into 225 finite elements.

stresses were then used with Equation (5-1) to find the piezo-resistance for each element. Because the typical thickness of the piezo-resistors was in the order of a few microns, no current was expected in the y-direction. The total resistance was calculated by using a parallel and uniform current assumption as shown in Figure (5.6).
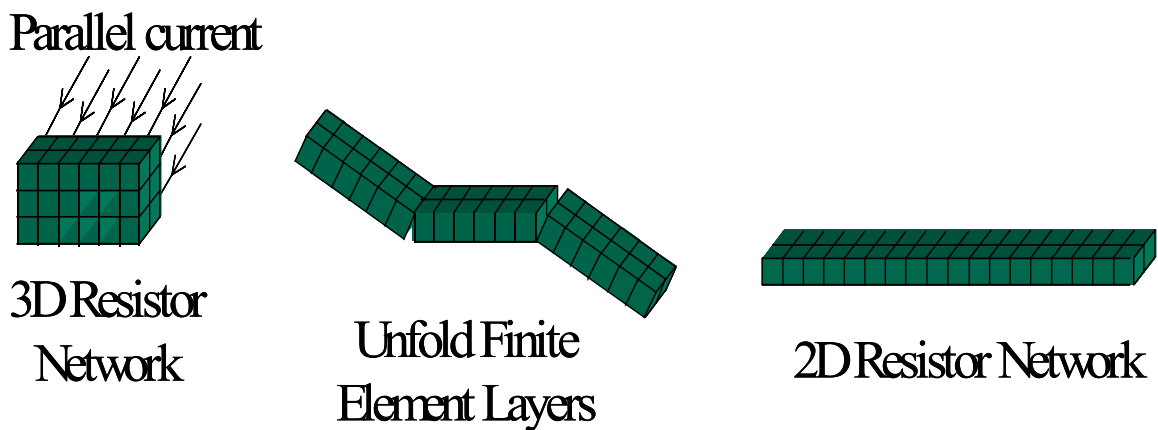
Figure 5.6   From 3D to 2D Resistor Network by parallel & uniform current assumption

The total resistance for one piezo-resistor was then found by simple resistor network summation, Figure (5.7).
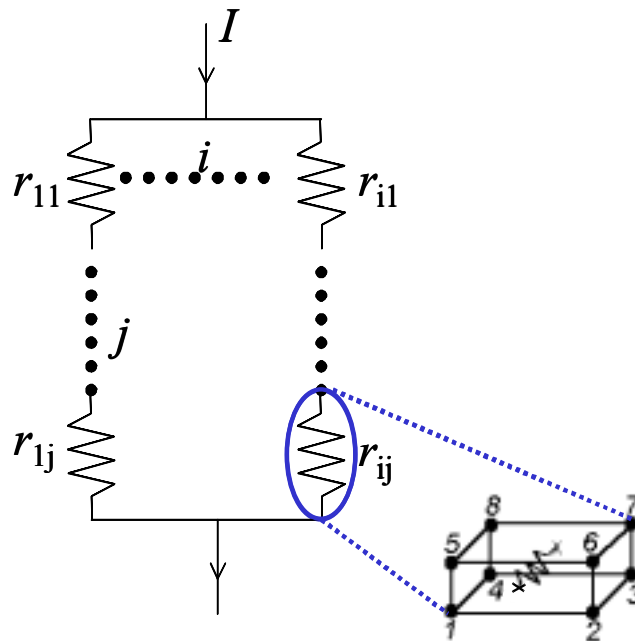
Figure 5.7   The equivalent resistor network.

5.2.4 Loads

The solution was obtained in four loadsteps, one loadstep for each temperature at which results were extracted. The pressure was applied from 0 to 3000kPa in 2 substeps, i.e. in increments of 1500kPa. Results were then available at 0, 1500 and 3000kPa for each temperature.

5.3 ELECTRICAL MODELLING

5.3.1 The Wheatstone Bridge

Figure (5.8) shows the Wheatstone bridge. First the stresses was calculated in the Si diaphragm as a function of applied pressure. Then the resistances of the piezo-resistors were calculated followed by calculations of the bridge signal (Equation (5-2)). This procedure was repeated for each pressure substep and the four temperatures.
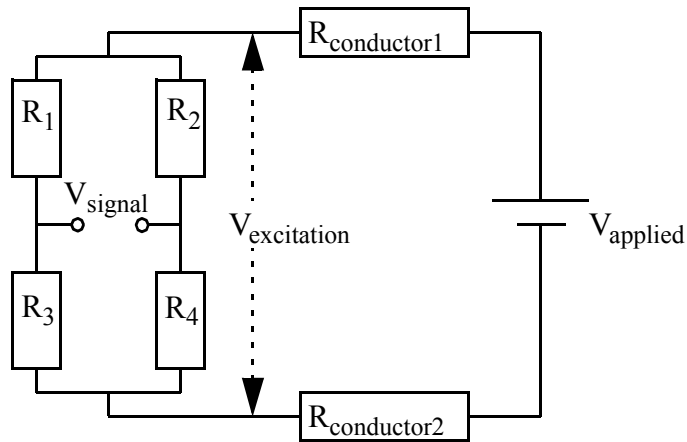
Figure 5.8   Wheatstone bridge with conductor-resistance represented.

Equation (5-2) shows that the voltage signal, V_{signal}, from a Wheatstone bridge, is proportional to the voltage across the Wheatstone bridge, $V_{excitation}$.

$$\frac{V_{signal}}{V_{excitation}} = \frac{R_1}{R_1 + R_3} - \frac{R_2}{R_2 + R_4} \qquad (5\text{-}2)$$

The voltage across the Wheatstone bridge itself is less than the voltage applied to the sensor externally, $V_{applied}$, due to voltage drop over the internal conductors, $R_{conductor1\&2}$. $V_{excitation}$ could not be measured directly in these sensors. It was however possible to estimate $V_{excitation}$ by using Equation (5-3),

$$V_{excitation} = V_{applied} \frac{R_b}{R_{conductor1} + R_b + R_{conductor2}} \qquad (5\text{-}3)$$

where R_b was the total bridge resistance and $R_{conductor1\&2}$ was a sum of contact-, buried conductor- and metal conductor-resistances (see Figure (5.9)).
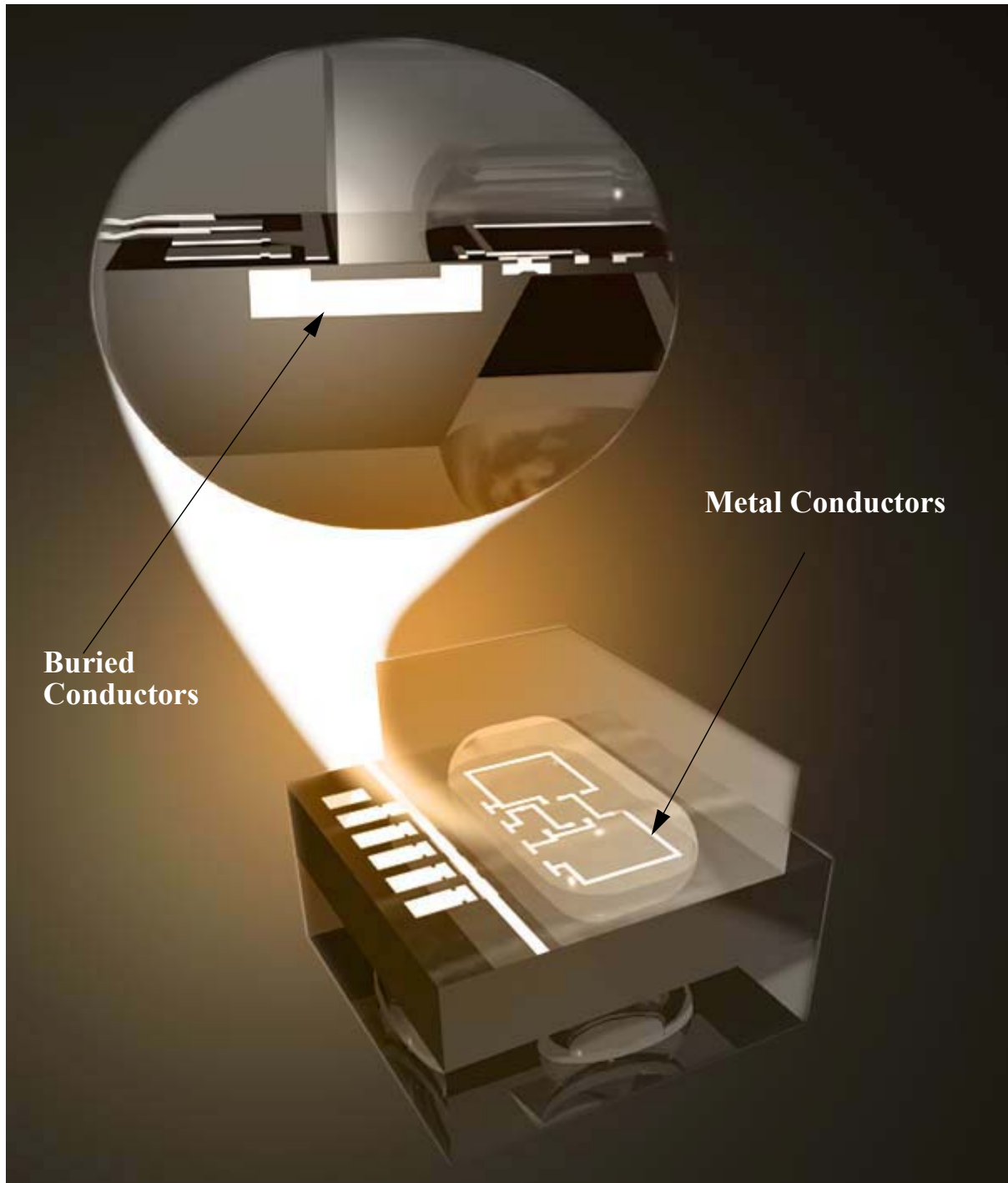
Figure 5.9   Schematic showing buried and metal conductors that partly make up $R_{conductor1\&2}$. Note: the bridge layout is different in this picture than the one used in this work.

5.4 PRESSURE SENSOR CHARACTERISATION - EXPERIMENTAL TECHNIQUE

The MEMS pressure sensor in question was encapsulated in an EMC as described in Chapter 4. This packaging process can be harsh and can contribute significantly to distortion of the trans-

ducer signal. A bare-die characterisation was necessary to isolate any packaging effects. This was carried out by assembling the sensor in a ceramic capsule as shown in Figure (5.10). In the ceramic capsule, the sensor could either be glued to the bottom surface by a soft glue or simply hung by the bonded wires. The latter method excluded all packaging effects and was used for the measurements done in this work. The ceramic capsule (without lid) was then mounted on a printed circuit board and placed in a pressure/temperature testing chamber.
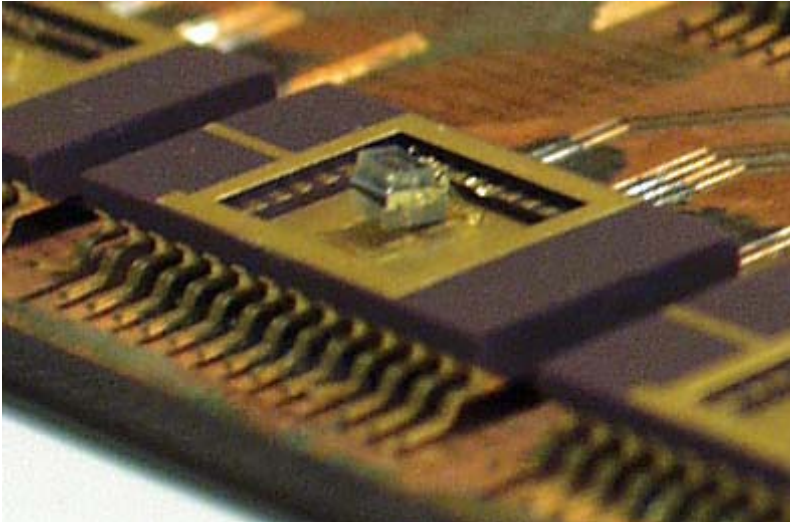
Figure 5.10   Bare Die assembled in a ceramic capsule. The sensor is hanging by the bonding wires.

5.5 RESULTS & DISCUSSION

5.5.1 FEA Results

It is worth noticing that during the testing of the sensor in the ceramic capsule, the pressure load acted not only to the pressure-hole inlet, but to all the exposed surfaces. The difference in the modelled output from the two loading conditions is summarised in Tables (5.5), (5.6) and (5.7).

The tabulated signal values has the units of mV/V because the values actually represents $V_{signal}/V_{excitation}$ as shown in Equation (5-2). It is extremely important that the reader at this point take note that all the coming tabulated values from the FEA represent $V_{signal}/V_{excitation}$. This means that the FEA results must be multiplied by the yet-to-be estimated $V_{excitation}$ when they are directly compared to the experimentally measured values. Sensitivity was defined as the slope of Signal vs. Pressure curve and was given in units of $\sigma V/V/kPa$ and also must be multiplied by $V_{excitation}$ for direct comparison.

Table 5.5: Load Cases

Case No.	Pressure Applied to:
1	Pressure inlet port
2	All exposed surfaces

66

Table 5.6: Calculated signal values for Case 1: Pressure load applied via the pressure inlet port. [*mV/V*]

Temperature (C) Pressure (kPa)	-7.5	25	75	125
0	0.41	0.57	0.65	0.62
1500	11.16	10.21	8.98	7.96
3000	21.88	19.83	17.29	15.29
Sensitivity [µV/V/kPa]	7.16	6.42	5.55	4.89

Table 5.7: Calculated signal values for Case 2. Pressure load applied on all exposed surfaces. [*mV/V*]

Temperature (C) Pressure (kPa)	-7.5	25	75	125
0	0.41	0.57	0.65	0.62
1500	9.48	8.71	7.68	6.82
3000	18.54	16.84	14.70	13.01
Sensitivity [µV/V/kPa]	6.04	5.42	4.68	4.13

Tables (5.6) and (5.7) show that an average reduction in sensitivity of 14% came as a result of the different loading conditions. This was significant and indicated that the sensor was sensitive to external load on the level-0 package. This result also proved that it was not adequate to model the membrane alone to estimate the sensor behaviour.

5.5.2 Measurement Results

The experimental data was obtained by placing the dies in a combined pressure/temperature chamber. The temperature was set to a prescribed value and the system was equilibrated for 15 minutes at each temperature. The pressure was then applied and the signal recorded. The applied voltage, $V_{applied}$, was set to 5.0Volts.

The main problem with the experimental data was that both temperature and pressure varied too much to treat any of them as constant over the time of the measurement. The way to get around this was to fit a 2-variable (Temperature and Pressure) function to the data. The fitted functions could then be used to extract measured data for constant pressure or constant temperature. It was decided to fit a function of the form;

$$S / T3P0 = a + b \lceil T + c \lceil P + d \lceil T \lceil P \tag{5-4}$$

where T was temperature in $^\circ$C, P was pressure in kPa and S-signal in mVolts. This function was linear both in T and P and thus gave the desired sensitivity at any temperature by;

$$\frac{\in S}{\in P} = c + d \lceil T \tag{5-5}$$

8 dies were measured in total. As an example, the measurements for one die is reproduced in Table (5.8) with the corresponding fitted surface in Figure (5.11). The measurement data for all 8 dies can be found in Appendix A. The regression variables for the 8 dies are listed in Table (5.9).

Table 5.8: Measured Signal for Die 1

Temperature ($^\circ$C)	Pressure (kPa)	Signal (mV)
117.2	70	5.878
99.8	70	6.499
75.7	70	7.292
25.5	70.1	8.781
-8.4	70.2	9.651
97.7	99.9	7.197
74.3	99.9	7.999
117.5	100	6.511
104.9	100	6.944
64.5	100	8.306
25.5	100	9.496
-7.9	100	10.387
84.6	100.1	7.641
22.6	100.2	9.519
-9.9	183.5	12.616
-6.8	999.9	33.098
116	1000	25.054

Table 5.8: Measured Signal for Die 1

72.7	1000	27.882
26	1000	30.927
95.1	1000.1	26.424
26	1999.9	54.432
-6.7	1999.9	58.006
92.8	2000	47.648
113.6	2000.1	45.594
71.2	2000.1	49.794
111.3	3000	66.024
90.7	3000	68.737
-6.6	3000	82.535
69.8	3000.1	71.489
26	3000.2	77.581
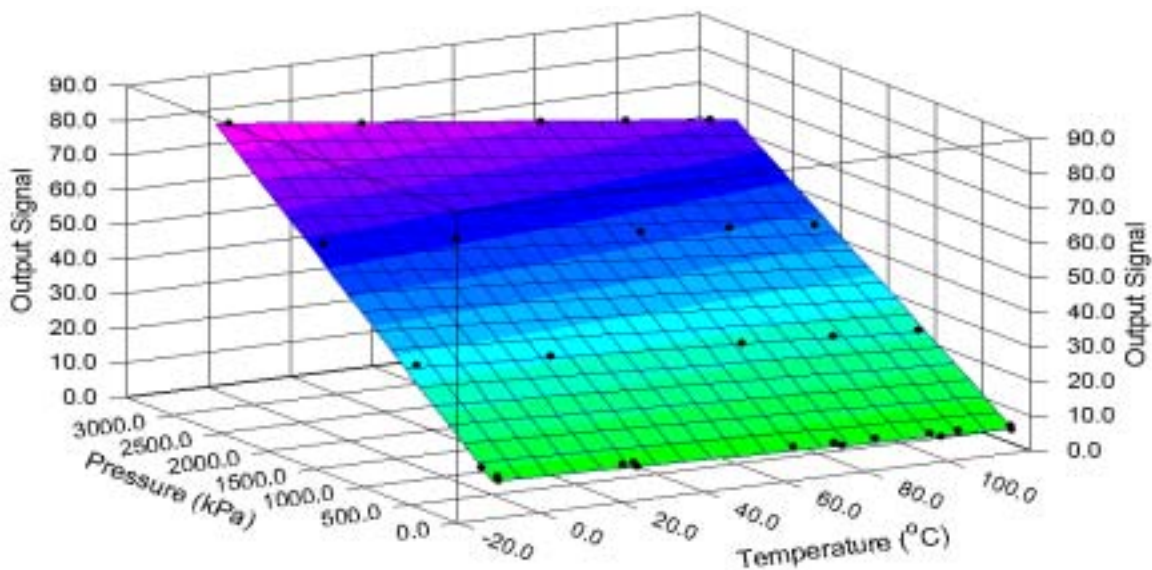
Figure 5.11   Plot of the fitted equation to the datapoints.

Table 5.9: Regression Variable Values for all 8 dies

	Regression Variable Values				
Die No.	a	b	c	d	R^2
1	7.84	-0.02738	0.02458	-3.76E-05	0.999959

69

Table 5.9: Regression Variable Values for all 8 dies

2	-7.95	-0.01119	0.02502	-3.86E-05	0.999955
3	-0.73696	-0.02407	0.02506	-3.84E-05	0.999956
4	-7.10908	-0.05271	0.02586	-4.12E-05	0.999787
5	-2.63307	-0.02593	0.02346	-3.56E-05	0.999959
6	5.59222	-0.02453	0.02556	-3.89E-05	0.999953
7	9.71099	-0.02249	0.02461	-3.78E-05	0.999959
8	4.19281	-0.03916	0.02577	-3.92E-05	0.999950

The R^2 values show that, for each die, more than 99.99% of the total sum of squares was explained by the model. This indicated good correlation between the fitted function and the datapoints.

As mentioned before, the FEA model did not include the conductor resistances. This meant that a direct comparison of the FEA calculated results and the measured results could only be done when the voltage across the bridge, $V_{excitation}$, was known. $V_{excitation}$ could not be measured directly on the sensor dies because the bridge was inside the glass cavity. A rough estimation of $V_{excitation}$ was obtained using Equation (5-3). For the product in question $R_{conductor1\&2}$ had been estimated to be 100T and R_b was measured to be 2300T, at room temperature. The equation then gave:

$$V_{excitation} = 5V \frac{2300T}{2 \left(100 \partial 50T 0 + 2300T \right)} = 4.2 \partial 0.4 Volts \tag{5-6}$$

The FEA calculated bridge response at 25$^\upsilon$C was multiplied by the estimated $V_{excitation}$. The calculated result and the measured result was shown in Table (5.10). This comparison was only done at 25°C because no measurements for $R_{conductor1\&2}$ was done on the wafers for other temperatures. The close match that was obtained gave confidence that the model was correct.

Table 5.10: Comparison of FEA result to measured data (σV/kPa).

FEA $\Delta V_{excitation}$	Average sensitivity for measured data
22.77±2.20	24.03

With the model validated for 25°C, an estimated $V_{excitation}$ for all temperatures was found by dividing the measured sensitivities by the estimated sensitivities. This was done to calibrate the model so that it could later be used to look at the level-1 packaging stress problem. Figure (5.12) shows the estimated $V_{excitation}$ as a function of temperature. The average value, with error bars representing 1 standard deviation, is also plotted on the same plot. Table (5.11) lists the average values with the 95% confidence intervals.

Die 5 laid outside 1 standard deviation. This was probably the result of wafer-to-wafer variations in the manufacturing process.
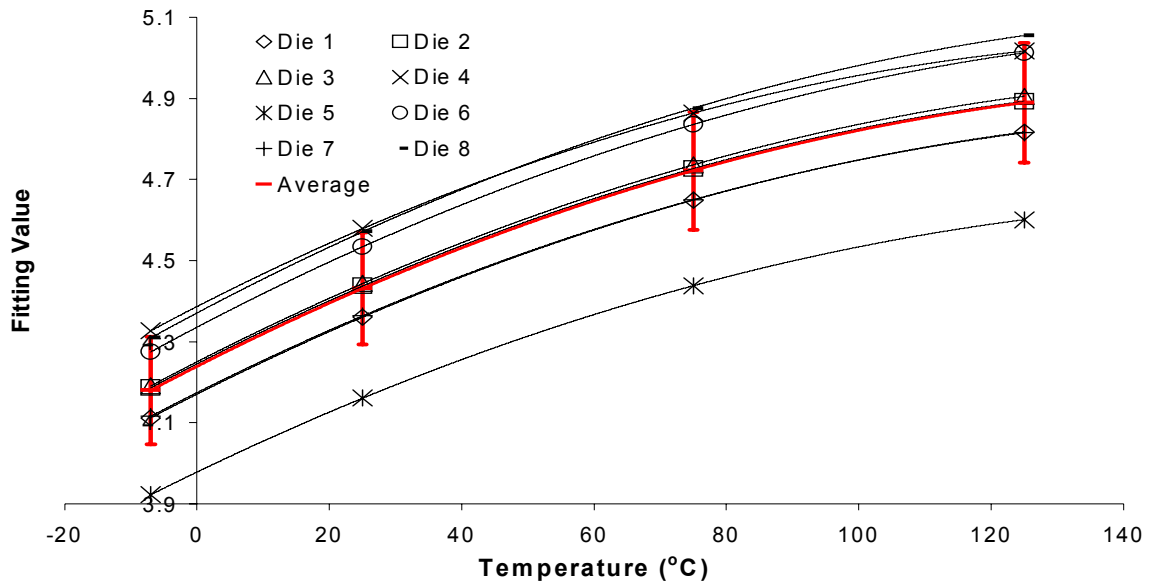
Figure 5.12   Plot of theoretically estimated $V_{excitation}$ vs. Temperature.

Table 5.11: Fitted values of $V_{excitation}$ for different temperatures.

Temperature ($^\upsilon$C)	$V_{excitation}$ (V)	95% Confidence Interval
-7	4.1	0.1
25	4.4	0.1
75	4.7	0.1
125	4.8	0.1

   Figure (5.12) shows that the trend of the curves were the same. The only difference was a shift on the vertical axis which probably was a result of process variation during manufacturing. This observation indicated that all the effects that contributed to the output signal of the sensor had been included in the FE model. Table (5.11) also show that the estimated value for $V_{excitation}$, $4.4 \partial 0.1V$, coincided with $4.2 \partial 0.4V$ that was calculated from Equation (5-6).

5.5.3 Process Variations

It was important to understand how mask missalignment and process variations could alter the sensor signal. A set of simulations were run to map out these effects. Table (5.12) gives an overview of the different cases that were considered. Figure (5.13) shows the sensitivity at 25°C for each of the process variation cases. The full result tables can be found in Appendix B.

71

Table 5.12: Load Cases for Process Variation Study

Case No.	Process Variable Varied
1	Resistors Shifted in x-direction
2	Resistors Shifted in z-direction
3	Resistors Rotated with respect to the membrane
4	Top Glass Cavity rotated
5	Membrane rotated
6	Longer Resistors
7	Wider Resistors
8	All the above
9	Max membrane dimensions, min thickness
10	Min membrane dimensions, max thickness
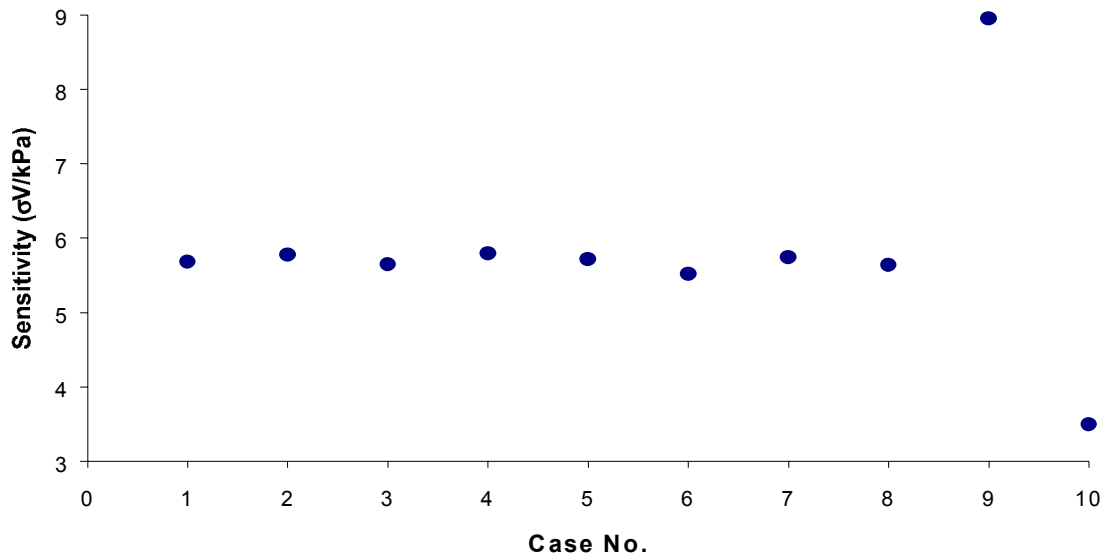
Figure 5.13   Sensitivity at 25°C for the 10 process variations in Table (5.12)

Cases 1 through 8 yielded little or no deviation to the sensitivity. The only major contributing effects was found to be alterations of the membrane dimensions. This concluded that process variations due to mask missalignment of the resistors did not contribute significantly to sensitivity deviations when compared to membrane-dimension variation.

5.5.4 CTE mismatch

The level-0 package consisted of a glass-silicon-glass stack, anodically bonded together at typically 350-400°C. The glass used was a borosilicate glass, Corning 7740. Figure (5.14) shows a plot of CTE of the two materials.
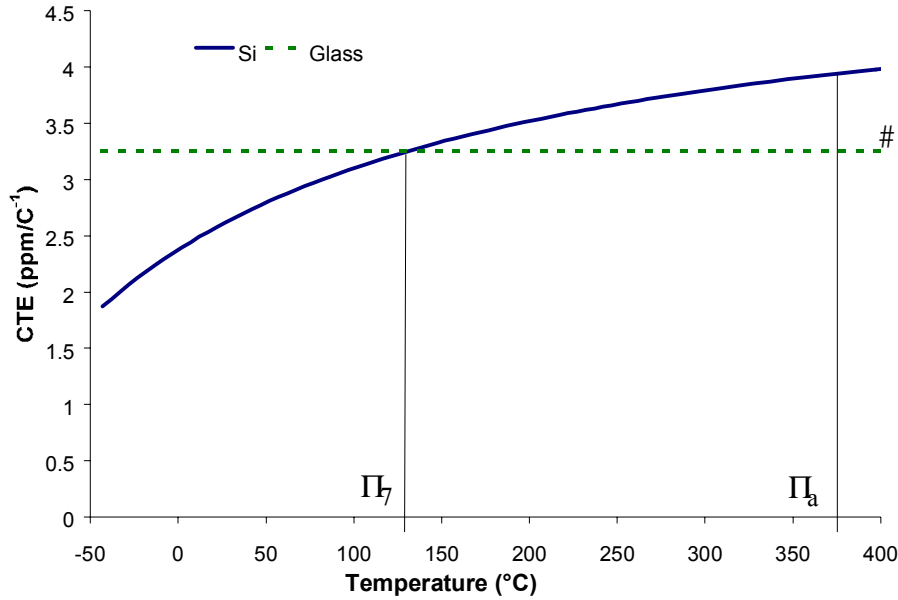
Figure 5.14   Coefficient of Thermal Expansion plot of Glass and Silicon

Figure (5.14) shows that CTE of Si was higher than that of borosilicate glass at the anodic bonding temperature (T_a). They had matching CTE's at around 125°C (T_0). Descending from T_0, Si had a lower CTE. Because the level-0 package was assembled at T_a, this temperature was assumed to represent the stress-free condition of the structure from which all thermal strains (κ_{th}) are calculated.

The CTE mismatch caused thermally driven stresses to occur. It was important to understand what effect this stress had on the membrane and hence the signal. Table (5.13) shows the signal for the sensor when the glass was exchanged for silicon, and hence no CTE mismatch or thermally driven stresses occurred. As expected, there was no signal at zero pressure because any signal at zero pressure was a result of level-0 packaging stress. Since the whole package was silicon, no CTE mismatch occurred and hence no stress would result from thermal loads. The sensitivities were all 1% higher than in the glass-Si-glass package. The concluding remark from this was that the level-0 package did indeed affect the sensor signal and should be considered for accurate sensor simulations.

There are multiple reasons for not making the level-0 package in pure silicon, including cost and post-manufacturing inspection issues.

Table 5.13: Calculated signal values for a pure Si sensor [*mV/V*]

Pressure (kPa) *Temperature (C)*	-7.5	25	75	125
0	0.00	0.00	0.00	0.00
1500	10.35	8.36	7.22	6.38
3000	20.71	16.79	14.42	12.75
Sensitivity [µV/V/kPa]	6.89	5.63	4.81	4.25

5.5.5 Offset

The offset is the voltage signal at zero pressure. There are several cases that contribute to non-zero offset voltage. The diaphragm can be stressed by the thermal mismatch in the level-0 package or from residual stresses in the silicon. Impurities in silicon can set up localised residual stresses that could cause the membrane to deflect. This can give relatively large offset signals. These residual stresses were not included in this work. Only offset caused by level-0 packaging effects were included in these simulations.

Yet another source of offset was variation in the piezo-resistor resistance due to production inconsistency. This can cause the four resistors in the Wheatstone bridge to have slightly different resistances at zero pressure, which in turn could cause signal offset.

The offset in the measurements could be found by setting *P=0kPa* in Equation (5-4), which yielded $S/03T0 = a + b \; [T$. It was then found that the offset ranged from -8.6mV to +9.1mV at room temperature. This was obviously more than the level-0 package contribution which was simulated to be 0.57mV.

The way to get around the effect of the offset was to look at sensitivity. This was done because the sensitivity (slope, or the derivative of the Signal vs. Pressure curve) was per definition independent of a constant offset.

Two ways to compare simulated results to the measured results were to plot sensitivity as a function of temperature, and signal as a function of temperature. Since the sensitivity was used to obtain $V_{excitation}$ it was unsuitable for comparison, because it would yield a 1-to-1 relation.

Figure (5.15) shows signal vs. temperature plots for the FEA and measured signals at 1500kPa and 3000kPa. The match was indeed good. The errorbars represented 1 standard deviation of the measured dataset.
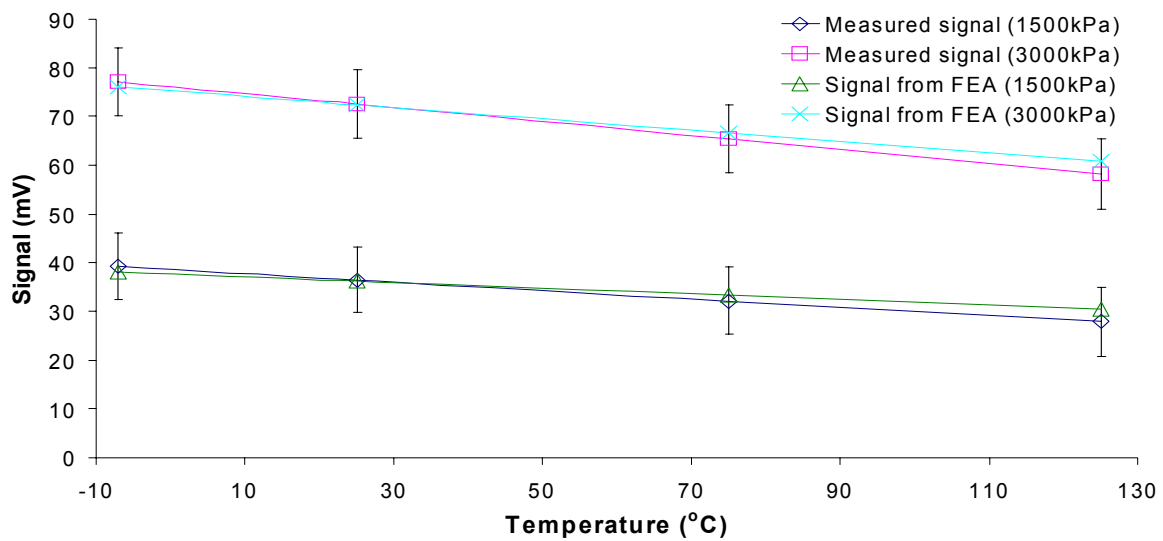
 Figure 5.15   Signal vs. temperature from the FEA and measured signal levels at 1500kPa and 3000kPa.

5.6 CONCLUSIONS

This chapter started by developing a parametric FE model of a commercial piezo-resistive MEMS pressure sensor. A novel method of treating each element as a resistor was developed in order to accurately track the piezo-resistivity over an area with high stress gradients. This work was believed to be the first work to include level-0 packaging effects on a sensor signal over it's intended service temperature range. The results of the analysis compared well to measured data.

   The simulations showed that the effect of the level-0 package was not negligible. It also showed that the sensor die was sensitive to the loading situation. A large difference was found between applying pressure only to the pressure inlet port and applying it to the whole structure. Process variations regarding resistor shifts and rotation plus top-glass cavity shifts and rotation had negligible effect on the sensor signal. Process variations regarding membrane dimensions had a large influence on the sensor signal.

CHAPTER 6

PACKAGING STRESS WITH AN ELASTIC MATERIAL MODEL

This chapter utilizes the previously developed method to investigate the effect of the stress contributed by the Epoxy Moulding Compound (EMC). An elastic material approach is taken as a first step towards understanding the packaging effect. Other researchers [68], [55], [69] have also investigated the result of packaging stress in plastic devices. However, to the authors knowledge, none have studied the effect on the characteristics of the MEMS device behaviour as a result of the packaging stress. The work in this chapter has been published at the EuroSIME2003 conference [89] and has been submitted to Elsevier's Micro-electronics Reliability Journal.

6.1 INTRODUCTION

A bare MEMS transducer is easily damaged. Even careful handling can be critical to its reliability. The previous chapter showed how a level-0 package often is used to protect the transducer element from any external contaminant and direct contact. This packaging is preferably done on wafer level to avoid extra process steps and contamination during and after dicing. A MEMS device generally needs something to read and process its output for further usage. The signal is then transmitted to the outside world. It is convenient to supply both chips in one package. This is accomplished by moulding both the sensor die and ASIC in a single plastic capsule as shown in Figure (6.1).
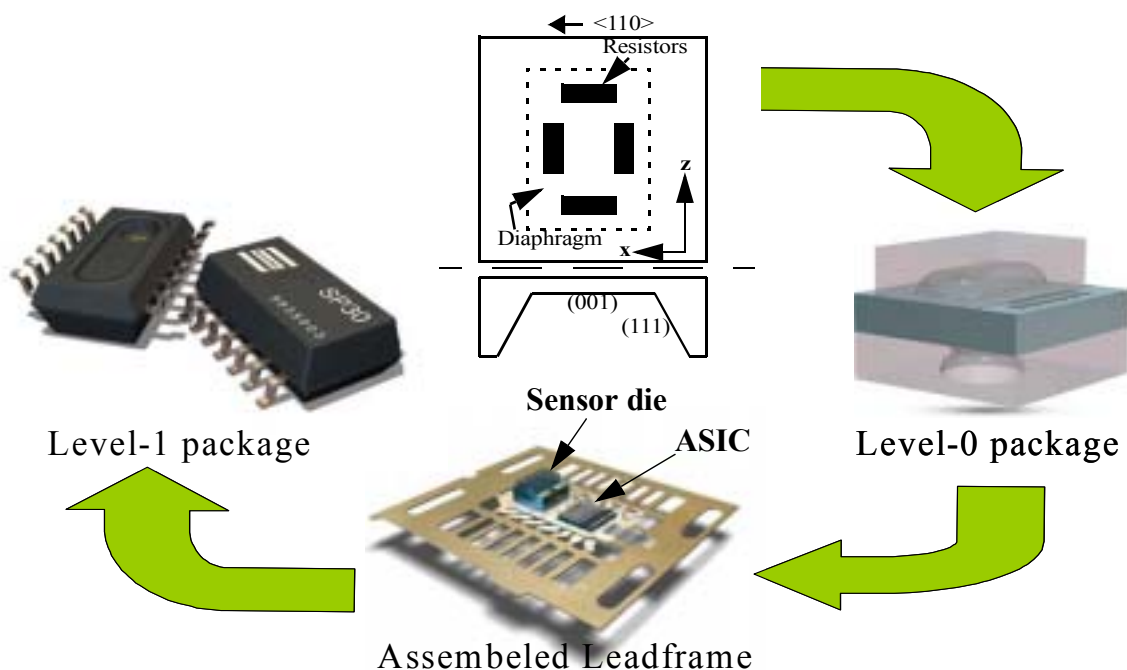
Figure 6.1   Steps in the production cycle of a MEMS pressure sensor.

Figure (6.1) gives a condensed overview of the steps between the sensor die manufacturing and the final product.

The leadframe is the backbone in a moulded plastic package. It is fabricated from a strip of sheet metal by stamping or chemical etching. The metal can be pure copper or often a copper alloy, selected to obtain desired properties [22]. At first it serves as a holding fixture during the assembly process shown in Figure (6.2) (b)-(f). After moulding it becomes an integrated part of the whole package and is used for electrical contact, heat conduction and to give structural stiffness.

The Back-End process line work as follows. A bare leadframe is picked up by a robot (a). The

a)   b)   c)

d)   e)   f)

g)   h)
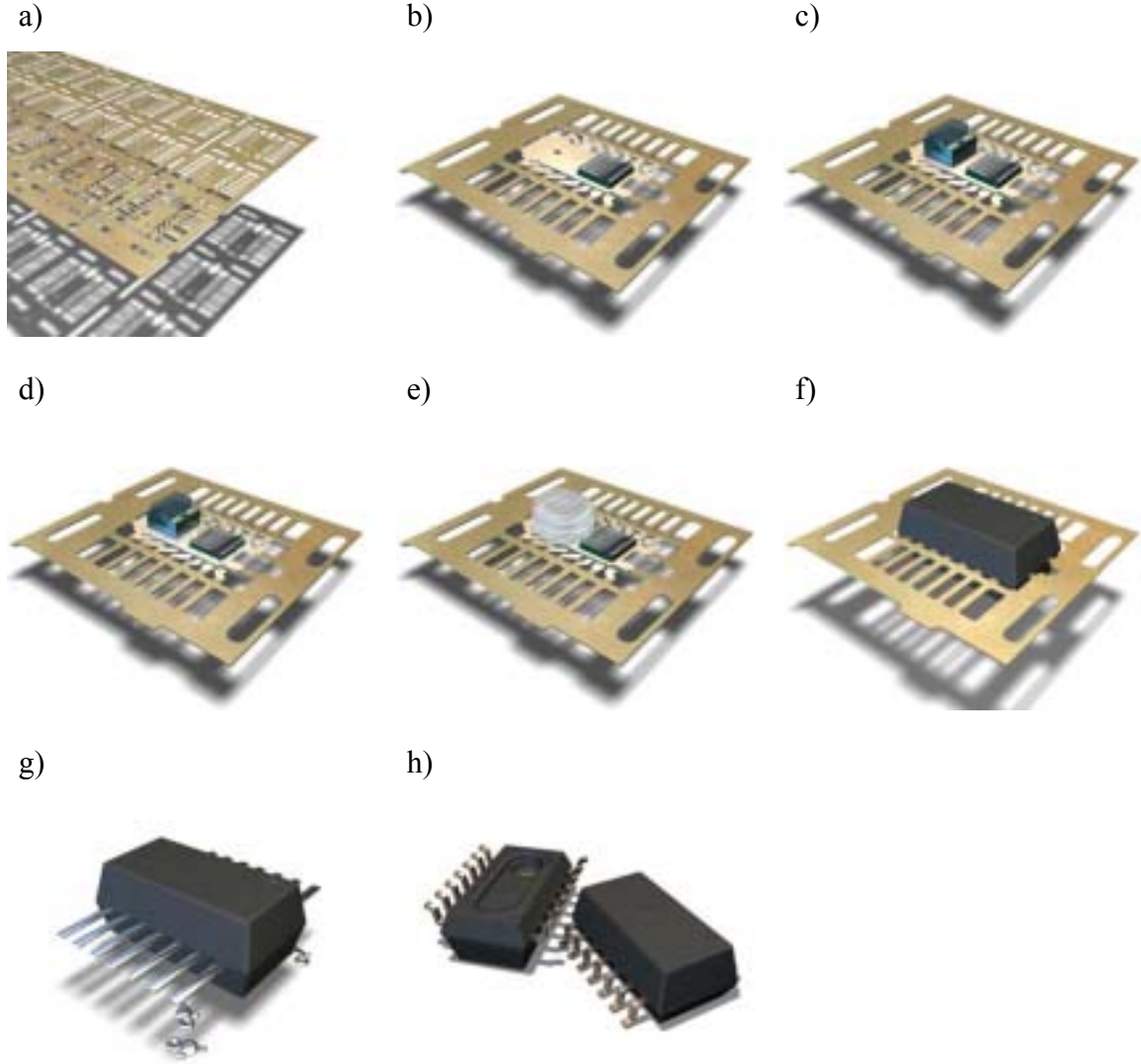
Figure 6.2   Process flow in Back-End. Leadframe is feed into the assembly line, a). ASIC and Sensor die is placed on leadframe, b) & c), followed by die-attach curing, d). Next comes wire bonding and globe-top, e) & f), before the assembled pieces are moulded, g). A trim & form follows (h).

leadframe is transported to the ASIC mounting station where the die attach is dispensed, the ASIC placed and cured (b). Sensor mounting (c) comes next followed by curing die attach. The leadframe is then moved to wire bonding (d). Then comes Glob Topping (GT) of the sensor die (e) and GT curing. The assembled leadframe is then encapsulated with EMC in a transfer moulding process (f) before it is sent to plating (g) and trim&form (h).

6.2 MATERIAL PROPERTIES

6.2.1 Epoxy Moulding Compound

Young's Modulus was obtained by DMA. The data was reported in Chapter 3. Table (6.1) shows the Young's Modulus and mean values of CTE that were used in the simulations. The mean CTE values were obtained by assuming a reference temperature equivalent to the stress free condition at 175°C, equal to the moulding temperature. The material data were temperature dependent. Note that the data was obtained from fully cured EMC samples.

Table 6.1: Temperature dependent material properties of the EMC

Temperature (^oC)	Young's Modulus	Mean CTE (ppm/^oC)
-7	18700MPa	13.7
25	18100MPa	14.9
75	17900MPa	18.4
125	14200MPa	28.7

6.2.2 Silver Filled Epoxy Glue

The viscoelasticity of the glue was neglected because it was assumed not to be relevant due to its low stiffness above it's glass transition temperature, T_g. The modulus of the glue was 2-3 orders of magnitude lower than any of its surrounding materials. The validity of assuming a constant modulus was considered valid because all the analysis were done above its T_g.

Material data for the QMI505^{TM} glue was provided by Loctite and are shown in Table (6.2) below.

Table 6.2: Material Property for QMI505

Mechanical Property	Value
T_g	-30^oC
E-modulus	740MPa
CTE	166 ppm/^oC

6.2.3 Cu leadframe

The leadframe was made of pure copper and the material data that are shown in Table (6.3) below were taken from [22].

Table 6.3: Material Property for Copper leadframe

Mechanical Property	Value
E-modulus	123000MPa
CTE	16 ppm/^{o}C

6.3 THERMOMECHANICAL MODELLING

6.3.1 The Geometry

The FEA model was built, meshed and solved using the finite element code ANSYS^{TM} v6.1. The model consisted of 5 different materials; silicon, glass, glue, copper and EMC. Figures (6.3), (6.4) and (6.5) shows the geometry of the packaged sensor. The geometry was parameterized to allow for flexibility towards different package designs. Figure (6.4) shows the pressure inlet hole in the bottom-side of the package.
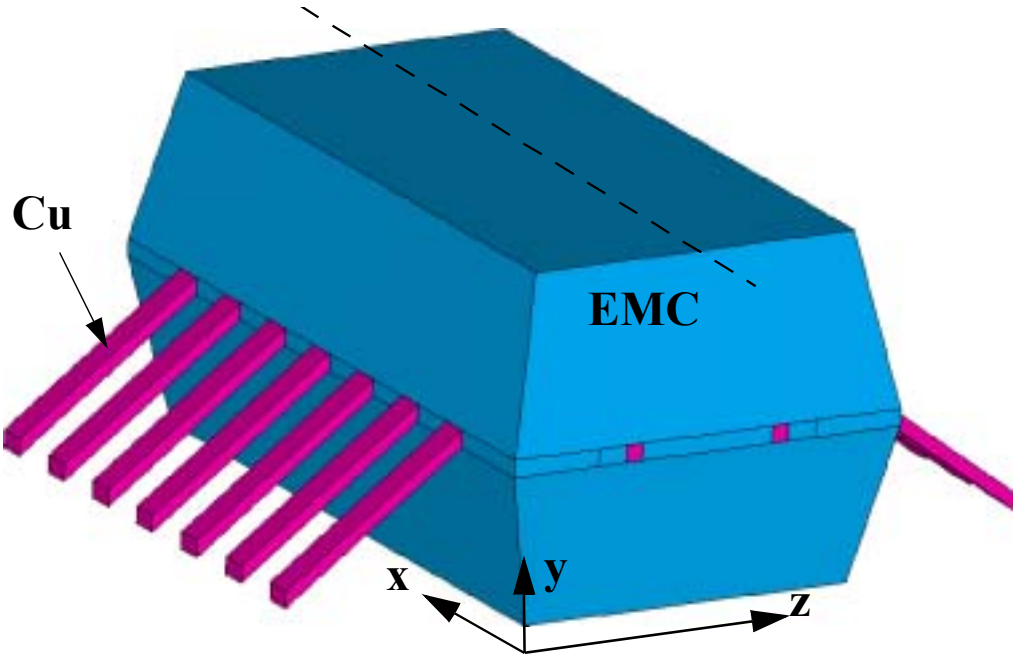
Figure 6.3   Geometry model showing the top side of the package
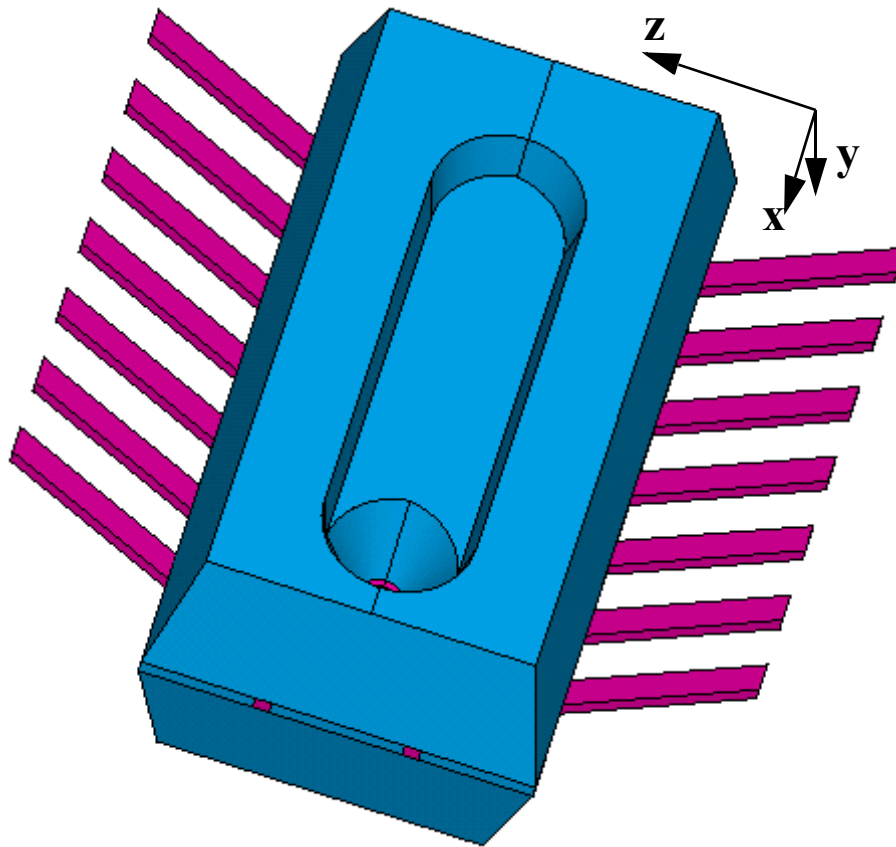
Figure 6.4   Geometry model showing the bottom side of the package

A full model was built in spite of the symmetry along the longitudinal length of the package (dotted line). This decision was made to render the possibility to look at the effects of manufacturing inconsistencies. The process variations can result in a geometry deviating from exact symmetry. The trade-off by considering a full model was longer computational time. Still the model could be solved over night on a P4 1.4GHz PC.

Figure (6.5) shows the geometrical structure inside the EMC. Both the sensor and the ASIC was glued onto the leadframe. The glue was modelled by a thin volume between the components and the leadframe.
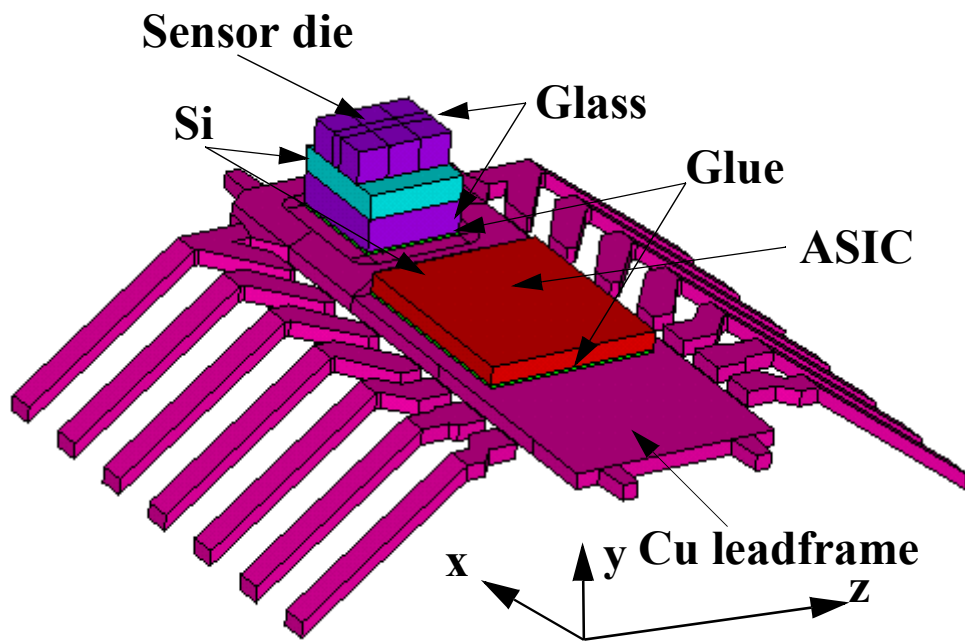
Figure 6.5   Geometry model showing the interior of the package

6.3.2 The Mesh

The model was meshed with 58450 elements resulting in 114861 nodes. 12769 of the elements were 20 node bricks and 45681 were 12 node tetrahedral elements, SOLID186 and SOLID187 respectively. Figures (6.6) and (6.7) shows the mesh of the exterior and interior of
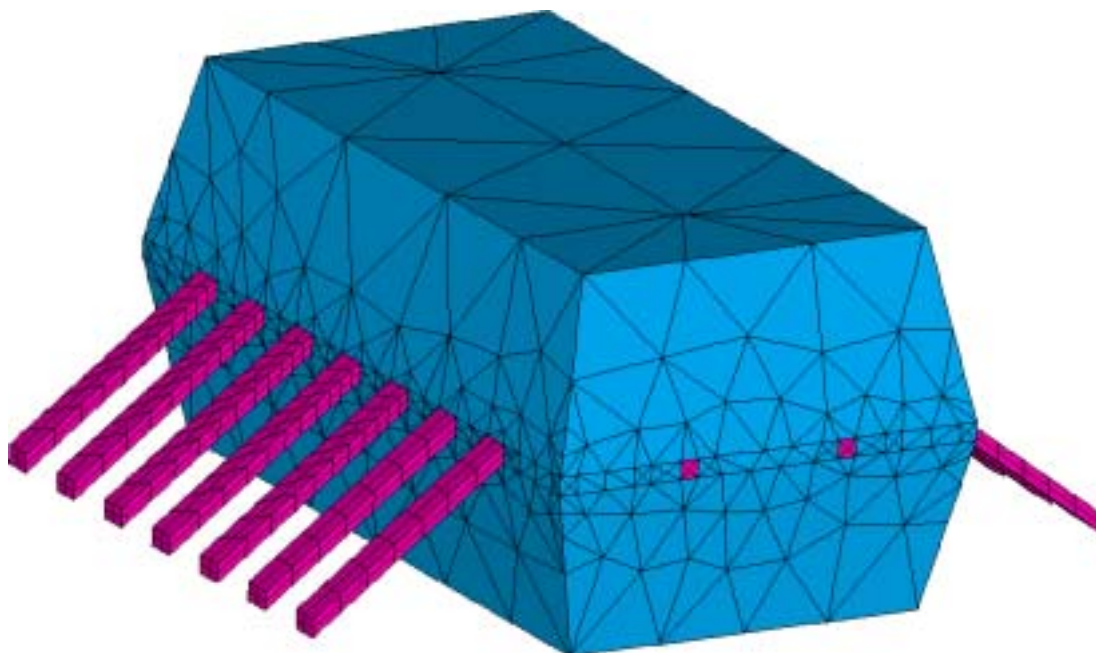
Figure 6.6   Mesh of the exterior of the package.
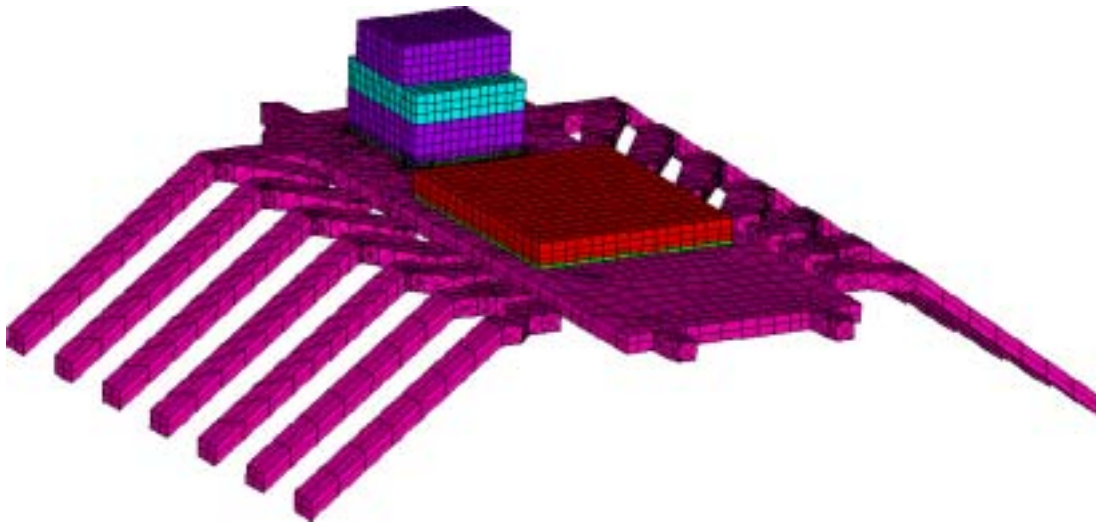
Figure 6.7   Mesh of the interior of the package.
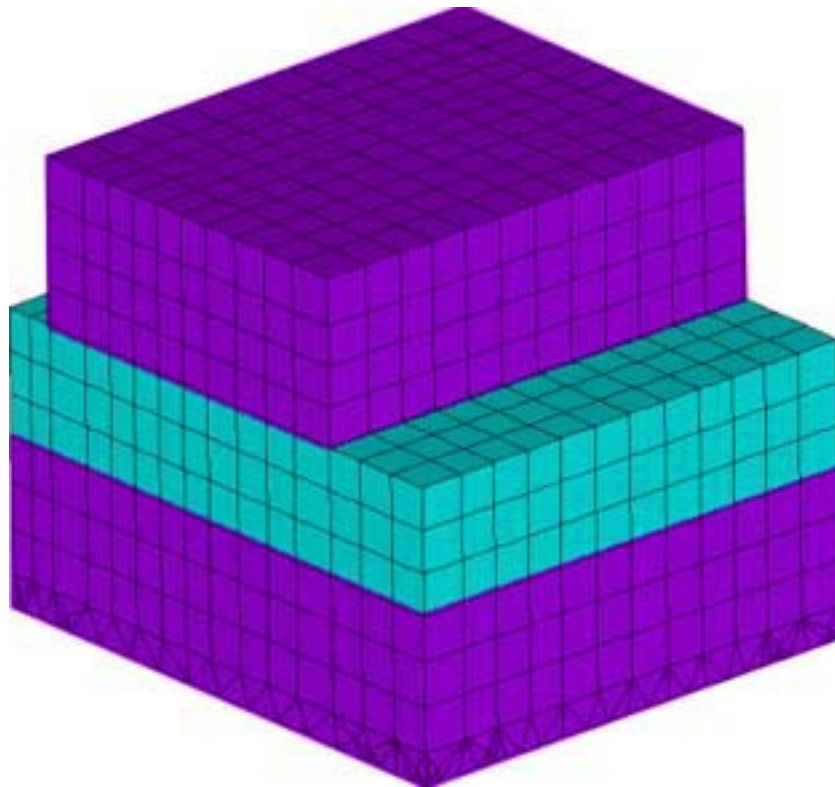
Figure 6.8   Mesh of the sensor die.

the sensor package respectively. Special care was taken to hexahedral mesh regions of interest. One such region in particular, was the exterior of the sensor die. This was done to obtain accurate and detailed information on the stress exherted by the EMC onto the sensor die. An even brick mesh was created to trap the packaging stress gradients on exposed surfaces to a satisfactory level. Figure (6.8) shows the mesh on the sensor die. A transition region of tetrahedral el-

ements in the bottom was needed to transition from the small elements in the glue to the bigger map-meshed elements in the sensor die. The glue volume was meshed with small elements to sustain an acceptable aspect ratio of the elements.

6.3.3 Loads and Boundary Conditions (BC)

The loads applied on the model were in the form of isotropic pressure and uniform temperatures. The moulding temperature of 175°C was used as the stress free temperature for the EMC, ASIC, leadframe and glue. The stress free temperature of the sensor level-0 package was given as the anodic bonding temperature, as defined in Chapter 5. The respective thermal strains were calculated from these reference temperatures.

The legs of the chips were clamped between the printed circuit board and a holding fixture during lab measurements. To correctly account for this situation in the FEA, all the copper (Cu) legs were fixed in the x-, y- and z-direction.

A pressure was applied to all exposed surfaces of the package, including the pressure sensing diaphragm. Solutions were obtained for 4 different temperatures. The temperatures corresponded to those used during the laboratory measurements (-7, 25, 75 and 125°C). At each temperature the pressure was applied in two substeps, resulting in solutions for 0, 1500 and 3000kPa. A total of 12 loadsteps were solved for each run.

6.4 RESULTS & DISCUSSION

The simulations were designed to give an answer to two questions. One was to understand how the packaging stress effected the sensor performance. The second was to identify how these stresses acted on the die.
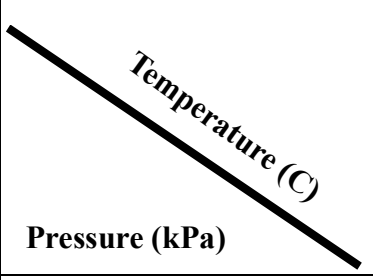
The method developed for extracting an electrical signal from a FEM model, explained in Chapter 5, was used to understand how the packaging stress effected the output signal, i.e. signal level and sensitivity. An indirect indication on the accuracy of the model was gained by comparing the estimated output signal from the FEA to measured output signals. Table (6.4) below shows the calculated signal values obtained.

Table 6.4: Calculated signal from FEA [mV/V]

Pressure (kPa) / Temperature (C)	-7.5	25	75	125
0	-50.43	-35.89	-19.59	-6.65
1500	-42.68	-29.00	-13.69	-1.59
3000	-34.93	-22.11	-7.80	3.46
Sensitivity [μV/V/kPa]	5.17	4.59	3.93	3.37

Consider the first row in Table (6.4) (for pressure = 0 kPa), which is also known as offset. One of the conclusions from Chapter 5 was that the level-0 package did not contribute much to the offset. The offset from the bare die measurements in Chapter 5 are reprinted in Table (6.5).

Table 6.5: Calculated offset signal values for bare die [mV/V]

Pressure (kPa) / Temperature (C)	-7.5	25	75	125
0	0.39	0.54	0.62	0.59

It was observed from Table (6.4) and Table (6.5) that the packaged die showed an increase in offset with decreasing temperature. This showed that the level-1 package had a profound effect on the offset. The explanation for this was found by considering the packaging process.

The stress free condition for the EMC was assumed to be at the moulding temperature, 175°C. Residual stresses from curing shrinkage and pack/hold pressure from the transfer moulding machine were neglected. This could be justified since the glass transition temperature was found to be around 130°C. With a T_g of 130°C, it meant that the EMC was in the rubbery state in the cooldown between 175 and close to 130°C (T_g). This meant that the E-modulus was low in that temperature range, which again limited the amount of stress that developed. Ochi et al. [63] showed that epoxies cured above their glass transition temperature did not build up any residual stress during curing. Only after cooled down below their glass transition temperature did stresses occur. This assumption was also used by [82].

Stresses that develop due to a packaging process are mostly a result of CTE-mismatch between the materials in the package. Thermal strain for a given material is calculated from the following formula:

$$\kappa^{th} = \int_{T_i}^{T_f} \zeta / T0 dT \qquad (6\text{-}1)$$

where ζ is the thermal expansion coefficient, T_i is the initial temperature and T_f is the final temperature. In other words, the lower the temperature, the larger the $\div T$, and hence the larger the thermal strains due to CTE mismatch would become. Ideally, all materials should have the same CTE values.

Moisture effects were neglected. The EMC in question absorbs 0.17%wt moisture after a 168h soak in 85°C/85%RH. The component used in this work were newly baked and therefore containing insignificant amounts of moisture.

The experimental data obtained for the packaged devices experienced the same problems as those obtained for the bare dies in Chapter 5. Neither pressure or temperature were kept sufficiently constant during measurements to be regarded as constants. The measurements were also

here fitted to a function. Equation (6-2) was fitted to the data. The measurement were nonlinear with respect to temperature and linear with respect to pressure.

$$S/T3P0 = a + b\,T + c\,P + d\,T\,P + e\,T^2 + f\,T^3 \tag{6-2}$$

Tables (6.6) and (6.7) show the regression variable values for the 8 chips. The measured data can be found in Appendix C.

Table 6.6: Regression Variable Values for Chips 1-4.

	Chip 1	Chip 2	Chip 3	Chip 4
a	-1.41E+02	-1.20E+02	-1.44E+02	-1.64E+02
b	1.62E+00	1.19E+00	1.10E+00	1.34E+00
c	2.52E-02	2.45E-02	2.50E-02	2.45E-02
d	-6.00E-05	-5.88E-05	-5.60E-05	-5.74E-05
e	-8.66E-03	-7.74E-03	-7.99E-03	-7.48E-03
f	4.10E-05	5.21E-05	5.58E-05	4.67E-05
R^2	0.99958	0.99945	0.99936	0.99943

.

Table 6.7: Regression Variable Values for Chips 5-8.

	Chip 5	Chip 6	Chip 7	Chip 8
a	-1.23E+02	-1.58E+02	-1.35E+02	-1.66E+02
b	1.50E+00	1.77E+00	1.57E+00	1.97E+00
c	2.47E-02	2.45E-02	2.63E-02	2.63E-02
d	-6.03E-05	-6.06E-05	-6.15E-05	-6.63E-05
e	-8.27E-03	-8.04E-03	-7.34E-03	-6.98E-03
f	4.22E-05	4.02E-05	3.44E-05	2.75E-05
R^2	0.99971	0.99979	0.99974	0.99984

Figure (6.9) shows the sensitivity vs temperature for the calculated and measured data. The comparison of the trend was good, but the values differ. The error bars represent 3 standard deviations for the measured dataset. Only one of the datapoints from the FEA was within the error bars of the measured data.
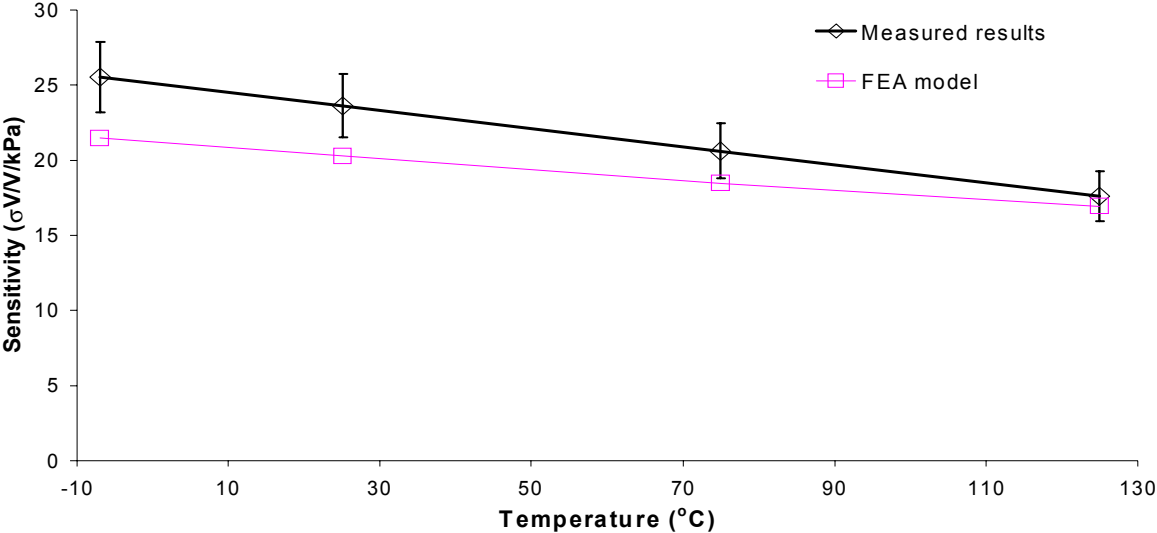
Figure 6.9   Sensitivity vs. Temperature. Error bars represent 3 st. dev.

Figure (6.10) and (6.11) shows the calculated and the measured output signal as a function of temperature. Two of the service temperatures produced signal values within 3 standard deviations of the measured data. A perfect match of the signal values was not expected due to lack of offset modelling. It was, however, expected that the trend of the curve would fit, since it was found in Chapter 5 that the offset contributed by the non-packaging related effects were independent of temperature. Both figures show that the trend was reasonably well matched, and hence that the model was successful in predicting the behaviour of the packaged sensor. Explanations for the observed deviations were found by considering the different assumptions that had been made in these analyses. Firstly, the modelling did not include process steps previous to the moulding. An improvement of the model would be to include all the steps of the assembly line. Wang et al. [69] found that a FEM model could yield 50% higher stresses when all these steps were included.
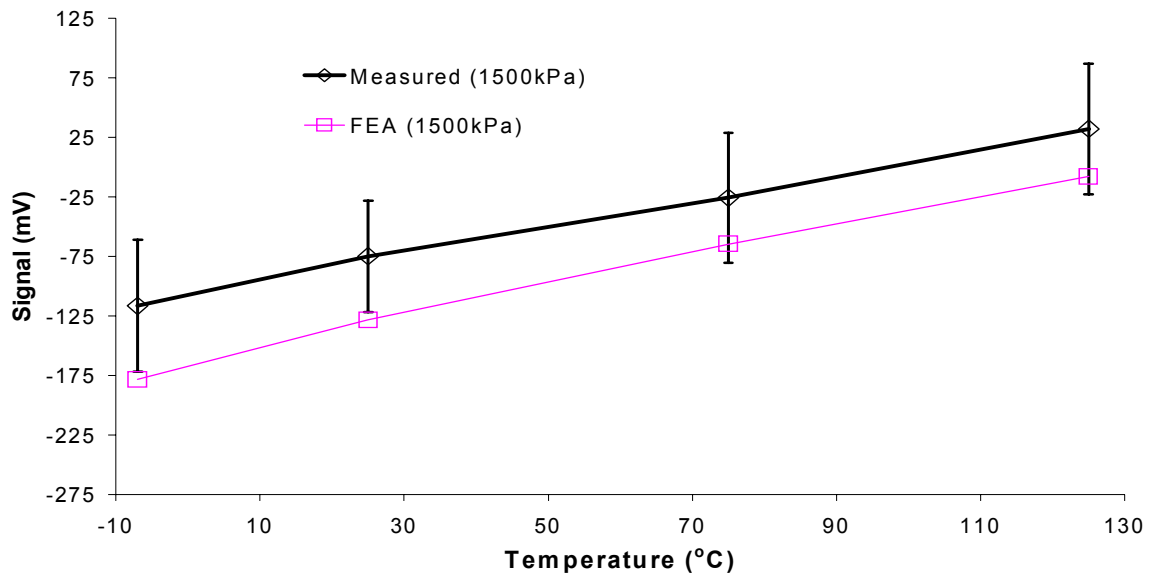
Figure 6.10   Signal vs. temperature for 1500kPa. Error bars represent 3 st. dev.
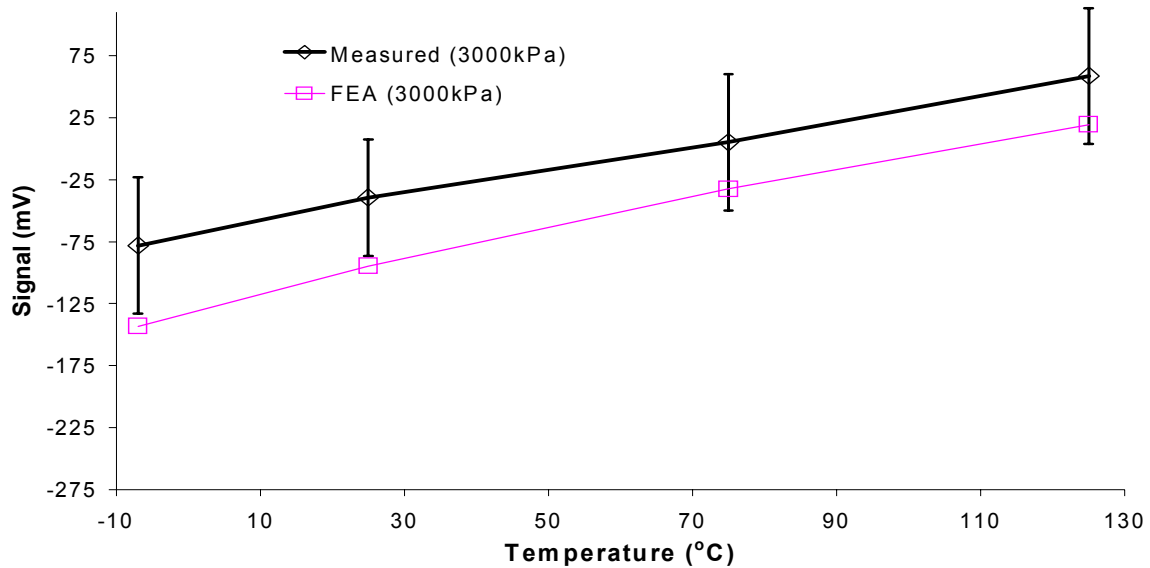
Figure 6.11   Signal vs. Temperature for 3000kPa. Error bars represent 3 st. dev.

The material properties obtained in Chapter 3 showed that the EMC exhibited a viscoelastic response. With viscoelastic material properties, stress relaxation occurs. This would lead to a decrease in the packaging stress and hence the signal offset.

Material properties themselves are always questionable. Although the test specimens and the plastic capsules were made of the same material type and brand, they were not made from the same material production batch. The commercial EMCs are complex materials that might show considerable batch to batch variations in the material properties.

Molecular orientation has an effect on the material properties of polymers. The effect of this for a thermosetting polymer is small. Neglecting this effect was decided to be insignificant to the results.

a)   b)
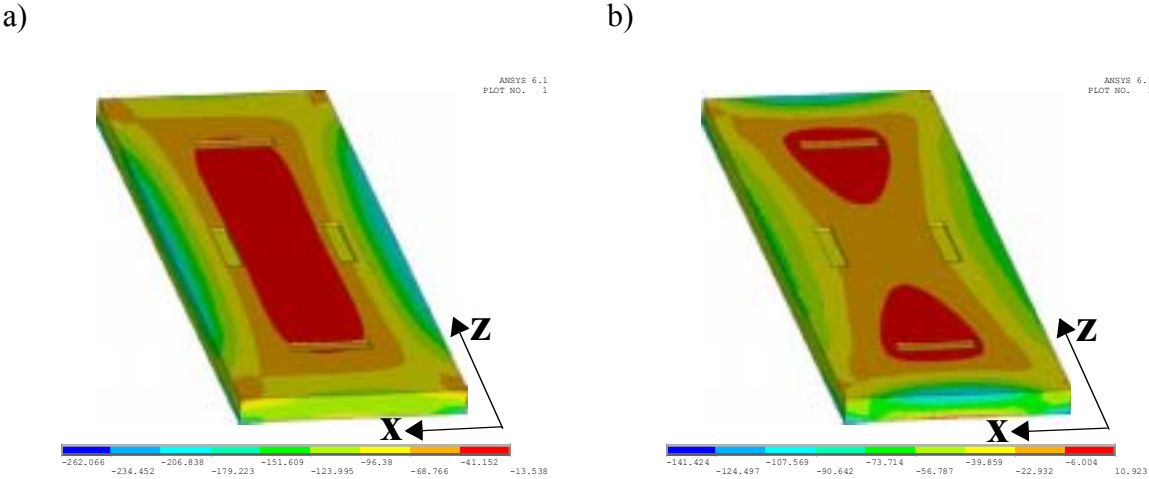
Figure 6.12   Plot of ω_x (a) and ω_z (b) on the membrane at -7°C for a level-1 packaged sensor.
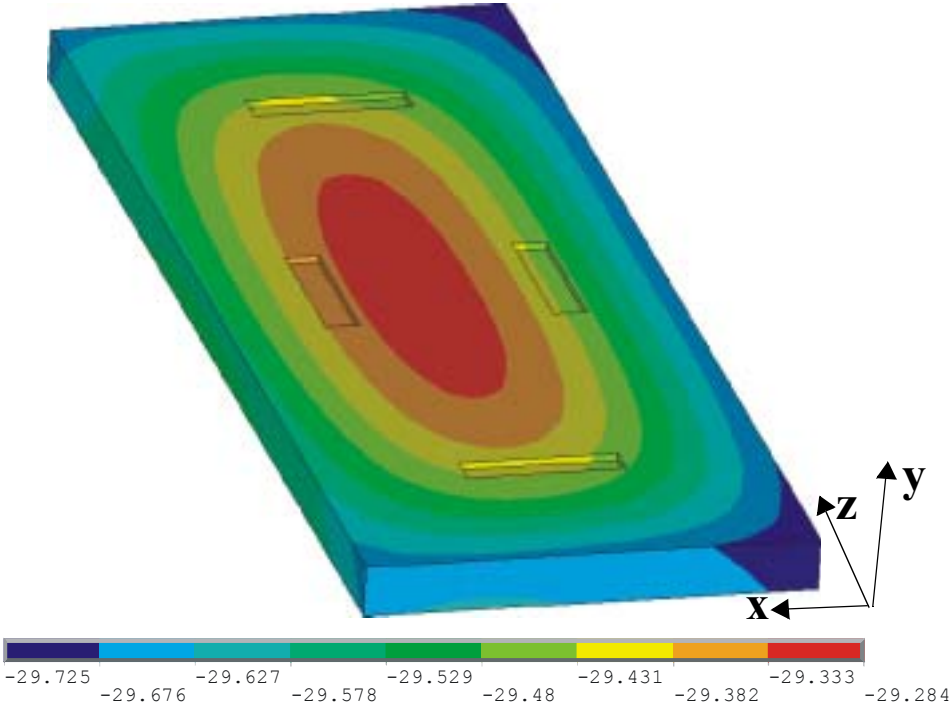
Figure 6.13   Plot of y-displacement on the membrane for -7°C for a level-1 packaged sensor. Note that the legend values are in σm and represent the displacement with respect to the whole structure.

It is important to understand what mechanical loads that caused the offset of the signal. The signal comparison above (Table (6.4) and Table (6.5)) showed that packaging significantly affected the sensor signal. Figure (6.12)a&b shows plots of ω_x and ω_z on the sensor membrane at -7°C for a level-1 packaged sensor. Figure (6.13) shows the y-displacement of the membrane at -7°C and 3000kPa for a level-1 packaged sensor. It is evident that both the stress- and displacement-fields has shifted in the positive x-direction of the membrane. Figure (6.14) shows a 3D surface plot of (6.12)b. The shaded areas represents the resistor locations. The resistors are taken out and their *z*- and *x*-stress components are plotted separately in Figures (6.15)b and (6.16)b respectively. In other words, they represent the same plot as in Figure (6.14), excluding the stress for the rest of the membrane. Figures (6.15)a and (6.16)a shows the z-component of the stress in the resistors in the level-0 packaged sensor found in Chapter 5. The plots shows that the stress in the membrane for the level-0 package is symmetrical in both xy and zy plane.
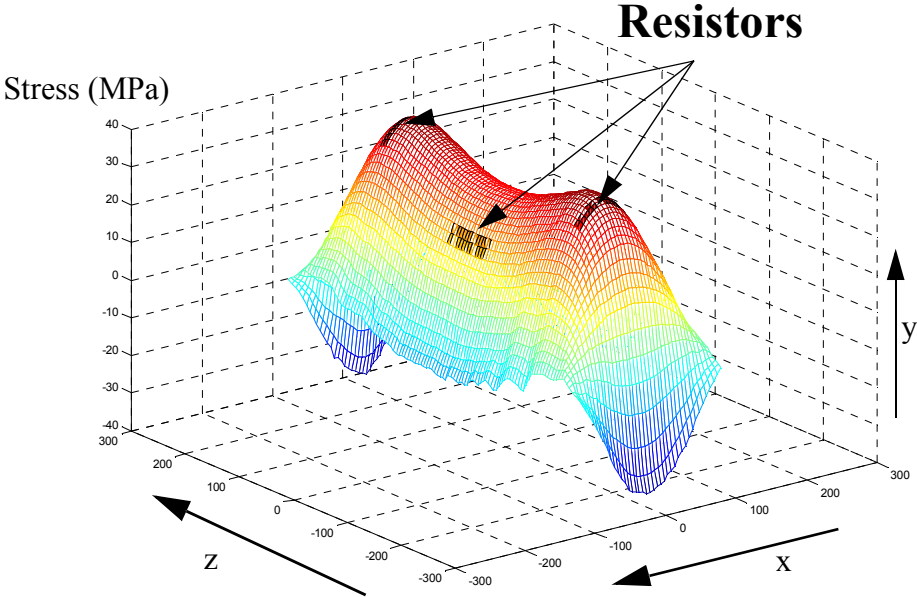
 Figure 6.14   3D-plot of ω_z on the membrane for a level-1 packaged sensor. Shaded parts are resistor placements.

a)

b)
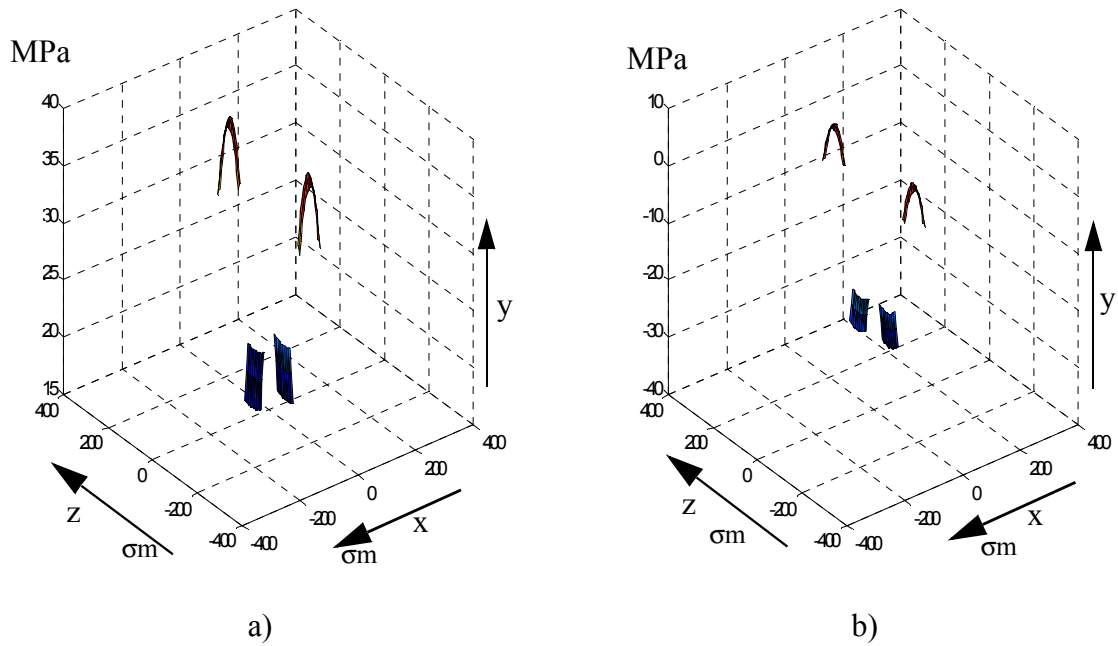
Figure 6.15 ω_z component for the resistors at -7°C for level-0 (a) and level-1 (b) packaged devices.

Figures (6.15)b and (6.16)b shows the x-stress components in the resistors in the level-1 packaged sensor. The difference between the (a) and the (b) plots was clear. The (b) plots shows that the stress field is no longer symmetric in the zy-plane after plastic encapsulation. There was still symmetry in the *xy*-plane as expected since the level-1 package was symmetric in that plane. This observed shift in the stress field was also seen on the contour plots in Figure (6.12).

a)

b)
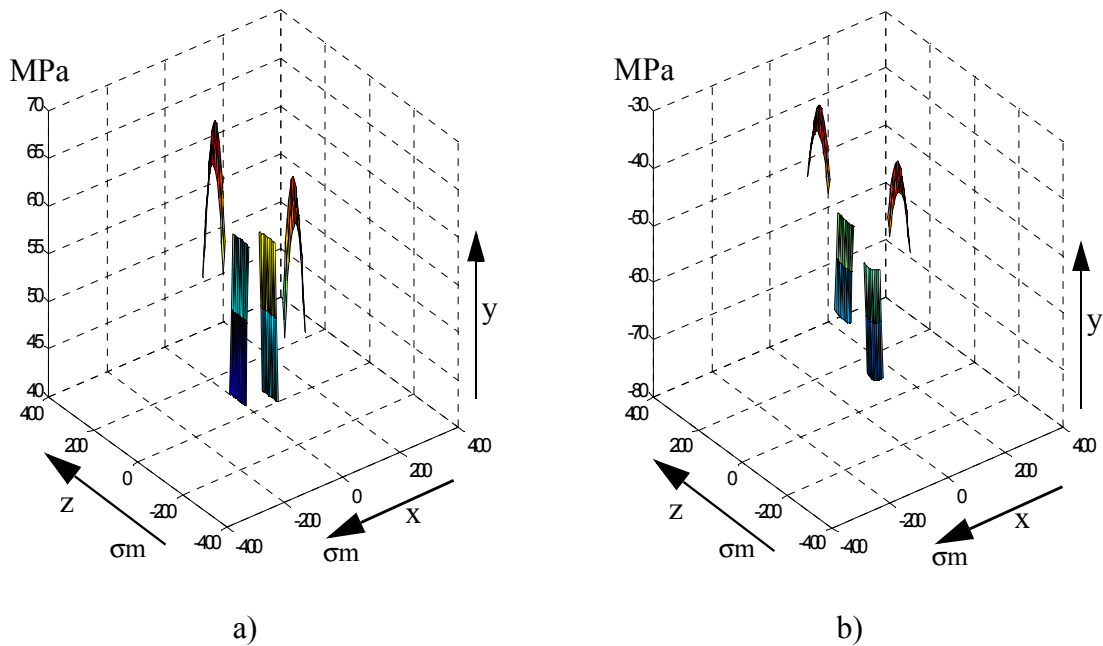
Figure 6.16 ω_x component for the resistors at -7°C for level-0 (a) and level-1 (b) packaged devices.

A special vector plot was developed to understand the nature of the interaction between the level-0 package and the level-1 package. All the areas exposed to the EMC were meshed with surface elements (SURF154). The node numbers of the elements were identified and the nodal force components for each node was extracted. The forces for each element were then summed up and divided by the element area to give a stress vector for each element. These were then plotted using a vector plot. The result can be seen in Figure (6.17) below.
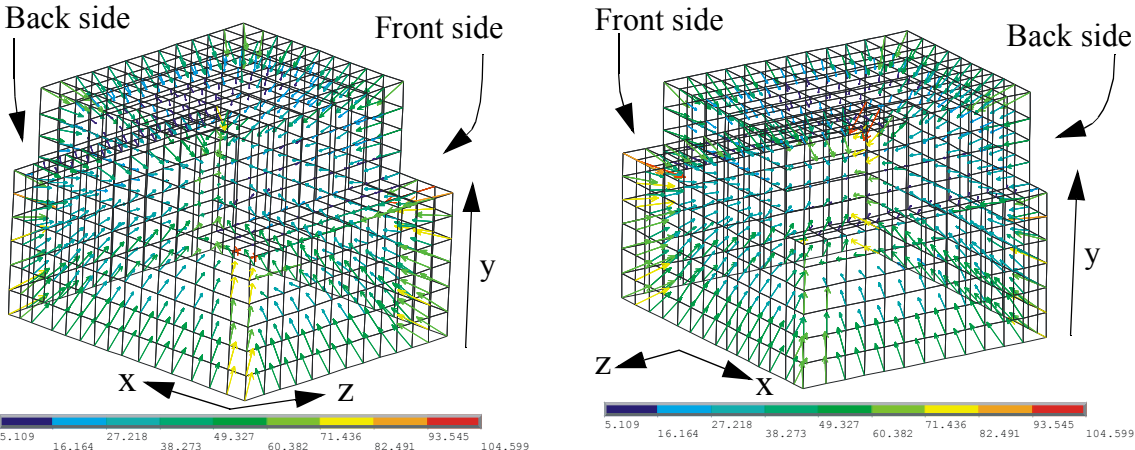
Figure 6.17   Plot of the stress vectors acting from the EMC on the sensor exterior at -7°C.

Knowing that the direction of the packaging stress from the vector plots, a contour plot was used to represent the magnitude of the vectors. Figure (6.18) shows the contours representing the vectors in Figure (6.17). The units on the legends are MPa. The whole package, including
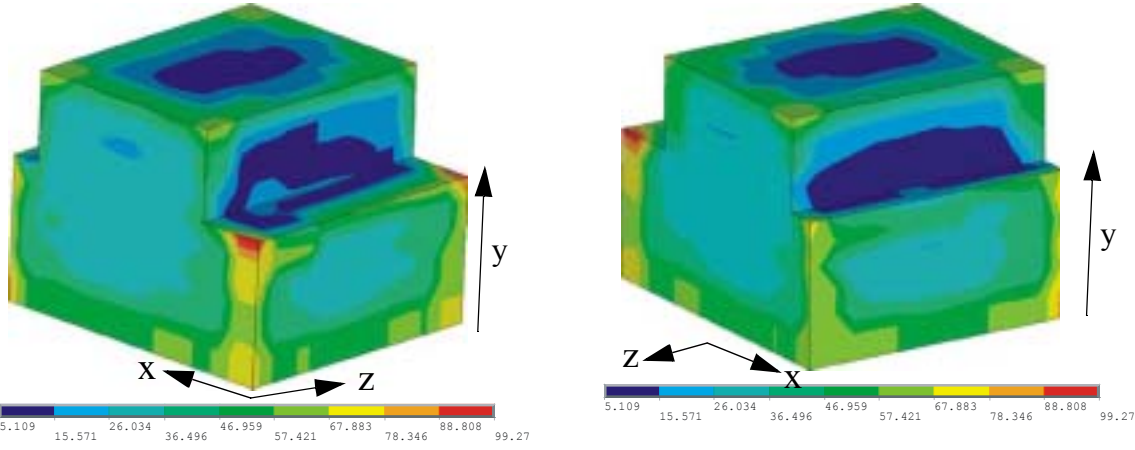
Figure 6.18   Contour plot of the magnitude of the stresses vectors acting from the EMC on the sensor exterior at -7°C.

the sensor, was, as stated previously, symmetrical with regard to the *xy*-plane. The contours plots were not completely symmertrical. This was due to uneven mesh density in the EMC volumes surrounding the sensor die. The symmetry deviations were too small to affect any conclusions drawn here.

Figure (6.18) shows that the pressure on the sides, parallel to xy-plane, was symmetric and even, as expected. The top glass (see Figure (6.5) for a reminder of the glass location) also had an even pressure on both the front and the back side. The situation was different for the silicon member and the bottom glass. A larger pressure was observed on the front surfaces (negative x-direction) than on the back surface (positive x-direction). The front surface had an average pressure of around 30MPa applied to it whereas the back surface experienced approximately 20MPa. This was what induced the shift in the stress field on the membrane observed in Figures (6.12), (6.15) and (6.16). The pressure difference induced the x-displacement field shown in Figure (6.19). The displacement plots correspond to the packaging pressures seen in Figure (6.18). The displacement plots were scaled by a factor of 100.

a)

b)
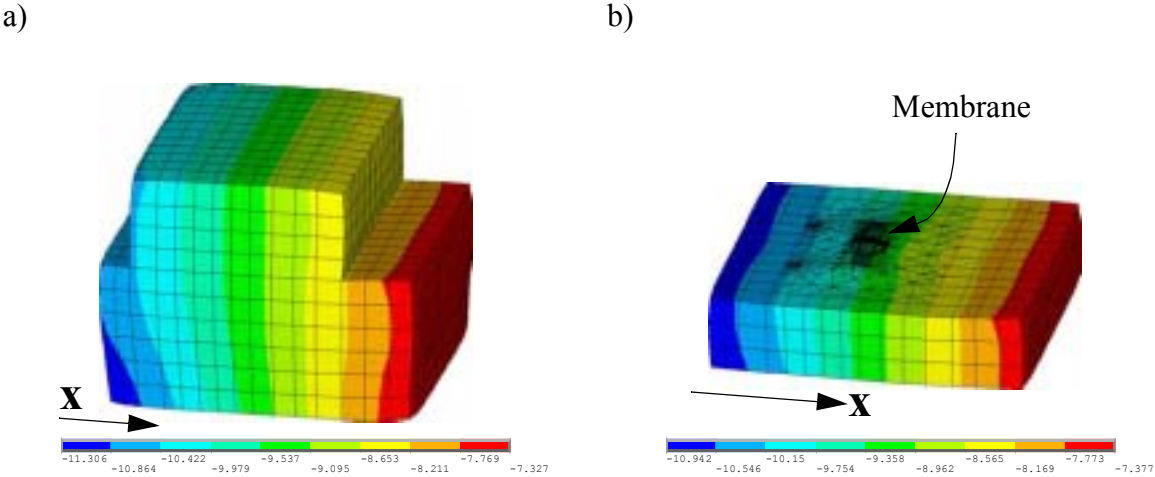
Figure 6.19   Displacement in x-direction for the a) die and the b) silicon member with the membrane.

The ω_x stresses on the membrane were plotted and are show in Figure (6.20). The idea was to get a picture of how the stresses act on the membrane edge. The forces that set up the stress-field seen in the figure created bending moments at the edges of the membrane. The bending moments were found to be 1384367σNσm for the back side and 733010σNσm for the front side of the membrane. This is what caused the shift of the stress- and displacement-field shown in Figure (6.12) and Figure (6.13) and is what causes the offset.

a)

b)
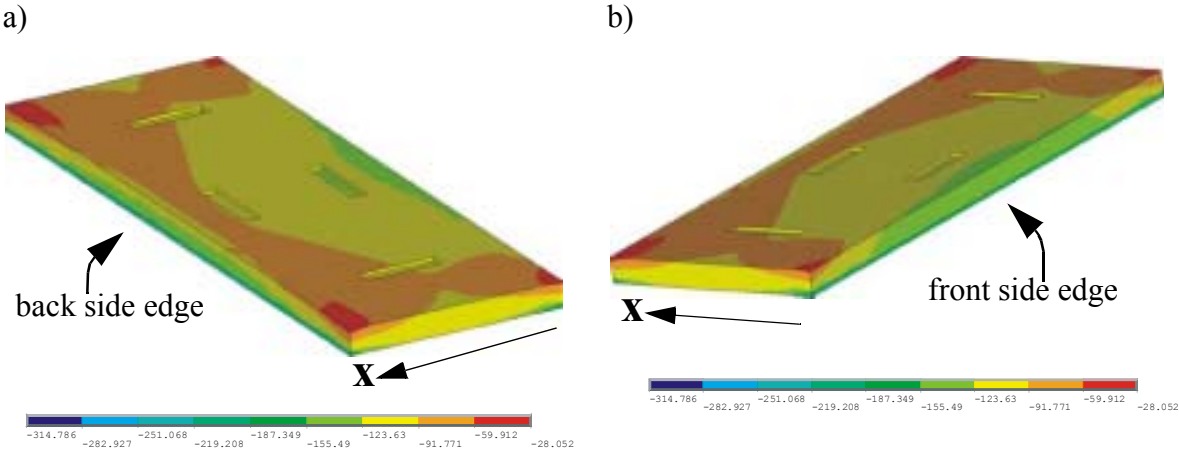
Figure 6.20   Stress plots of membrane showing ω_x at -7°C. a) showing the back side edge and b) showing the front side edge.

Figure (6.21) shows a contour plot of the stresses that acted on the sensor exterior at 25°C. It shows that the stress levels are smaller for 25°C than for -7°C. The relative stress difference between front and back increases with decreasing temperature because of larger CTE mismatch and higher E-modulus of the EMC. This caused the signal offset to increase accordingly.
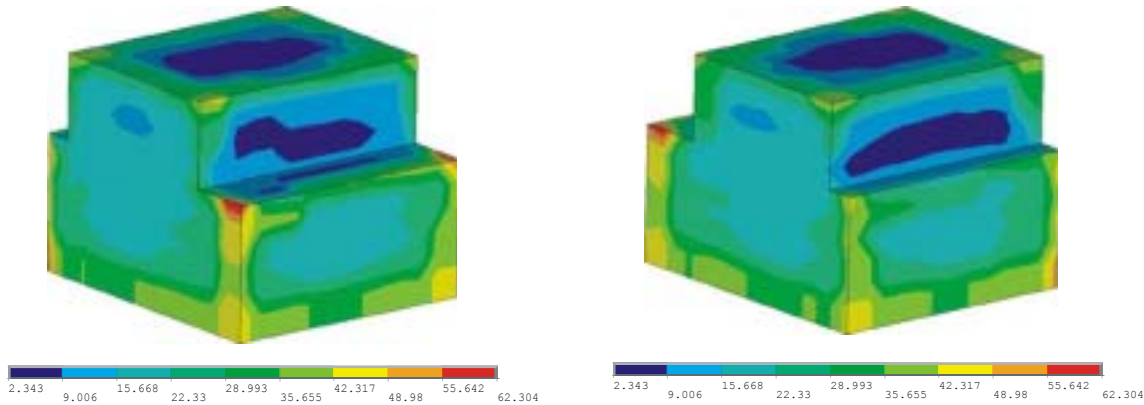
Figure 6.21   Contour plot of the stresses that act on the sensor exterior at 25°C.

6.5 CONCLUSIONS

This chapter started by the development of a full model of the level-1 package. The material data for the EMC was entered as temperature dependent elastic. The model was made parametric for compatibility to design variations. The method outlined in Chapter 5, of extracting an electrical signal from the sensor was used to determine the accuracy and usefulness of the FE model. The sensitivity did not match quantitatively but showed a comparable trend to the measured results. The signal vs. temperature matched at the higher end of the temperature scale, but not at the lower. Several explanations for this were given in the results and discussion section.

A special vector plot was developed to understand the packaging stresses that acted on the sensor die. The vector plot was used together with contour plots to gain a best possible picture of the total package stress.

A shift in the stress- and displacement-fields on the membrane was observed. It was found that bending moments of different magnitudes acted on each long side of the membrane.

CHAPTER 7

PACKAGING STRESS WITH A VISCOELASTIC MATERIAL MODEL

The analysis in Chapter 6 assumed a linear elastic but temperature dependent material model. However, the Epoxy Moulding Compound (EMC) was found to behave viscoelastically. The corresponding material parameters were presented in Chapter 3. In order to improve the numerical results, the effect on packaging stress by treating the EMC as viscoelastic solid was investigated in this chapter. The goal was to obtain a better match to measured data.

7.1 MATERIAL PROPERTIES

The viscoelastic material data was obtained through stress relaxation experiments and were presented in Chapter 3. The WLF shift function was used.

7.2 THERMO-MECHANICAL MODELLING

7.2.1 The Geometry

The geometry used was the same as for the elastic model. The reader is referred to Chapter 6 for details.

7.2.2 The Mesh

The mesh and elements used were the same as for the elastic approach. The reader is again referred to Chapter 6 for details.

7.2.3 Loads

The response of a viscoelastic materials is time dependent. The full loading history used is shown in Figure (7.1). It started with a 2 minute cooldown from the moulding temperature down to room temperature. The hold time at room temperature could be arbitrary depending on equipment and operator availability, but was set to 1 day (1440min) for these simulations. The thermocycles consisted of 60 minutes dwells and 10 minutes temperature changes. The pressure loading phase had 10 minutes temperature changes with 15 minutes dwells. At the end of each 15 minutes dwell, 1 minute was used to apply the pressure loads in 3 substeps (0kPa at 0min, 1500kPa at 0,5min and 3000kPa at 1 min.)
.
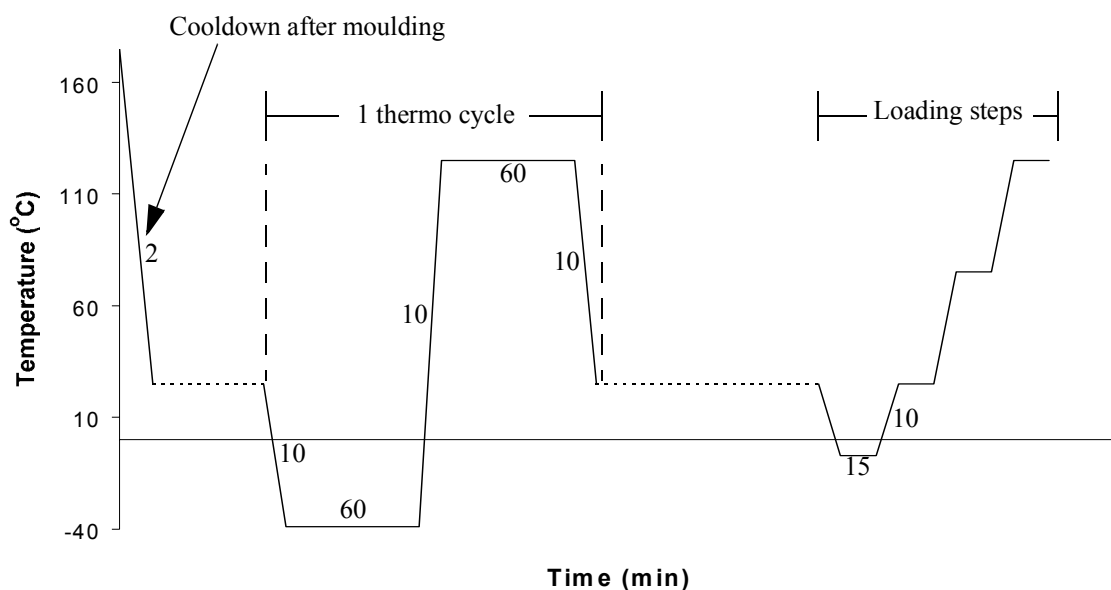
Figure 7.1   Temperature history.

7.3 RESULT & DISCUSSION

Tables (7.1), (7.2) and (7.3) below show the output signal values that were obtained from the FEA model after running the model through 1, 3 and 6 thermocycles respectively. All three cases showed smaller offset values than those obtained for the elastic case in Chapter 6. In Figure (7.2) the contour plots shows 20% lower stresses compared to the corresponding elastic case, compare to Figure (6.18). This complies with the results in Chapter 5 where it was found that an increased external pressure on the sensor die caused a larger offset. The reduced stress is due to the stress relaxation in the material. The tables also show that the signal values decreased with increasing number of thermo cycles for all temperatures. This was a result of a reduced packaging stress as a function of the number of thermo cycles. This is again an effect of the stress relaxation and hence load redistribution. In fact, thermocycling is often called destressing in the microelectronics industry. Stress relaxation is a function of time and temperature.

Table 7.1: Calculated signal values for 1 cycle [*mV/V*]

Pressure (kPa) / Temperature (C)	-7.5	25	75	125
0	-43.63	-29.70	-14.07	-1.97
1500	-35.92	-22.84	-8.20	3.20
3000	-28.21	-15.99	-2.32	8.42
Sensitivity [σV/V/kPa]	5.14	4.57	3.92	3.46

Table 7.2: Calculated signal values for 3 cycles [*mV/V*]

Pressure (kPa) / Temperature (C)	-7.5	25	75	125
0	-42.77	-28.92	-13.39	-1.48
1500	-35.06	-22.06	-7.52	3.69
3000	-27.36	-15.21	-1.64	8.90
Sensitivity [σV/V/kPa]	5.14	4.57	3.92	3.46

Table 7.3: Calculated signal values for 6 cycles [*mV/V*]

Pressure (kPa) / Temperature (C)	-7.5	25	75	125
0	-42.62	-28.78	-13.27	-1.38
1500	-34.91	-21.92	-7.40	3.78
3000	-27.21	-15.07	-1.52	9.00
Sensitivity [σV/V/kPa]	5.14	4.57	3.92	3.46

No evidence of a change in sensitivity with the number of thermo cycles were observed. This was counter intuitive to the results from Chapter 5 where it was found that a pressure load on the external surfaces of the die lowered the sensitivity. From those results it was expected to see an increase in sensitivity for more thermo cycles because of the decrease in packaging stress. Figure (7.2) show evidence of destressing on the die as a function of the number of thermo cycles. The maximum exerted pressure at -7°C decreased from 82MPa for 1 thermo cycle to 80 MPa for 6 thermo cycles. The same trend was found for 25°C and 75°C (plots located in Appendix D).

1 Thermo cycle   6 Thermo cycles
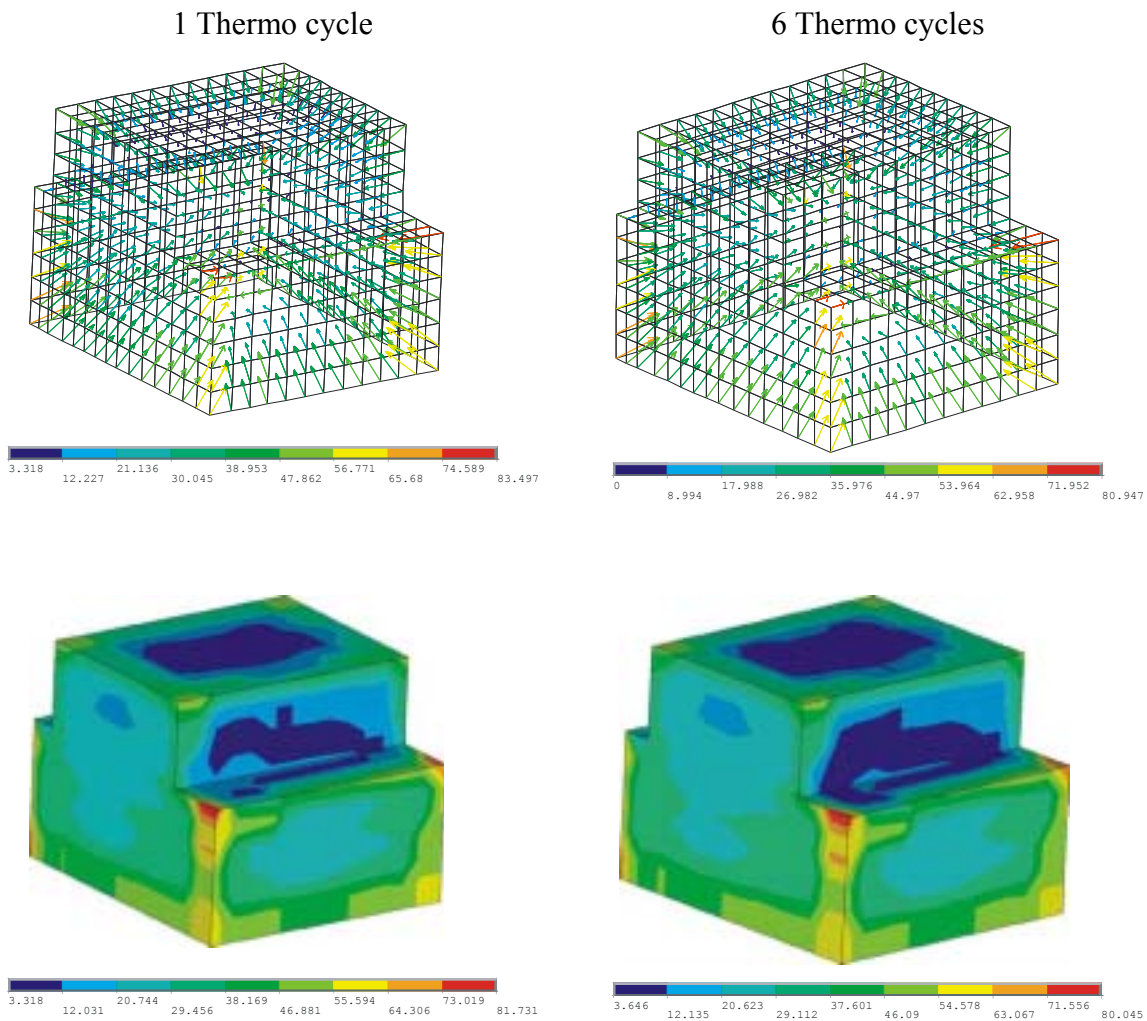
Figure 7.2   Comparison of packaging stress at -7$^\text{o}$C for 1 and 6 thermo cycles.

In Chapter 6 packaging stress (from the elastic EMC) was found to create a signal offset. It was found that the larger the packaging stress, the larger the offset. The results from the viscoelastic material model clearly results in less packaging stress and less signal offset.

The observed decrease in packaging stress with the number of thermo cycles was the result of load redistribution in the EMC because of irreversible shape changes that occur when the material flow.

The accuracy of the model could only be determined indirectly. As before, the indirect test was to see how well the output signals from the model matched the measured output signals. The same 8 dies that were used in Chapter 6 were also used here. The errorbars again represent 3 standard deviations of the measurement data. All the measurement data can be found in Appendix C.

The sensitivity predictions are shown in Figure (7.3). Only the sensitivity at 125$^\text{o}$C deviated from the elastic case. No difference was observed in the estimated sensitivity for 1, 3 and 6 thermo cycles, hence the single line representing the results from the viscoelastic FEA simulations. It is clear from the plot that the material model had little effect on the sensitivity of the sensor. This indicated that the sensitivity was not strongly dependent of packaging stress. Table (7.4) below shows a comparison between the sensitivity for a bare die and a packaged die. The sensitivities in the table were obtained from the FEM model. The pressure was applied only at the

pressure inlet in both cases. A maximum difference of 4% in sensitivity is observed. This deviation has to come from the package stress. Hence, by going from zero packaging stress (bare die) to a packaged die (with the corresponding packaging stress), the sensitivity changes by only 4%.

Table 7.4: Sensitivity [$\sigma V/V/kPa$] comparison of bare die and packaged die

	Temperature			
	-7	**25**	**75**	**125**
Bare die	6.48	5.81	5.02	4.42
Packaged	6.75	6.04	5.20	4.62
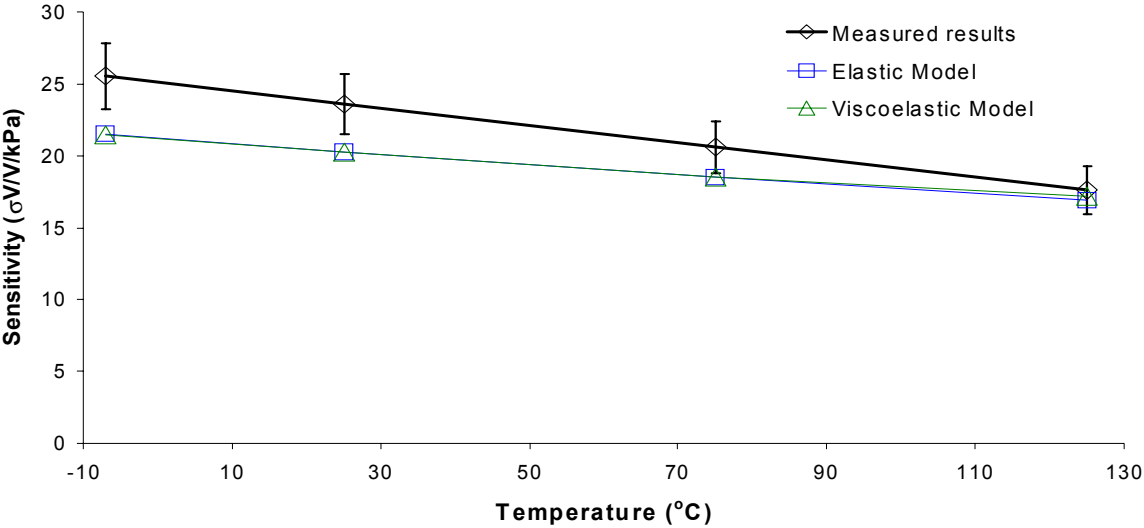
Figure 7.3   Sensitivity of the elastic- and viscoelastic model compared to the measured values.

Figures (7.4) and (7.5) shows the comparison of the output signal as a function of temperature from the model and the measurements, at 1500kPa and 3000kPa respectively. In Chapter 5 it was stated that all the sources for offset were not included in the model. This again meant that a perfect match of the signal values were not expected. The errorbars in the figures represent 3

standard deviations of the measurements. All the datapoints from the viscoelastic model fall inside the errorbars. The curve trend also compared well to the measurements.
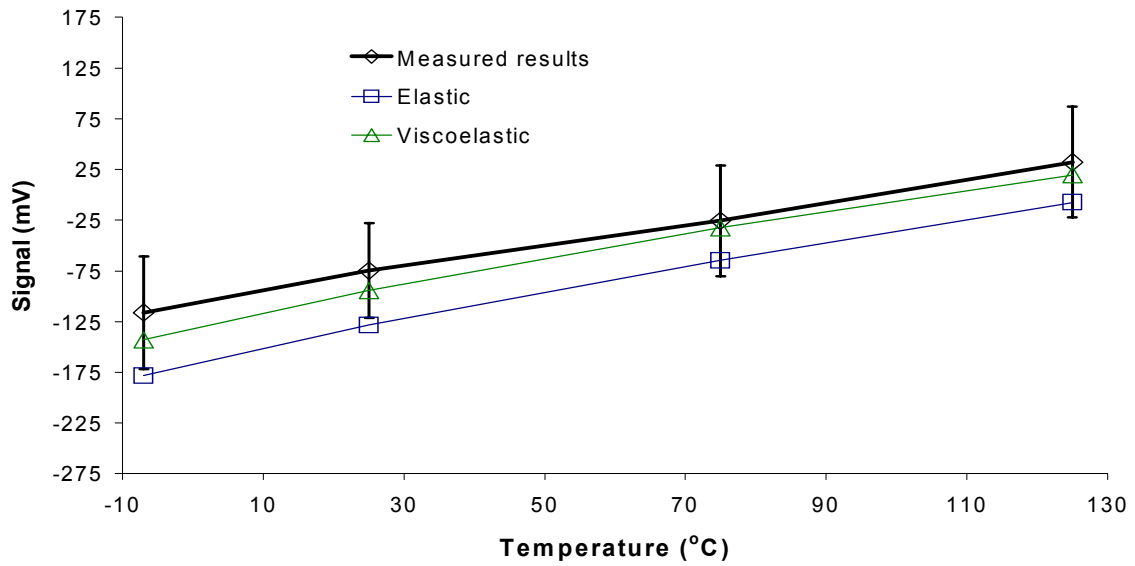
Figure 7.4   Signal from the elastic- and viscoelastic model compared to the measured values at 1500kPa.
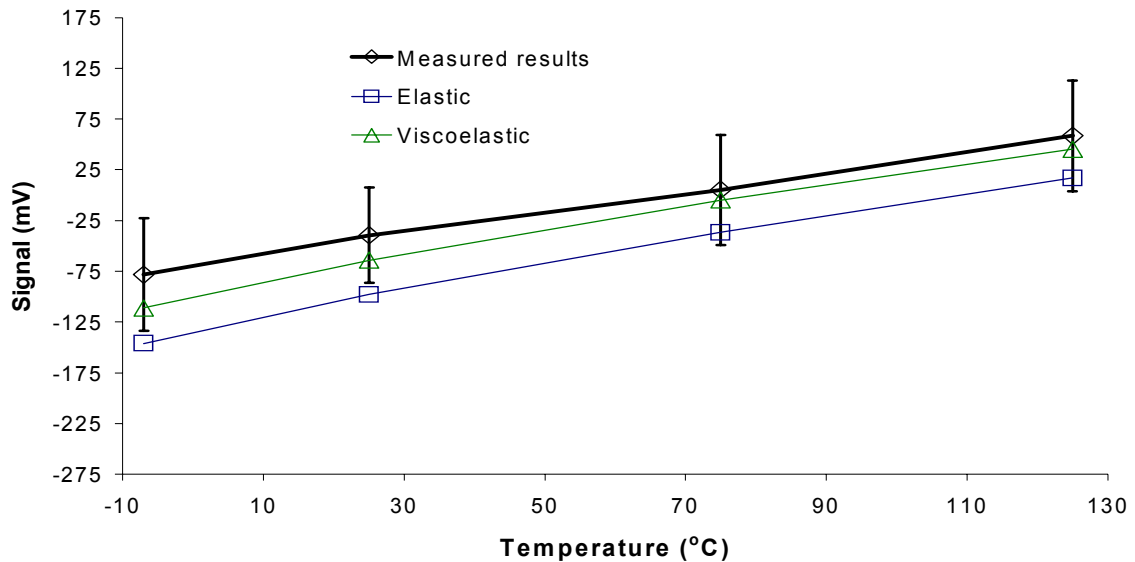
Figure 7.5   Signal from the elastic- and viscoelastic model compared to the measured values at 3000kPa.

The reasons for the discrepancies observed include the same reasons as in Chapter 6. In addition to them, there was also the issue of the viscoelastic material data. Stress relaxation exper-

iments were only conducted for temperatures between 35 and 175°C whereas the simulations included temperatures from -40 to +175°C. The stress relaxation master curve is expected to change marginally in the glassy and rubbery regions at low and high temperatures respectively. One can therefore be confident that for all practical purposes, the curve was representative for the material since the data around T_g had been thoroughly collected. The effect of the slight lack of fit between the measured shift function and the WLF was considered to be too cumbersome to investigated. See also Chapter 8.

The temperature loads applied were in the form of uniform temperatures. This meant that the whole structure was set to a uniform temperature and the thermal strains were calculated with respect to the reference temperature. This would never be the case in reality as heat always has to be conducted to and transferred into the structure. Therefore it will take time to obtain a uniform temperature which could result in a different stress picture inside the package than that obtained using the uniform temperature assumption. As stated, the viscoelastic material is dependent on temperature and strain history, both of which would change with a transient temperature consideration.

7.4 CONCLUSIONS

The results showed that a viscoelastic material model should be used for accurate packaging stress simulations of the plastic package. The viscoelastic material data resulted in less stress on the die as was anticipated. This was due to stress relaxation in the moulding compound. It was also found that the packaging stress levels for all temperatures decreased with increasing number of thermocycles applied to the package. Load redistribution was given as the cause for this.

The sensitivities from the simulations using viscoelastic material properties was found to yield the same result as for the elastic material model. It was found that sensitivity showed negligible dependence on packaging stress.

CHAPTER 8

MATERIAL PROPERTY INFLUENCE ON THE RESULTS

This chapter aims to discuss the sensitivity of the FE analysis to material property variations.

8.1 THE PARAMETERS OF VARIATION

The parameters that were investigated were glass transition temperature, CTE, viscoelastic shift function and Poisson's ratio of the moulding compound. The basis for all the simulations in this Chapter was the model and material properties used in Chapter 7.

8.2 RESULTS

8.2.1 CTE variations.

The Epoxy Moulding Compound (EMC) manufacturer has the following specifications on CTE,

$$\zeta_1 = 9\Delta10^{-6} \partial 3\Delta10^{-6}/\forall C$$

$$\zeta_2 = 32\Delta10^{-6} \partial 15\Delta10^{-6}/\forall C$$

which are relatively wide. ζ_1 and ζ_2 is defined as the CTE below and above T_g respectively. For the simulations here, it was assumed that if ζ_1 was low, then so was ζ_2. This was thought to be valid since CTE is very much controlled by the amount of quartz filler that is mixed into the EMC. Hence, the more quartz, the lower the CTE becomes for both below and above T_g. Figure (8.1) below shows the results from the simulations of three different CTE cases (minimum, nominal and maximum.) The experimentally measured results are also included in the plot. The figure shows that the output signal was very dependent on the CTE value of the moulding compound.

The minimum CTE values produces a signal vs. temperature curve that lies slightly above the measured results.

The curve that was produced with the nominal values lies below the measured results and has the best trendwise fit of the three CTE cases.

The maximum CTE values produced a curve that mostly lay outside the 3 standard deviation errorbars of the measured results. The trend also showed a strong deviation from the measured results.

Signal offset was identified in Chapter 6 to be caused by uneven bending moments on the membrane as a result from unsymmetrical packaging stress on the sensor die. It is clear from Figure (8.1) that the signal offset increase with increasing CTE values. This was also expected since the magnitude of the CTE is proportional to the packaging stress.

 Figure 8.1   Signal vs. temperature for 3000kPa for three different CTE cases. The errorbars represent 3 standard deviations of the measured dataset.

   Figure (8.2) shows sensitivity vs. temperature for the three different CTE cases. The maximum deviation among the simulated results is 1.5% and occur at -7°C. This was an interesting observation and again proved that the sensor sensitivity was almost unaffected by packaging stress. This is because the sensitivity is a measure of signal change for any given pressure change. The packaging stress from the cooldown shrinkage will only set the initial stress state in the membrane, it does not alter the stress on the membrane as a function of pressure change.
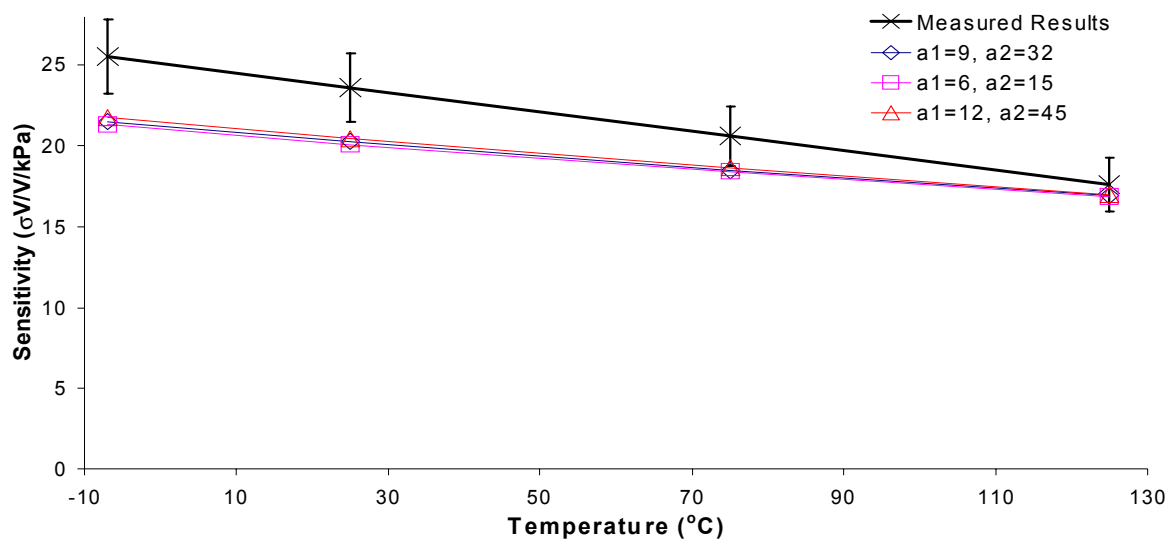
 Figure 8.2   Sensitivity vs. temperature for the different CTE cases. The errorbars represent 3 standard deviations of the measured dataset.

8.2.2 Variation of T_g

Glass transition temperature was varied between 105°C and 130°C in the model. The measured material data in Chapter 3 had a T_g of 130°C. Since no stress relaxation measurements from a 105°C-T_g-material existed, the data had to be created. This was done by assuming the same set of measurement data that was used in Chapter 3, but assigning different temperatures to them. This meant the following; T_g was lowered by 25°C, i.e. the stress relaxation data that was obtained for 35°C was now assigned 35-25=5°C and so forth. The viscoelastic shift function was adjusted by simply changing the reference temperature from 35°C to 5°C. Also the E-modulus for 125°C had to be changed from 14200MPa to 7000MPa, since it then fell above T_g.

Figure (8.3) shows that a change in T_g contributed significantly to the output signal. T_g of 130°C gave an output signal that was within 3 standard deviations of the measured results. T_g of 105°C gave a significantly different curve. This was again caused by of the strong dependence on CTE that was shown in section 8.2.1 and a lower E-modulus at 125°C. In a cooldown from 175°C, the material stays longer in the high CTE region if it has a T_g of 105°C than if it had 130°C. This causes larger thermal strains and hence larger signal distortion. The lower T_g also gives a lower E-modulus at 125°C which causes less signal distortion and hence a worse trend-fit.
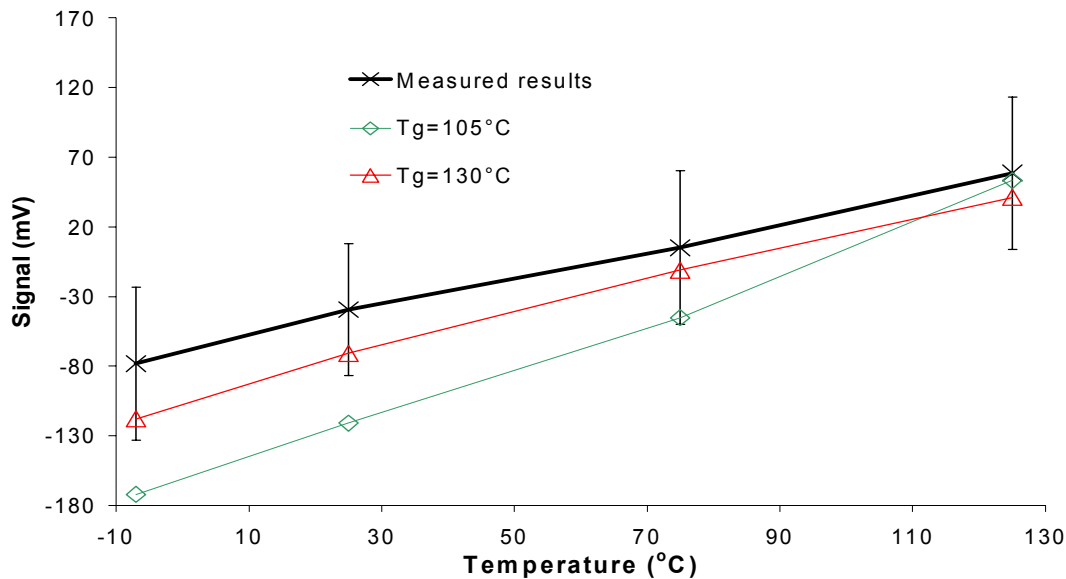
Figure 8.3   Signal vs. temperature for 3000kPa for Tg. The errorbars represent 3 standard deviations of the measured dataset.

Figure (8.4) shows the sensitivity vs. temperature for the two T_g cases with the measured results. It is seen that the largest difference is found at 125°C.
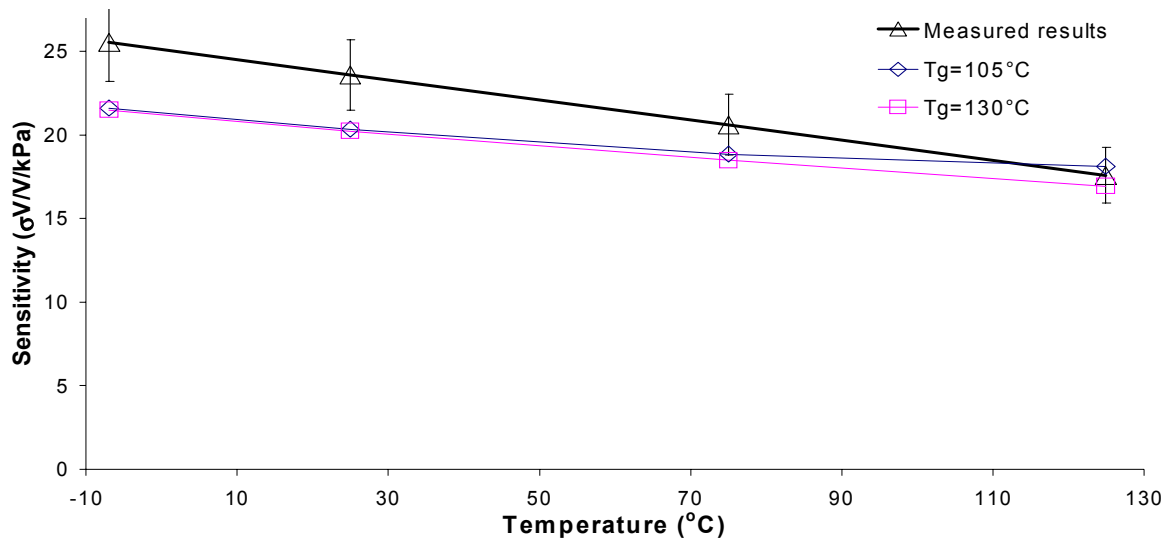
Figure 8.4 Sensitivity vs. temperature for T_g variation. The errorbars represent 3 standard deviations of the measured dataset.

8.2.3 Viscoelastic shift-function variation.

The WLF equation is restated below in Equation (8-1),

$$\log a_t \; = \; \frac{-a/T - T_0 0}{b + T - T_0} \tag{8-1}$$

where $T_0 = 303K$ was the reference temperature and a, b - were fitted constants. Two sets of fitted constants were found and are shown in Table (8.1) below. Figure (8.5) shows a plot of the two shift functions with the experimental data. Shift function #2 was used in Chapter 7.

Table 8.1: Constants used in the two WLF shift functions.

	a	b
Shift Function #1	-100	1100
Shift Function #2	-34	-586
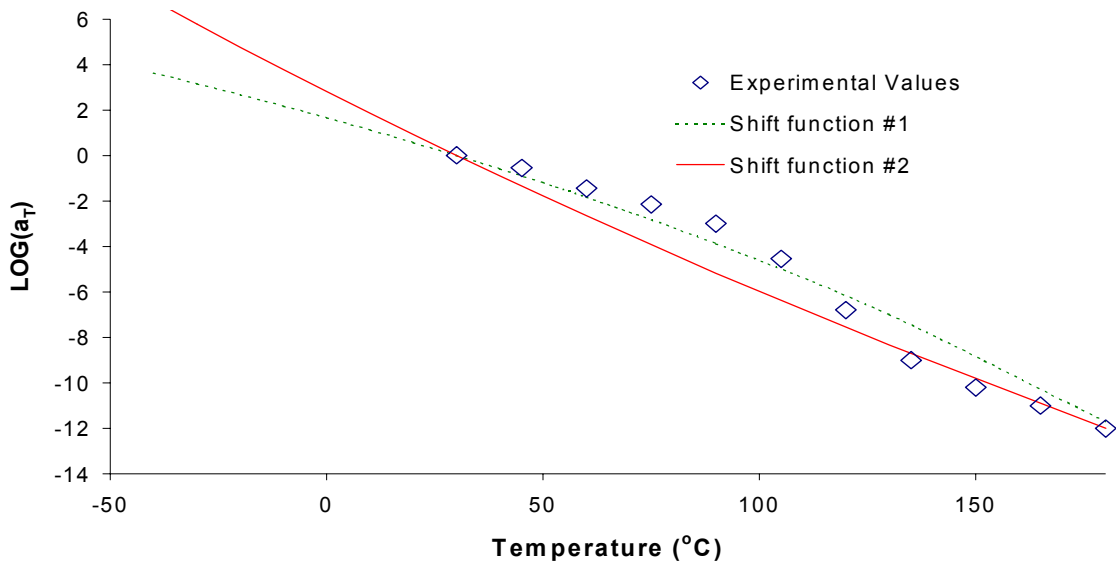
Figure 8.5 The two different shift-functions with the experimental data.

Figure (8.6) shows that the change in shift function resulted in small changes in the output signal curve. Figure (8.7) shows how the sensitivity changed with shift-function variation. There is a significant difference at 125°C. This is due to shift function #1 giving less shift at 130°C. The smaller shift factor means that the material behaves more stiffly. The stiffer the material, the less of the externally applied pressure propagates through to the sensor.
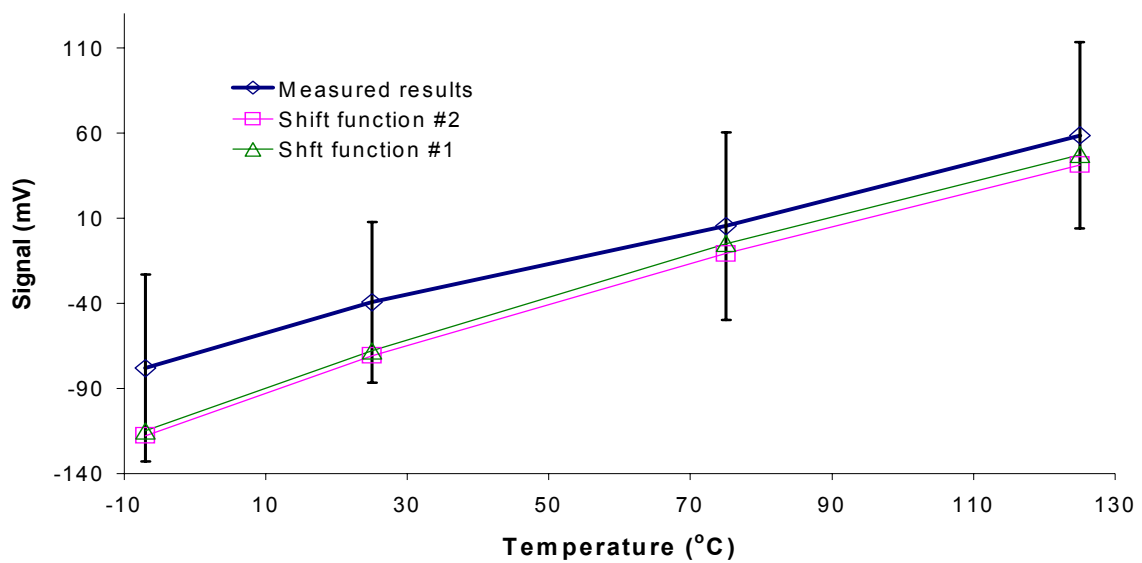
Figure 8.6 Signal at 3000kPa for the two different viscoelastic shift functions. The errorbars represent 3 standard deviations of the measured dataset.
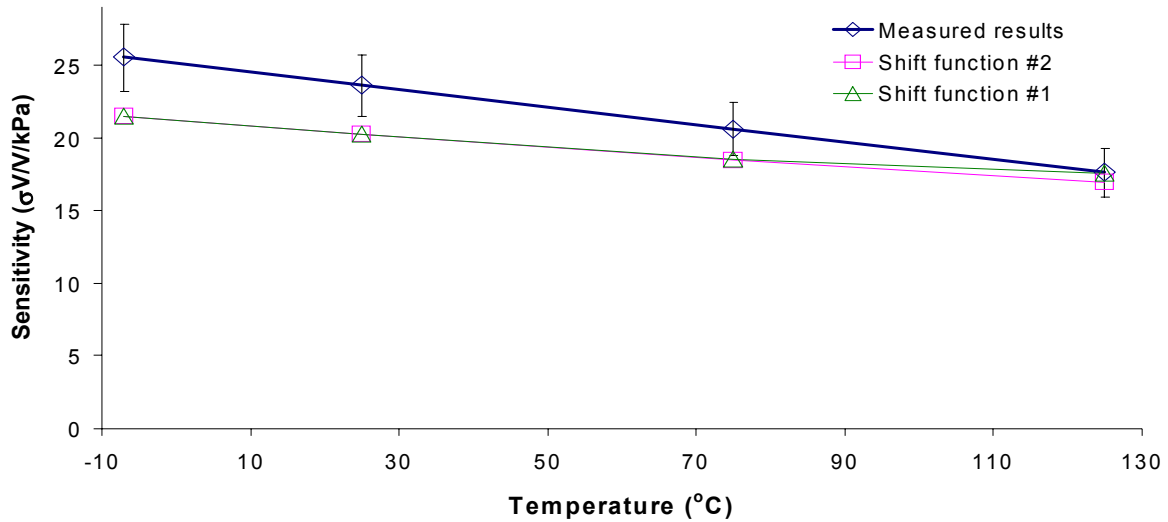
Figure 8.7   Sensitivity vs. temperature for shift function variation. The errorbars represent 3 standard deviations of the measured dataset.

8.2.4 Poisson's ratio variation

In polymers, Poisson's ratio change with temperature and especially when T_g is included in the service temperature range. Above T_g, polymers become nearly incompressible and the Poisson's ratio approaches 0.5. An EMC of the kind used in this work is highly filled and will therefore show a lesser value than 0.5. Two cases were simulated here to see the effect of Poisson's ratio on the model. The two cases used constant isotropic Poisson's ratio of 0.26 and 0.36 for all temperatures. The result of this on the signal values is shown in Figure (8.8) and the result on the sensitivity is shown in Figure (8.9).

It is seen that an increase in Poisson's ratio from 0.26 to 0.36 gives a small change in the signal values. 0.26 was the value used in Chapter 7.

Figure (8.9) shows that the sensitivity changes significantly with a change in the Poisson's ratio.
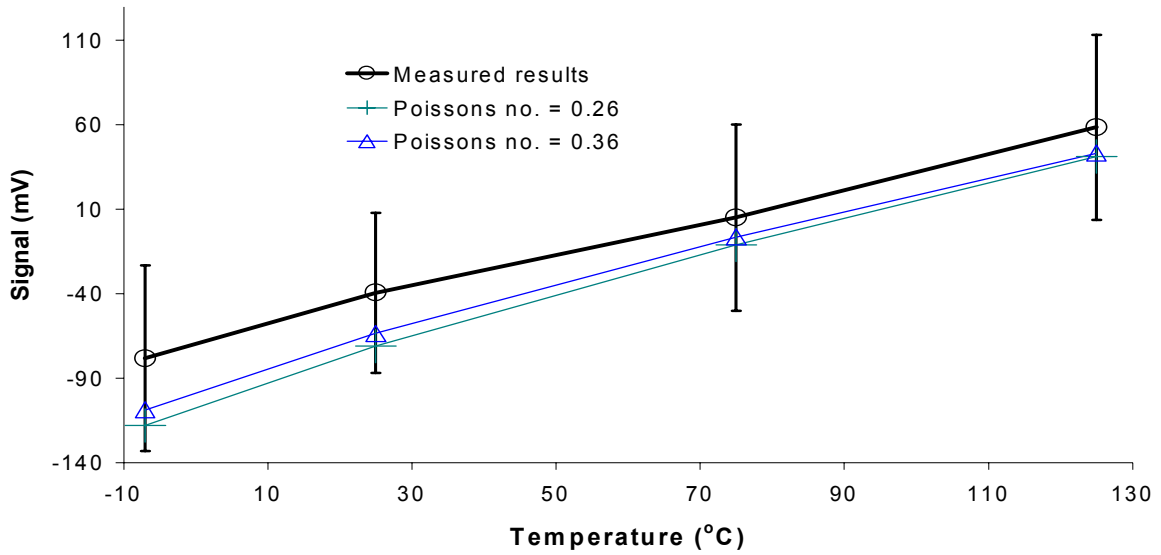
 Figure 8.8   Output signal for 3000kPa for Poisson's ratio variation. The errorbars represent 3 standard deviations of the measured dataset.
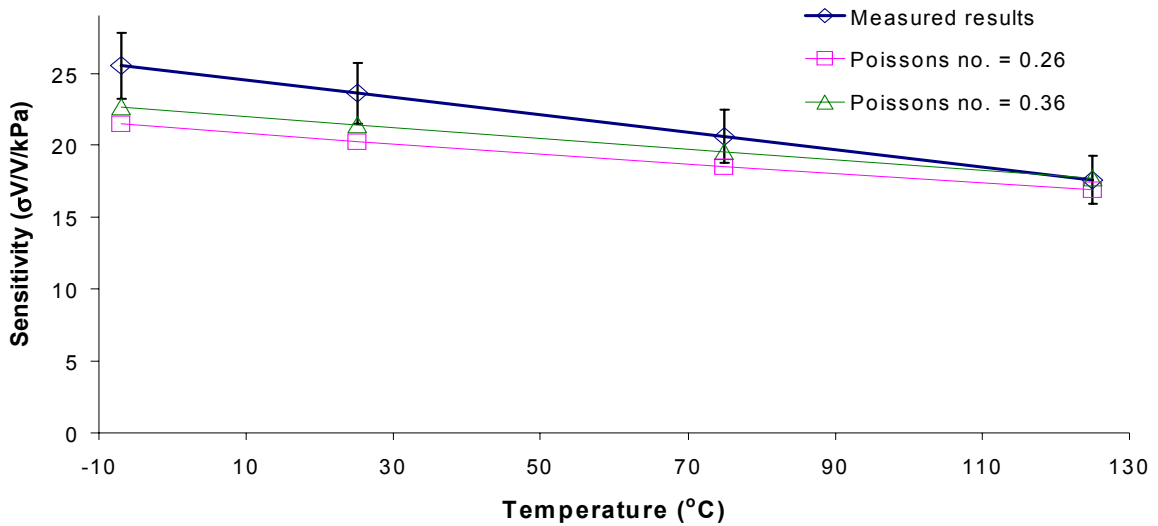
 Figure 8.9   Sensitivity vs. temperature for Poisson's ratio variations. The errorbars represent 3 standard deviations of the measured dataset.

8.2.5 Loading conditions

Two simulations were run to look at the difference in output signal for different loading conditions. One was to apply pressure only through the pressure inlet port, the other was to apply pressure to all exposed surfaces.

Figure (8.10) shows the simulated sensor signal vs. temperature at 3000kPa for a pressure sensor component loaded only through the pressure inlet port and for a component loaded on all exposed surfaces. It is clear from the figure that the loading condition of the applied pressure does change the output signal. The sensitivity curves for the same loading conditions is shown in Figure (8.11). It is seen that the sensitivity decreases when pressure is applied on all surfaces and not only applied to the pressure inlet port. This is the same findings that were made in Chapter 5 for the bare sensor die situation.
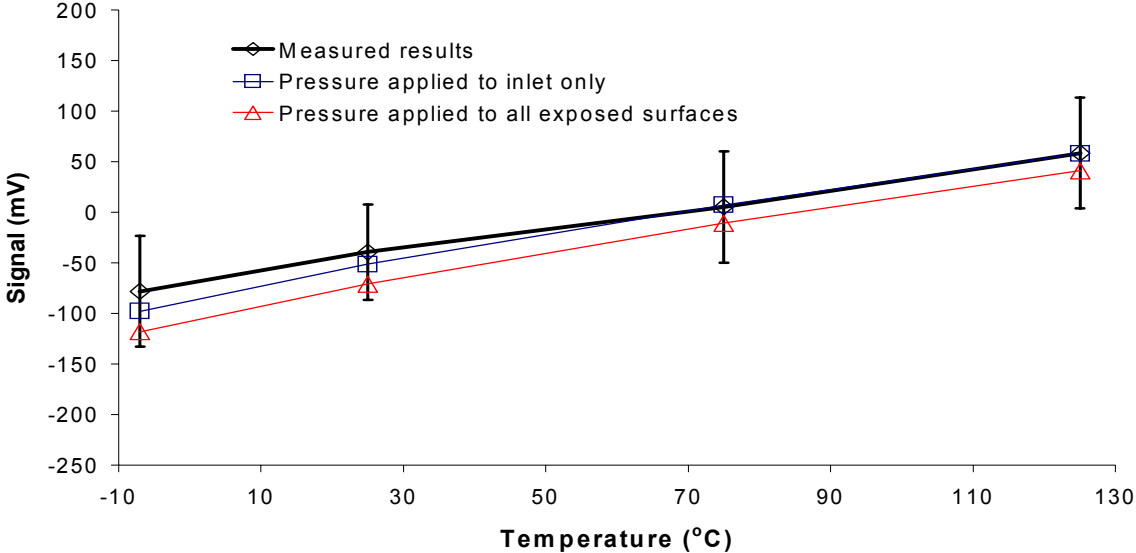
Figure 8.10   Signal at 3000kPa for the two different pressure loading conditions. The errorbars represent 3 standard deviations of the measured dataset.
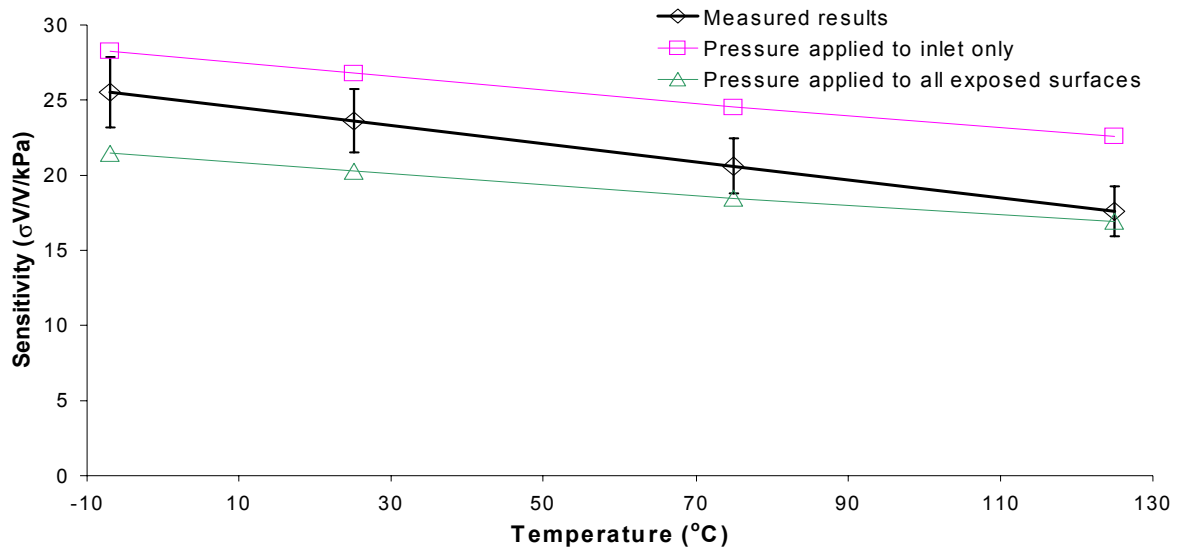
Figure 8.11   Sensitivity vs. temperature for the two different pressure loading conditions. The error-bars represent 3 standard deviations of the measured dataset.

8.3 CONCLUSIONS

It was shown that changes in CTE mainly altered the output signal and did not alter the sensitivity of the device. Changes in Poisson's ratio had the opposite effect. By changing Poisson's ratio from 0.26 to 0.36, the output signal change was small, but the sensitivity changed significantly.

Two different viscoelastic shift functions were also tested. Small differences were observed for both the output signal and most of the sensitivity vs. temperature curve. Only the sensitivity at 125°C deviated significantly between the two cases. Higher material stiffness for one of the shift functions was given as the reason for this.

Change in Tg resulted in significant change of output signal. The reason for this was explained by CTE considerations and lower E-modulus for the low-T_g case.

It was also seen that the pressure loading conditions had a significant impact on the behaviour of the MEMS device and specially for the sensitivity.

This chapter has shown that the behaviour of the MEMS pressure sensor depends largely on the material properties of the moulding compound. It is therefore very important to fully characterize the EMC in question to obtain good results.

CONCLUDING REMARKS

This dissertation started by giving a general introduction to MEMS packaging in Chapter 1. It then went on, in Chapter 2, to give the reader an overview of the theories used throughout the dissertation. The dissertation has focused on the effect of packaging stress on MEMS devices.

Chapter 3 presented the thermomechanical material characterisation that was conducted on the Epoxy Moulding Compound (EMC) that was used in this work. Coefficient of thermal expansion and modulus of elasticity was measured as a function of temperature.

Chapter 4 presented a study of the plastic processing CFD code C-Mold and its capabilities to simulate the transfer moulding process for MEMS packaging. It was found that the software and its 2.5D simulations could not predict the cavity filling of the SOP in this work because of the geometry. The geometry of a MEMS plastic package is different compared to traditional IC packages. MEMS devices are often packaged in two levels, level-0 and level-1. Level-0 is the package that creates the controlled environment surrounding the MEMS transducer or actuator. The controlled environment is needed to keep the transducer or actuator out of reach from unwanted external influence. The level-0 package of the MEMS device in this work is about 5 times higher than traditional ICs. The footprint can be the same or less. The added height of the level-0 package gives the SOP a geometry that is unsuited for the 2.5D simulations in C-Mold. It was found that a full 3D simulation tool would be needed to simulate the packaging process precisely.

To simulate packaging stress, the commercially available finite element code, ANSYS^{TM}, was utilised. Chapter 5 of this work presented the development of a novel approach to obtain accurate piezo-resistance in a piezo-resistor. A commercially available family of piezo-resistive pressure sensors were simulated. These pressure sensors consisted of a silicon diaphragm with implanted piezo-resistors. The piezo-resistors were arranged in a Wheatstone bridge which converted the change in piezo-resistance into a change in electrical voltage signal. A novel method of converting the mechanical stresses from the FEA to electrical signals, for direct comparison to measured data, was developed. The results from the FEA were verified for 25°C and the model was calibrated to give it an accurate response over a wide temperature range. The FEA model included the level-0 package. It was found that the inclusion of the level-0 package did effect the final output signal.

A full model of the SOP was presented in Chapter 6. The encapsulation moulding compound was treated as an elastic material. Thermal cooldown analyses were done from the moulding temperature of 175°C to 4 different temperatures. These temperatures corresponded to those used when obtaining the experimental data. A purposely developed vector plot showed that the stress exerted on the level-0 package from the EMC was directed inwards towards the middle of the MEMS die. The electrical output signal from the transducer was compared to measurements at -7, 25, 75 and 125°C. The discrepancies were obvious and a number of reasons were given to explain them. A shift in the stress field on the silicon diaphragm was observed as a result of the stress from the EMC on the MEMS die.

Chapter 7 went one step further than Chapter 6 by treating the EMC as viscoelastic material. Previous work by other authors have only used the elastic approach. The viscoelastic material

data was obtained from stress relaxation experiments presented in Chapter 3. The material was assumed to be thermo rheologically simple, and the master stress relaxation curve and the corresponding shift function was obtained. The FEA using the new material model was again compared to measured results and a closer correspondence was found between these results than in the elastic case. Packaging stress plots also showed that the pressure exerted on the level-0 package was less in the viscoelastic case than for the elastic case. It was also found that the effect of thermocycling had a positive effect on decreasing packaging stress on the MEMS device.

Change in material properties and the influence this had on the FEA results were investigated in Chapter 8. It was found that changes in CTE changed the output signal, but not the sensitivity significantly. The opposite was found for a change in Poisson's ratio.

REFERENCES

[1] Catanescu, R. and Binder, J., Microsystem technologies'96, in: H. Reichel, A. Heuberger (Eds.), Fifth Int. Conf. and Exhibition on Micro Electro, Opto Mechanical Systems and Components, Potsdam, 1996, Vde-Verlag GMBH, Berlin, pp. 712-22

[2] Ko, W. H., Packaging of microsensors, in: H. Reichel, A. Heuberger (Eds.), Microsystem Technologies'94 4th Int. Conf. and Exhibition on Micro Electro, Opto Mechanical Systems and Components, Berlin, 1994, Vde-Verlag GMBH, Berlin, pp. 477-80

[3] Morrissey, A.; Kelly, G.; Alderman, J.; Barrett, J.; Lyden, C.; O'Rourke, L., "Some issues for microsystem packaging in plastic and 3D", *Microelectronics Journal,* Vol. 29, 1998, pp. 645-650

[4] Tilmans, H. A. C.; Fullin, E.; Ziad, H.; Van de Peer, M. D. J.; Kesters, J.; Van Geffen, E.; Bergquist, J.; Pantus, M.; Beyne, E.; Baert, K. and Naso, F.*,* " A fully packaged elecromagnetic Microrelay", *Proc. MEMS conference IEEE*, 1999

[5] Muller, L.; Hecht, M. H.; Miller, L. M.; Rockstad, H. K. and Lyke, J. C., "Packaging and qualification of MEMS-based space systems", *Proc. MEMS conference IEEE, 1996*

[6] Monk, D. J. and Shah, M. K., "Packaging and Testing Considerations of Bulk Micromachined,Piezoresistive Pressure Sensors", Motorola Sensor Product Division, Commercialization of Microsystems '96, pp.136-149, 1996

[7] Butler, J. T.; Bright, V. M. and Comtois, J. H., "multichip module packaging of microelectromechanical systems", *Sensors and Actuators,* A70, p. 15-22, 1998

[8] Malshe, A. P.; Brown, W. D.; Eaton, W. P. and Miller, W. M., "Challenges in the Packaging of MEMS", *The International Journal of Microcircuits and Electronic Packaging,* Vol. 22, No. 3, Third Quarter 1999 (ISBN 1063-1674)

[9] Beardmore, G., "Packaging for microengineered devices. Lessons from the real world", *Proc. Inst. Elec. Eng. Colloq. Assembly Connections Microsyst.,* London, U.K., 1997

[10] Brown, W. D., "Advanced Electronic Packagin: With Emphasis on Multichip Modules", *IEEE Press,* New York, p.3-8, 16-22, 35-41, 1999

[11] Monk, D. J.; Maudie, D.; Stanerson, J.; Wertz, J.; Bitko, G.; Matkin, J. and Petrovic, S., "Media Compatible Packaging and Environmental Testing of Barrier Coating Encapsulated Silicon Pressure Sensors", *Solid State Sensor and Actuator Workshop,* Hilton Head, South Carolina, June 2-6, p. 36-41, 1996

[12] Tilmans, H. A. C.; Van de Peer, M. D. J. and Beyne, E., "The Indent Reflow Sealing (IRS) Technique-A Method for the Fabrication of Sealed Cavities for MEMS Devices", *Journal of Microelectronical Systems,* Vol. 9, No. 2, June 2000

[13] Legtenberg, R. and Tilmans, H. A. C., "Electrostatically driven vacuum-encapsulated polysilicon resonators, Part I: Design and fabrication," *Sensors and Actuators,* vol. 45, p. 57-66, 1994

[14] Klanna, P. K.; Bhatnagar, S. K. and Gust, W., "Analysis of packaging and sealing techniques for microelectronic modules and recent advances," *Microelectronics International,* Vol. 16, no. 2, p.8-12, 1999

[15] Core, T. A.; Tsang, W. K. and Sherman, S. J., "Fabrication technology for an integrated surface-micromachined sensor," *Solid State Technology,* p. 39-47, Oct. 1993

[16] Legtenberg, R. and Tilmans, H. A. C., "Electrostatically driven vacuum-encapsulated polysilicon resonators, Part I: Design and fabrication," Sens. Actuators, vol. 45, pp. 57–66, 1994.

[17] Tilmans, H. A. C.; Fullin, E.; Ziad, H.; Van de Peer, M. D. J.; Kesters, J.; Van Geffen, E.; Bergqvist, J.; Pantus, M.; Beyne, E.; Baert, K. and Naso, F., "A fully packaged electromagnetic microrelay," in Proc. IEEE MEMS'99, Orlando, FL, pp. 25–30.

[18] Fujita, T.; Hatano, K.; Maenaka, K.; Mizuno, T.; Matsuoka, T.; Kojima, T.; Oshima, T. and Maeda, M., "Vacuum sealed silicon bulk micromachined gyroscopes," in Proc. 10th Int. Solid-State Sens. Actuators Conf., Sendai, Japan, 1999, pp. 914–917.

[19] Ziaie, B.; Von Arx, J.; Nardin, M. and Najafi, K., "A hermetic packaging technology with multiple feedthroughs for integrated sensors and actuators," in Proc. 7th Int. Solid-State Sens. Actuators Conf., Yokohama, Japan, 1993, pp. 266–269.

[20] Guckel, H., "Surface micromachined pressure transducers," Sens. Actuators, vol. 28, pp. 133–146, 1991.

[21] Rogge, B.; Moser, D.; Oppermann, H.; Paul, O. and Baltes, H., "Solderbonded micromachined capacitive pressure sensors," in Proc. SPIE Micromachined Devices Comp. IV Conf., vol. 3514, Santa Clara, CA, Sept. 1998, pp. 307–315.

[22] Tummala, R. R.; Rymaszewski, E. J. and Klopfenstein, A. G., Microelectronics Packaging Handbook. New York: Van Nostrand, 1989.

[23] Mack, S.; Baumann, H. and Gösele, U., "Gas tightness of cavities sealed by silicon wafer bonding," in Proc. IEEE MEMS'97 Nagoya, Japan, pp. 488–493.

[24] Gui, C.; Albers, H.; Gardeniers, J. G. E.; Elwenspoek, M. and Lambeck, P. V., "Fusion bonding of rough surfaces with polishing technique for silicon micromachining," Microsyst. Technol., pp. 122–128, 1997.

[25] Parameswaran, L.; McNeil, V. M.; Huff, M. A. and Schmidt, M. A., "Sealed-cavity microstructure using wafer bonding technology," in Proc. 7th Int. Solid-State Sens. Actuators Conf., Yokohama, Japan, 1993, pp. 274–277.

[26] Ando, D.; Oishi, K.; Nakamura, T. and Umeda, S., "Glass direct bonding technology for hermetic seal package," in Proc. IEEE MEMS'97 Nagoya, Japan, pp. 186–190.

[27] Caillat, P. and Nicolas, G., "Fluxless flip-chip technology," in 1st Int. Flip Chip Symp., Feb., San Jose, CA, 1994.

[28] Cohn, M. B.; Lang, Y.; Howe, R. T. and Pisano, A. P., "Wafer-to-wafer transfer of microstructures for vacuum packaging," in Proc. Solid-State Sens. Actuators Workshop Hilton Head, SC, 1996, June 2–6, pp. 32–35.

[29] Quenzer, H. J.; Benecke, W. and Dell, C., "Low temperature wafer bonding for micromechanical applications," in Proc. IEEE MEMS'92 Travemünde, Germany, pp. 49–55.

[30] Legtenberg, R. and Bouwstra, S., "Resonating microbridge mass flow sensor with low-temperature glass-bonded cap wafer," Sens. Actuators, vol. 25–27, pp. 723–727, 1991.

[31] Oh, K. W. and Ahn, C. H., "Development of an innovative flip-chip bonding technique using micromachined conductive polymer bumps," in Proc. Solid-State Sens. Actuator Workshop Hilton Head, SC, 1998, June 8–11, pp. 170–173.

[32] Estes, R. H., "Technology assessment: PFC® polymer flip chip solderless bump process," Epoxy Technol., Billerica, MA, Tech. Paper GB-31.

[33] Li, G. and Tseng, A., "Low Stress Packaging of a Micromachined Accelerometer", *IEEE Transactions on Electronics Packaging Manufacturing,* Vol. 24, No. 1, Jan 2001

[34] Billmeyer JR., F. W., "Textbook of Polymer Science", third edition, John Wiley &Sons, New York 1984

[35] Prime, R. B., *Thermal Characterization of Polymeric Materials,* Ed. Edith A. Turi, 2nd edition, Academic Press, San Diego, 1997

[36] Flory, P. J., *Principles of Polymer Chemistry,* Cornell University Press, Ithaca, NY (1953)

[37] Williams, M. L.; Landel, R. F. and Ferry, J. D., *J. Am. Chem. Soc.*, 77, 3701 (1955)

[38] Ferry, J. D., *Viscoelastic Properties of Polymers,* 3rd Edition, John Wiley and Sons, New York (1980)

[39] Wineman, A. S. and Rajagopal, K. R., *Mechanical Response of Polymers,* Cambridge University Press, 2000

[40] Rosen, S. L., *Fundamental Properties of Polymeric Materials,* John Wiley & Sons, New York (1982)

[41] Manzione, L. T., *Plastic Packaging of Microelectronic Devices,* Van Nostrand Reinhold, New York (1990)

[42] Bogetti, T. A. and J. W. Gillespie, "Process-Induced Stress and Deformation in Thick-Section Composite Laminates," *Journal of Composite Materials*, Vol. 26, No. 5., (1992)

[43] Ward, I. M. and D. W. Hadley, An Introduction to the Mechanical Properties of Solid Polymers, John Wiley and Sons, England, (1993).

[44] Findley, W. N.; Lai, J. S. and K. Onaran, Creep and Relaxation of Nonlinear Viscoelastic Materials: With an Introduction to Linear Viscoelasticity, Dover Publications, Inc., New York, (1989).

[45] Kamal, M. R. and Ryan, M. E., Chapter 4 in *Injection and Compression Molding Fundamantals*, A. I. Isayev, ed., New York: Marcel Dekker, (1987)

[46] Turng, L. S. and Wang, V. W., "On the Simulation of Microelectronic Encapsulation with Epoxy Molding Compound", *Journal of reinforced plastics and composites*, vol. 12, may 1993

[47] Wang, V. W.; Hieber, C. A. and Wang, K. K., "Dynamic simulation and graphics for the injection molding of three-dimensional thin parts", *Journal of Polymer Engineering,* vol. 7, no. 1, 1986

[48] Chiang, H. H.; Hieber, C. A. and Wang, K. K., "A Unified Simulation of the Filling and Postfilling Stages in Injection Molding. Part I: Formulation", *Polymer Engineering and Science*, vol. 31, no. 2, (1991)

[49] Hieber, C. A. and Shen, S. F., "A Finite-Element/Finite-Difference Simulation of the Injection-Molding Filling Process", *Journal of Non-Newtonian Fluid Mechanics*, vol. 7, p. 1-32, 1980

[50] Fleming, W. J., "Overview of Automotive Sensors", *IEEE Sensors Journal*, vol. 1, No.. 4, pp. 296-308, December 2001.

[51] Gong, S-C., and Lee, C., "Analytical Solutions of Sensitivity for Pressure Microsensors", *IEEE Sensors Journal*, vol. 1, No. 4, pp. 340-344, December 2001.

[52] Sze, S., Semiconductor Sensors, John Wiley Sons, Inc., 1994.

[53] Kanda, Y., "Graphical representation of piezoresis-tance coefficients in silicon", *IEEE Trans. Electron Devices*, ED-36, pp. 1295-1301, 1989.

[54] Timoshenko, S. and Woinowsky-Krieger, S., Theory of Plates and Shells, McGraw-Hill, 2nd Ed., 1959.

[55] Li, G. and Tseng, A. A., "Low Stress Packaging of a Micromachined Accelerometer", *IEEE Transactions on Electronics Packaging Manufacturing,* Vol. 24, No. 1, January 2001

[56] Kelly, G.; Lyden, C.; O' Mathuna C. and Cambell, J. S., "Investigation of Thermo-Mechanically Induced Stress in a PQFP 160 Using Finite Element Techniques", Proc. of Electronic Components and Technology Conference, (1992)

[57] Kawada, H. and Ikegami, K., "Viscoelastic Properties of Resin for IC Plastic Packages JSME International Journal, Series I, vol. 35, No. 2, (1992)

[58] Hong, B. Z. and Burrell, L. G., "Modeling Thermally Induced Viscoplastic Deformation and Low Cycle Fatigue of CBGA Solder Joints in a Surface Mount Package", InterSociety Conferance on Thermal Phenomena, (1996)

[59] Michael, M. and Nguyen, L., "Effect of Mold Compound Thermal Conductivity on IC Package Thermal Performance", InterSociety Conferance on Thermal Phenomena, (1992)

[60] Wright, R. E., Injection/Tansfer Molding of Thermosetting Plastics, Carl Hanser Verlag, Munich Vienna New York, 1995

[61] Pye, R. G. W, Injection Mould Design, John Wiely &Sons, Inc., New York, 1989

[62] Khazan, A. D., Transducers and Their Elements, PTR Prentice Hall, Englewood Cliffs, NJ, 1994

[63] Ochi, M.; Yamashita, K. and Shimbo, M., "The Mechanism for Occurence of Internal Stress during Curing Epoxide Resins", *Journal of Applied Polymer Science,* Vol. 43, 2013-2019 (1991)

[64] Romig, A. D.; Dressendorfer, P. V. and Palmer, D. W., "High performance microsystem packaging: A perspective.", *Microelecronics Reliability,* Vol. 37, No. 10/11, pp. 1771-1781, 1997

[65] Kelly, G.; Alderman, J. and Camon, H., "3-D Packaging Methodologies for Microsystems", *IEEE Transactions on Advanced Packaging,* Vol. 23, No. 4, Nov. 2000

[66] Reichi, H. and Grosser, V., "Overviev and development trends in the field of mems packaging.", *The 14th IEEE International Conference on Micro Electro Mechanical Systems,* 2001

[67] Kelly, G.; Lyden, C.; Lawton, W. and Barrett, J., "Accurate Prediction of PQFP Warpage", *Publication source unknown*

[68] Kelly, G.; Lyden, C.; Lawton, W.; Barrett, J.; Saboui, A.; Pape, H. and Peters, J. B., "Importance of Molding Compound Chemical Shrinkage in the Stress and Warpage Analysis of PQFP's", *IEEE Transactions on Components, Packaging and Manufacturing Technology-PART B,* Vol. 19, No. 2, May 1996

[69] Wang, J. and Liu, S., "Sequential Processing Mechanics Modeling for a Model IC Package", *IEEE Transactions on Components, Packaging, and Manufacturing Technology-PART C,* Vol. 20, No. 4, Oct. 1997

[70] Chew, S., "Thermal And Viscoelastic Characterization Of Transfer-Molded Epoxy Encapsulant During Simulated Post-Mold Cure", *IEEE Electronic Components and Technology Conference,* pp. 1032-1038, 1996

[71] Maehara, D. and Ikegami, K., "Temperature Dependence of Viscoelastic Deformation of Resin for Plastic Packaging", *JSME International Journal*, Series A, Vol. 38, No. 2, 1995

[72] CINDAS, SRC Document, Purdue University, Lafayette, IN, 1999

[73] Tucker, C. L., Fundamentals of Computer Modeling for Polymer Processing, Hanser Publishers, Munich Vienna New York, 1989

[74] Tummala, R. R.; Rymaszewski, E. J. and A. G. Klopfenstein, Microelectronics Packaging Handbook, Part II, 2nd ed., Norwell, Chapman & Hall, 1997.

[75] Dealy, J. M. and Wissbrun, K. F., Melt Rheology and its role in Plastics Processing, Kluwer Academic Publishers, Dordrecht, 1999

[76] Barnes, H. A; Hutton, J. F. and Walters, K., An introduction to Rheology, Elsevier Science B. V., Amsterdam, 1998

[77] Castro, J. M. and Macosko, C. W., AIChe J., 28, 250, 1982

[78] Castro, J. M., PhD Thesis, Univ. Minnesota, 1980

[79] Lekakou, C. N. and Richardson, S. M., "Simulation of Reacting Flow During Filling in Reaction Injection Molding (RIM)", *Polymer Engineering and Science,* Vol. 26, No. 18, pp. 1264-1275, 1986

[80] Harper, B. D.; Lu, L. and Kenner, V. H., "Effects of Temperature and Moisture upon the Mechanical Behaviour of an Epoxy Moulding Compound", *Advances in Electronic Packaging*, Vol. 19-1, ASME, 1997

[81] Kenner, V. H.; Julian, M. R.; Popelar, C. H. and Chengalva, M. K., "Viscoelastic Characterization of an Epoxy-Based Moulding Compound", *Material Research Society Symposium Proceedings,* Vol. 390, 1995

[82] Dudek, R., Vogel, D. and Michel, B., "Mechanical Failure in COB-technology Using Glob-top Encapsulant," *IEEE Trans. Components, Pack. Manufact. Tech. C*, vol. CP-MTC-19, pp. 232-240, Oct. 1996

[83] Narayanaswamy, O. S., "A Model of Structural Relaxation in Glass", *Journal of the American Ceramic Society*, Vol. 54, No. 10, pp. 491-498, 1971

[84] Wortman, J. J., "Young's modulus, shear modulus and Poisson's ratio in Silicon and Germaium," *Journal of Applied Physics,* vol. 36, p. 153, 1965

[85] Daniel, I. M. and Ishai, O., Engineering Mechnics of Composite Materials, Oxford Univ Press (1994)

[86] Matsuda, K., Suzuki, K., Yamamura, K and Kanda, Y., "Nonlinear piezoresistance effects in silicon", *Journal of Applied Physica,* 73(4), pp. 1838-1847, (1993)

[87] Krondorfer, R. H. and Ullvensøen, J. H., "Simulation of Transfer Molding", *Proc. of 38th IMAPS Annual Conference,* Oslo, pp. 304-310, 2001

[88] Krondorfer, R. H. and Lommasson, T. C., "Direct Calculation of Sensor Performance in a FEA Model," *Proc. 1st Sensors Conf.,* Orlando, FL, pp. 2013-2019, June 2002.

[89] Krondorfer, R. H., Kim, Y. K. and Lommasson, T. C., "FEA simulation of package stress in transfer molded MEMS pressure sensors", *Proc. of EuroSIME2003,* Aix-en-Provence, France, pp. 165-169, 2003

APPENDIX A

MEASUREMENT RESULTS FOR BARE DIE

Table A.1: Measurement results for Die 1.

Temperature (ºC)	Pressure (kPa)	Signal (mV)
117.2	70	5.878
99.8	70	6.499
75.7	70	7.292
25.5	70.1	8.781
-8.4	70.2	9.651
97.7	99.9	7.197
74.3	99.9	7.999
117.5	100	6.511
104.9	100	6.944
64.5	100	8.306
25.5	100	9.496
-7.9	100	10.387
84.6	100.1	7.641
22.6	100.2	9.519
-9.9	183.5	12.616
-6.8	999.9	33.098
116	1000	25.054
72.7	1000	27.882
26	1000	30.927
95.1	1000.1	26.424
26	1999.9	54.432
-6.7	1999.9	58.006
92.8	2000	47.648
113.6	2000.1	45.594
71.2	2000.1	49.794
111.3	3000	66.024

Table A.1: Measurement results for Die 1.

90.7	3000	68.737
-6.6	3000	82.535
69.8	3000.1	71.489
26	3000.2	77.581

Table A.2: Measurement results for Die 2.

Temperature (ºC)	Pressure (kPa)	Signal (mV)
75.7	69.9	-7.201
117.3	70	-8.04
99.7	70	-7.676
25.5	70.1	-6.476
-8.4	70.2	-6.314
117.5	99.9	-7.414
97.7	99.9	-6.986
104.9	100	-7.148
74.3	100	-6.499
25.5	100	-5.765
-7.9	100	-5.563
84.7	100.1	-6.719
64.5	100.1	-6.328
22.6	100.1	-5.827
-9.8	183.5	-3.364
115.9	999.9	11.416
-6.9	999.9	17.619
95.1	1000	12.495
72.7	1000	13.685
26	1000	16.052
-6.7	1999.9	42.971
92.8	2000	34.035
71.2	2000	35.944
113.6	2000.1	32.258
26	2000.3	39.975
111.2	3000	52.992
69.8	3000	57.996
26	3000	63.533

Table A.2: Measurement results for Die 2.

90.6	3000.1	55.43
-6.6	3000.1	67.863

Table A.3: Measurement results for Die 3.

Temperature (°C)	Pressure (kPa)	Signal (mV)
75.7	69.9	-0.997
99.7	70	-1.745
117.3	70.1	-2.296
25.5	70.1	0.445
-8.3	70.1	1.038
117.5	100	-1.662
105	100	-1.265
97.7	100	-1.032
74.3	100	-0.274
64.6	100	0.014
25.5	100	1.158
-7.9	100	1.78
84.7	100.1	-0.613
22.7	100.1	1.099
-9.8	183.5	3.949
115.9	999.9	17.227
72.7	999.9	19.981
95.1	1000	18.526
26	1000.1	23
-6.9	1000.1	24.934
92.7	2000	40.142
71.1	2000	42.309
-6.7	2000	50.333
113.5	2000.1	38.141
26	2000.1	46.958
111.2	2999.9	58.951
90.6	2999.9	61.604
69.8	2999.9	64.407
26	3000	70.529
-6.6	3000.1	75.26

Table A.4: Measurement results for Die 4.

Temperature (ºC)	Pressure (kPa)	Signal (mV)
75.7	69.9	-9.125
99.7	70	-10.938
25.5	70	-6.405
117.3	70.1	-12.47
-8.3	70.1	-5.409
117.4	100	-11.831
105	100	-10.721
97.6	100	-10.1
74.3	100	-8.35
25.5	100	-5.641
-7.9	100	-4.67
84.7	100.1	-9.095
64.6	100.1	-7.735
22.7	100.1	-5.571
-9.7	183.5	-2.262
115.8	999.9	7.566
95	999.9	10.057
72.6	999.9	12.513
26	1000	16.89
-6.9	1000.3	19.262
113.5	2000	29.084
92.7	2000	32.314
71.1	2000	35.498
26	2000	41.624
-6.7	2000	45.405
90.5	2999.9	54.421
69.8	2999.9	58.247
26	2999.9	65.943
-6.6	2999.9	71.149
111.1	3000	50.514

Table A.5: Measurement results for Die 5.

Temperature (ºC)	Pressure (kPa)	Signal (mV)
75.6	69.9	-3.092
117.3	70	-4.519
99.6	70	-3.898
-8.3	70	-0.937
25.5	70.1	-1.667
117.4	99.9	-3.916
105	99.9	-3.478
97.6	100	-3.219
74.2	100	-2.412
25.5	100	-0.978
22.7	100	-1.049
-7.9	100	-0.209
84.7	100.1	-2.775
64.6	100.1	-2.127
-9.7	183.5	1.8
72.6	999.8	16.562
95	1000	15.118
115.8	1000.1	13.793
25.9	1000.1	19.459
-6.9	1000.3	21.453
71.1	1999.9	37.487
113.5	2000	33.419
26	2000	41.899
92.7	2000.1	35.394
-6.7	2000.1	45.182
26	2999.8	63.999
111.1	3000	52.959
-6.6	3000	68.523
69.7	3000.1	58.217
90.5	3000.3	55.533

Table A.6: Measurement results for Die 6.

Temperature (ºC)	Pressure (kPa)	Signal (mV)
75.6	69.9	5.286
99.6	70	4.571
-8.3	70	7.373
117.4	70.1	4.042
25.5	70.1	6.785
117.4	100	4.689
105	100	5.069
97.6	100	5.298
25.5	100	7.524
22.8	100	7.578
-7.9	100	8.134
84.7	100.1	5.693
74.2	100.1	6.023
64.6	100.1	6.312
-9.6	183.5	10.377
72.6	999.8	26.718
94.9	1000	25.282
25.9	1000.1	29.85
-6.9	1000.1	31.802
115.8	1000.2	23.992
71.1	2000	49.514
26	2000	54.331
-6.7	2000	57.65
113.4	2000.1	45.355
92.6	2000.1	47.357
90.5	2999.9	69.249
111.1	3000	66.598
69.7	3000	72.072
-6.6	3000	83.027
26	3000.5	78.448

Table A.7: Measurement results for Die 7.

Temperature (ºC)	Pressure (kPa)	Signal (mV)
75.6	69.9	9.533
-8.3	69.9	11.41
99.6	70	8.85
117.4	70.1	8.335
25.5	70.1	10.847
105	99.9	9.325
117.4	100	8.954
97.5	100	9.547
84.7	100	9.927
74.2	100	10.239
25.5	100	11.544
22.8	100	11.555
-7.9	100	12.159
64.6	100.1	10.497
-9.6	183.5	14.473
72.5	999.8	30.128
94.9	1000	28.752
-6.9	1000	34.911
115.7	1000.1	27.506
25.9	1000.1	32.982
113.4	2000	48.035
71	2000	52.052
-6.7	2000	59.894
92.6	2000.1	49.966
26	2000.1	56.522
111	2999.9	68.488
90.4	2999.9	71.053
69.7	2999.9	73.751
-6.6	2999.9	84.401
26	3000.4	79.688

Table A.8: Measurement results for Die 8.

Temperature (ºC)	Pressure (kPa)	Signal (mV)
75.6	69.9	2.7
-8.3	69.9	6.224
99.5	70	1.753
117.4	70.1	1.072
25.5	70.1	4.853
117.4	99.9	1.713
105	99.9	2.206
84.7	100	3.025
25.5	100	5.608
22.8	100	5.745
-7.9	100	7.027
97.5	100.1	2.506
74.2	100.1	3.458
64.6	100.1	3.866
-9.5	183.5	9.37
-6.9	999.9	30.837
115.7	1000	21.2
94.8	1000	22.692
72.5	1000	24.364
25.9	1000	28.099
113.3	1999.8	42.761
-6.7	1999.8	56.854
92.5	1999.9	44.976
25.9	2000	52.823
71	2000.1	47.38
111	2999.9	64.23
-6.6	2999.9	82.546
90.4	3000	67.092
69.6	3000	70.147
26	3000	77.068

APPENDIX B

SIGNAL VALUES FROM PROCESS VARIATION STUDY

Table 9.1: Calculated signal values for Case 1 [*mV/V*]

Temperature (C) / Pressure (kPa)	-7.5	25	75	125
0	0.40	0.55	0.63	0.60
1000	6.73	6.23	5.54	4.93
2000	13.06	11.91	10.44	9.25
3000	19.39	17.59	15.34	13.57
Sensitivity [µV/V/kPaµV/V/kPa]	6.33	5.68	4.91	4.33

Table 9.2: Calculated signal values for Case 2 [*mV/V*]

Temperature (C) / Pressure (kPa)	-7.5	25	75	125
0	0.40	0.54	0.63	0.60
1000	6.84	6.32	5.62	5.00
2000	13.27	12.10	10.60	9.39
3000	19.70	17.86	15.58	13.79
Sensitivity [µV/V/kPa]	6.43	5.77	4.99	4.40

Table 9.3: Calculated signal values for Case 3 [*mV/V*]

Pressure (kPa) \ Temperature (C)	-7.5	25	75	125
0	0.39	0.54	0.62	0.59
1000	6.69	6.19	5.50	4.89
2000	12.98	11.84	10.38	9.19
3000	19.28	17.48	15.25	13.49
Sensitivity [μV/V/kPa]	6.29	5.65	4.88	4.30

Table 9.4: Calculated signal values for Case 4 [*mV/V*]

Pressure (kPa) \ Temperature (C)	-7.5	25	75	125
0	0.39	0.53	0.61	0.58
1000	6.85	6.33	5.62	5.00
2000	13.30	12.12	10.62	9.41
3000	19.75	17.91	15.62	13.81
Sensitivity [μV/V/kPa]	6.45	5.79	5.00	4.41

Table 9.5: Calculated signal values for Case 5 [*mV/V*]

Pressure (kPa) / Temperature (C)	-7.5	25	75	125
0	0.35	0.48	0.55	0.53
1000	6.72	6.20	5.49	4.88
2000	13.08	11.91	10.42	9.23
3000	19.44	17.61	15.35	13.57
Sensitivity [µV/V/kPa]	6.36	5.71	4.93	4.35

Table 9.6: Calculated signal values for Case 6 [*mV/V*]

Pressure (kPa) / Temperature (C)	-7.5	25	75	125
0	0.38	0.53	0.61	0.58
1000	6.53	6.04	5.37	4.78
2000	12.67	11.56	10.13	8.97
3000	18.82	17.07	14.89	13.17
Sensitivity [µV/V/kPa]	6.14	5.51	4.76	4.20

Table 9.7: Calculated signal values for Case 7 [*mV/V*]

Pressure (kPa) / Temperature (C)	-7.5	25	75	125
0	0.40	0.54	0.63	0.60
1000	6.80	6.29	5.59	4.97
2000	13.20	12.03	10.55	9.34
3000	19.59	17.77	15.50	13.71
Sensitivity [μV/V/kPa]	6.40	5.74	4.96	4.37

Table 9.8: Calculated signal values for Case 8 [*mV/V*]

Pressure (kPa) / Temperature (C)	-7.5	25	75	125
0	0.35	0.49	0.56	0.53
1000	6.64	6.13	5.43	4.83
2000	12.92	11.76	10.30	9.12
3000	19.20	17.39	15.16	13.41
Sensitivity [μV/V/kPa]	6.28	5.64	4.87	4.29

Table 9.9: Calculated signal values for Case 9 [*mV/V*]

Pressure (kPa) / Temperature (C)	-7.5	25	75	125
0	0.37	0.50	0.58	0.55
1000	10.35	9.46	8.31	7.37
2000	20.32	18.40	16.03	14.18
3000	30.29	27.34	23.75	20.98
Sensitivity [μV/V/kPa]	9.97	8.95	7.72	6.81

Table 9.10: Calculated signal values for Case 10 [*mV/V*]

Pressure (kPa) / Temperature (C)	-7.5	25	75	125
0	0.35	0.48	0.56	0.53
1000	4.25	3.98	3.58	3.19
2000	8.14	7.47	6.60	5.86
3000	12.03	10.97	9.61	8.52
Sensitivity [μV/V/kPa]	3.89	3.49	3.02	2.66

APPENDIX C

MEASUREMENTS RESULTS FOR EMC PACKAGED DIE

Table C.1: Measurement results for Die 1.

Temperature (°C)	Pressure (kPa)	Signal (mV)
123.2	70	3.867
122.3	100	3.865
120.3	1000.1	18.779
117.9	2000	34.989
115.3	3000	50.659
109.2	100	-10.044
99.1	70	-24.381
97	100	-26.747
94.4	1000	-12.452
92.1	2000	4.274
89.9	3000	21.381
84.2	100	-39.325
75.7	70	-47.529
74.3	100	-48.045
72.8	999.9	-30.966
71.4	2000	-11.794
70	2999.9	7.405
65.2	100	-56.208
24.8	70.1	-103.806
24.9	100.1	-102.92
25.8	1000.1	-80.432
26.2	2000.1	-56.646
26.5	3000.1	-33.182
23.8	99.9	-104.824
-10.6	69.1	-157.56
-9.6	100.1	-154.803

Table C.1: Measurement results for Die 1.

-7.2	1000	-126.849
-6.6	2000.1	-99.945
-6.4	3000	-74.098
-9	100.2	-153.93

Table C.2: Measurement results for Die 2.

Temperature (°C)	Pressure (kPa)	Signal (mV)
123.2	70	7.111
122.3	100	6.904
120.3	1000	20.152
117.8	2000	34.852
115.3	2999.9	49.294
109.2	100	-10.022
99.1	70	-26.275
96.9	100	-28.973
94.4	999.9	-15.23
92	2000	1.136
89.8	3000.1	17.965
84.2	100	-41.917
75.7	70	-49.509
74.3	99.9	-49.784
72.8	999.9	-32.816
71.3	1999.9	-13.68
70	3000	5.462
65.2	100	-55.619
24.8	70	-93.2
24.9	100.1	-92.378
25.8	1000.1	-70.805
26.1	2000.1	-47.609
26.5	2999.8	-24.73
23.8	99.9	-93.251
-10.6	68.7	-132.349
-9.6	100.1	-129.859
-7.2	999.8	-103.92
-6.6	2000.1	-77.932

Table C.2: Measurement results for Die 2.

-6.5	3000	-52.883
-9	100.1	-128.568

Table C.3: Measurement results for Die 3.

Temperature (ºC)	Pressure (kPa)	Signal (mV)
123.2	70	-25.561
122.3	100	-25.606
120.3	1000	-11.355
117.8	2000	4.372
115.2	3000	19.841
109.2	100	-42.669
99	70	-57.951
96.9	100	-60.589
94.3	1000	-46.242
92	1999.9	-29.368
89.8	3000	-12.079
84.2	100	-73.317
75.6	70	-80.346
74.2	100	-80.491
72.8	999.9	-62.894
71.3	2000	-43.269
69.9	3000	-23.637
65.2	100	-86.01
24.8	69.9	-119.75
24.9	100.1	-118.947
25.8	999.9	-96.861
26.1	2000	-73.254
26.5	2999.9	-49.945
23.9	99.9	-119.85
-10.7	68.9	-155.751
-9.6	100.1	-153.605
-7.2	999.9	-127.116
-6.7	2000.1	-100.753
-6.5	3000.1	-75.211
-8.9	100.1	-152.59

Table C.4: Measurement results for Die 4.

Temperature (°C)	Pressure (kPa)	Signal (mV)
123.2	70	-25.926
122.2	100	-26.082
120.2	999.9	-12.501
117.7	2000	2.582
115.2	3000	17.377
109.2	100	-42.889
99	70	-58.936
96.8	100	-61.776
94.3	1000	-48.234
91.9	2000	-32.056
89.8	3000	-15.461
84.2	100	-76.741
75.6	70	-83.515
74.2	99.9	-83.876
72.7	1000	-66.96
71.3	2000	-47.98
69.9	2999.9	-28.983
65.3	100	-91.17
24.8	69.9	-133.822
24.9	100.1	-132.978
25.8	999.9	-111.28
26.1	1999.9	-88.059
26.5	3000	-65.183
23.9	99.9	-134.595
-10.7	69.2	-178.132
-9.6	100.1	-175.682
-7.2	999.9	-149.186
-6.7	2000	-123.287
-6.5	3000	-98.194
-8.9	100.1	-174.692

Table C.5: Measurement results for Die 5.

Temperature (°C)	Pressure (kPa)	Signal (mV)
123.2	70	14.475
122.2	100	14.551

Table C.5: Measurement results for Die 5.

120.2	999.9	28.998
117.7	2000	44.214
115.2	3000.1	58.951
109.2	100	0.473
99	70	-13.138
96.8	100	-15.46
94.2	1000	-1.656
91.9	2000	14.5
89.7	2999.9	31.092
84.2	100	-29.003
75.6	70	-36.759
74.2	99.9	-37.163
72.7	1000.1	-20.327
71.2	2000	-1.503
69.9	3000	17.368
65.3	100	-44.842
24.8	69.9	-88.279
24.9	100.1	-87.405
25.8	999.9	-65.568
26.1	1999.9	-42.38
26.4	2999.9	-19.468
23.9	99.9	-89.27
-10.7	69.6	-137.931
-9.5	100.1	-135.423
-7.3	1000.1	-108.297
-6.7	2000.9	-82.209
-6.5	3000	-57.048
-8.9	100.1	-134.71

Table C.6: Measurement results for Die 6.

Temperature (°C)	Pressure (kPa)	Signal (mV)
123.2	70	13.122
122.2	100	13.026
120.1	1000.1	26.509
117.6	2000	41.025
115.1	3000	55.033

Table C.6: Measurement results for Die 6.

109.2	100	-4.27
98.9	70	-20.55
96.8	100	-23.48
94.2	1000	-10.558
91.8	2000.1	4.838
89.7	3000.1	20.753
84.2	100	-40.695
75.6	70	-50.582
74.1	99.9	-51.372
72.7	1000	-35.062
71.2	2000.1	-16.743
69.9	3000	1.665
65.3	100	-61.585
24.8	69.8	-116.151
24.9	100	-115.289
25.8	1000	-93.432
26.1	2000	-70.311
26.4	3000	-47.434
23.9	99.9	-117.973
-10.7	70	-175.606
-9.5	100.1	-172.844
-7.3	1000	-145.381
-6.7	2000	-119.351
-6.5	3000	-94.251
-8.9	100.1	-172.522

Table C.7: Measurement results for Die 7.

Temperature (ºC)	Pressure (kPa)	Signal (mV)
123.2	70	11.327
122.1	100	11.286
120.1	1000.1	26.971
117.6	2000	43.941
115.1	2999.9	60.252
109.2	100	-2.756
98.9	70	-16.565
96.7	100	-18.858

Table C.7: Measurement results for Die 7.

94.1	1000.1	-3.851
91.8	2000.1	13.74
89.6	3000.2	31.698
84.2	100	-32.474
75.6	70	-40.958
74.1	99.9	-41.622
72.6	1000.1	-23.672
71.2	2000	-3.525
69.8	3000.1	16.644
65.3	100	-50.654
24.8	69.8	-98.162
24.9	100	-97.254
25.8	999.9	-73.888
26.1	1999.9	-49.13
26.4	3000	-24.754
23.9	99.9	-99.583
-10.7	70.2	-150.921
-9.5	100.1	-148.15
-7.3	1000	-119.514
-6.7	1999.9	-91.907
-6.5	2999.9	-65.166
-8.9	100.1	-147.924

Table C.8: Measurement results for Die 8.

Temperature (°C)	Pressure (kPa)	Signal (mV)
123.2	70	22.413
122.1	100	22.332
120	1000	36.848
117.6	2000	52.689
115	2999.9	67.93
109.1	100	5.709
98.9	70	-10.6
96.7	100	-13.501
94.1	1000	0.265
91.8	1999.9	16.717
89.6	3000	33.788

Table C.8: Measurement results for Die 8.

84.2	100	-31.466
75.5	70	-42.657
74.1	99.9	-43.78
72.6	1000.1	-26.581
71.1	2000	-7.061
69.8	3000	12.638
65.3	100	-56.112
24.8	69.9	-118.549
24.9	100	-117.638
25.7	999.9	-94.153
26.1	1999.9	-69.496
26.4	2999.9	-45.107
24	100	-120.817
-10.6	70.5	-185.398
-9.5	100.1	-182.524
-7.3	1000	-152.923
-6.7	2000.1	-125.193
-6.5	3000	-98.53
-8.8	100.1	-182.373

APPENDIX D

STRESS PLOTS FOR ALL CONSIDERED TEMPERATURES

This appendix shows contour stress plots for all the temperatures, comparing 1 and 6 thermo-cycles.
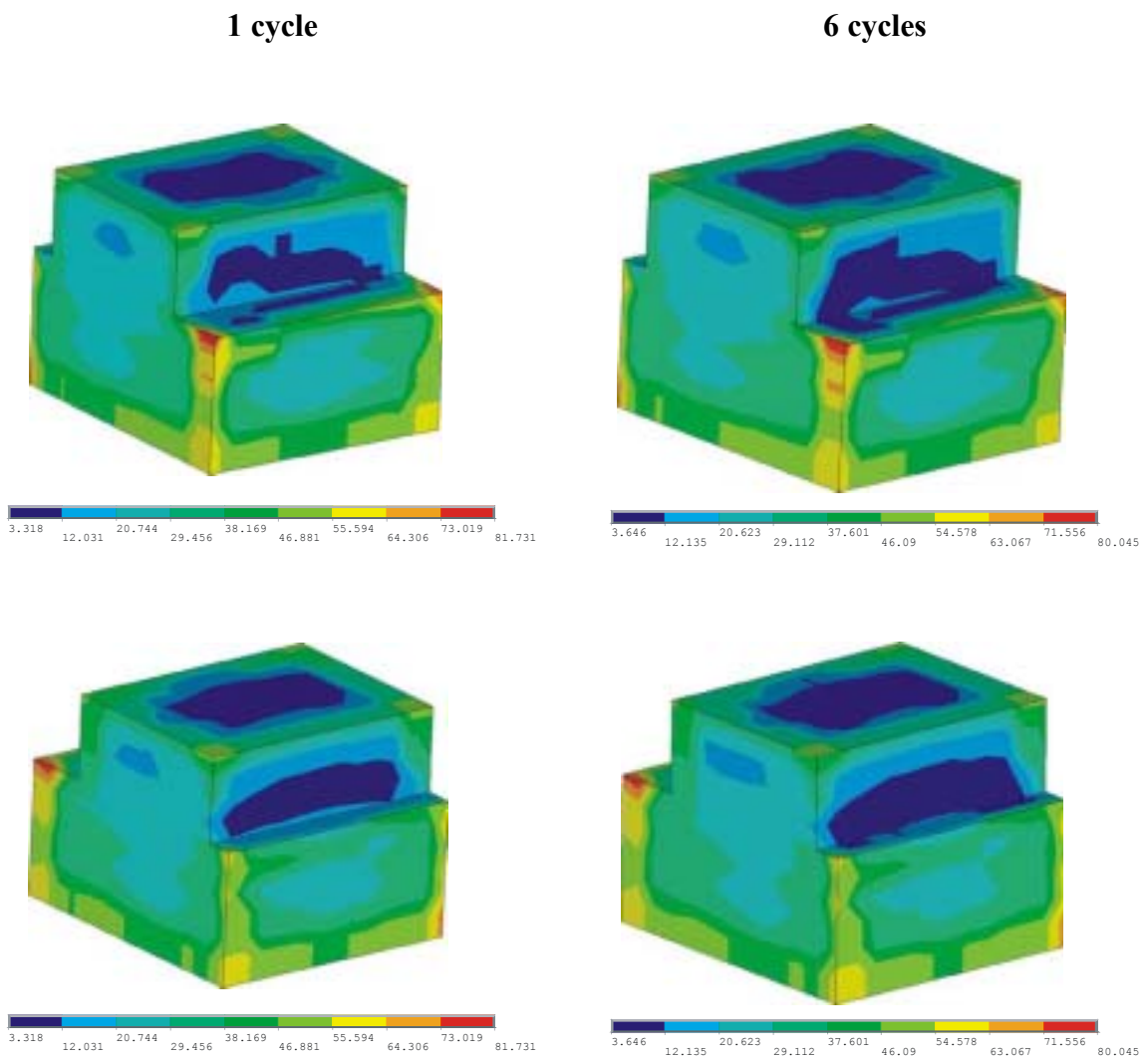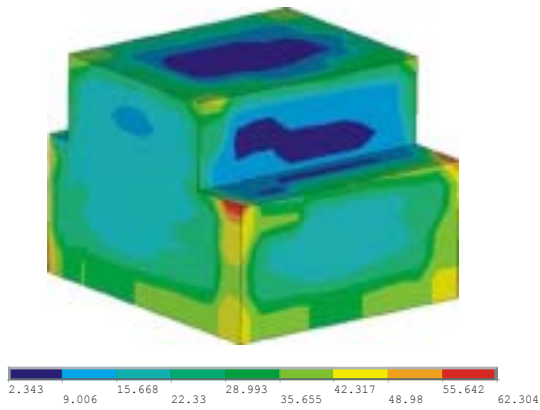
1 cycle   **6 cycles**
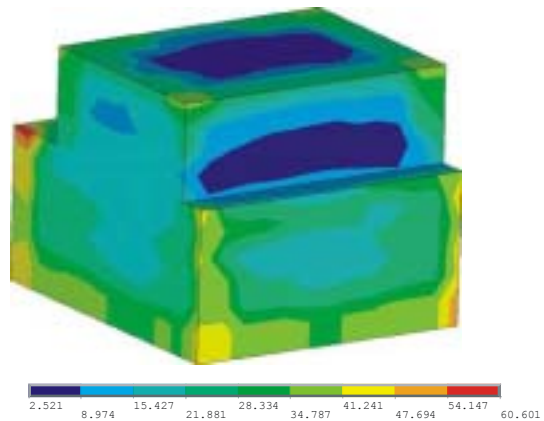

Figure D.1   -7°C

1 cycle   **6 cycles**
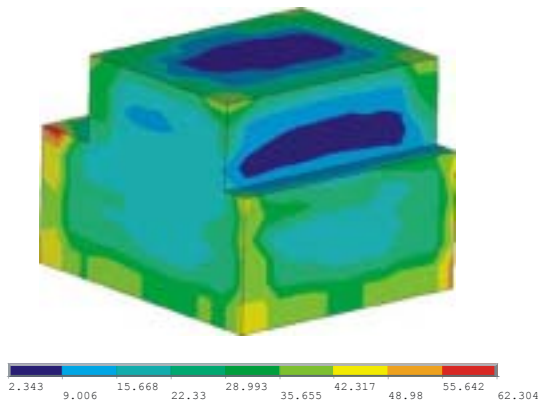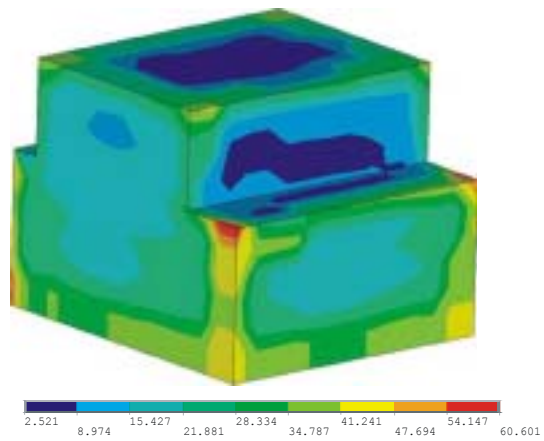
Figure D.2   25°C
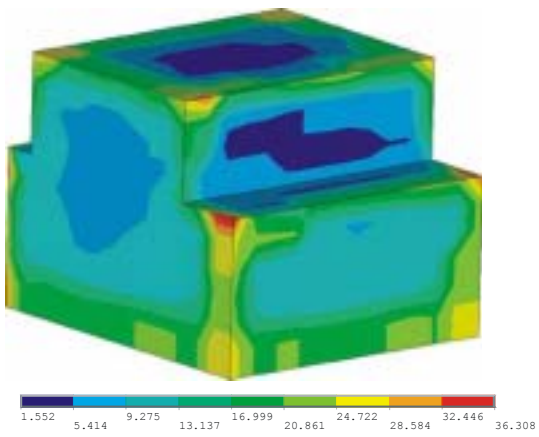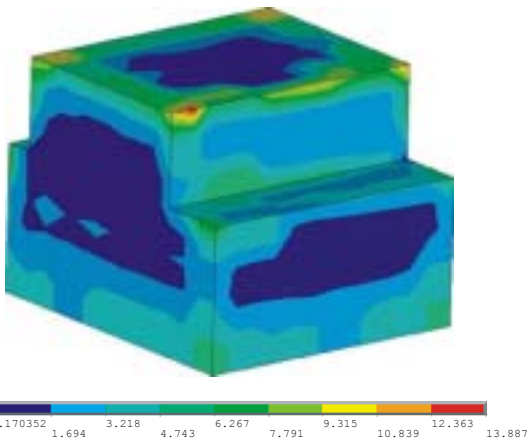
1 cycle
                      6 cycles
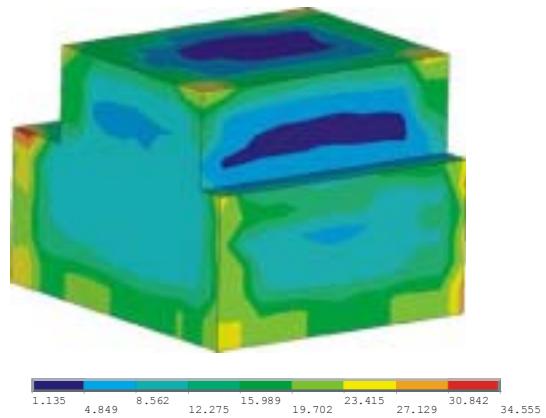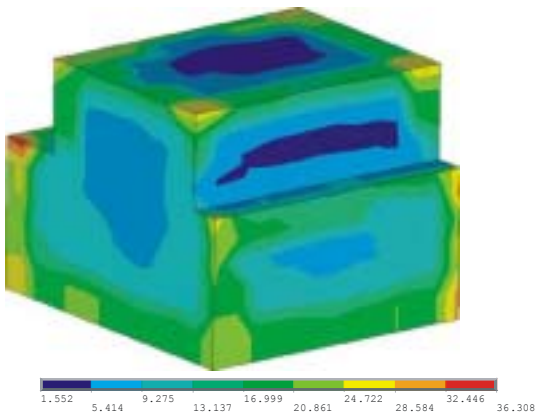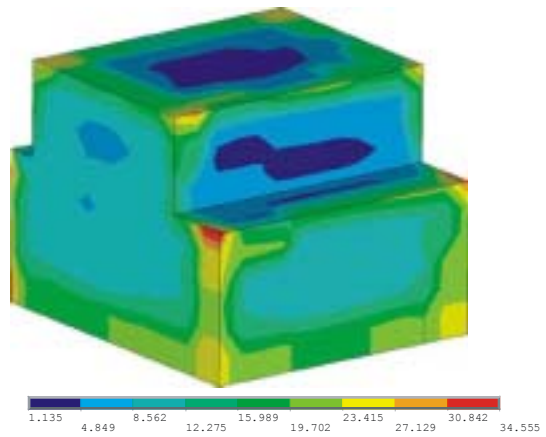
Figure D.3   75°C

1 cycle   **6 cycles**
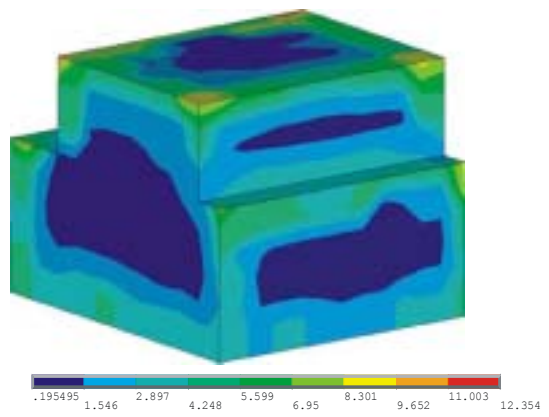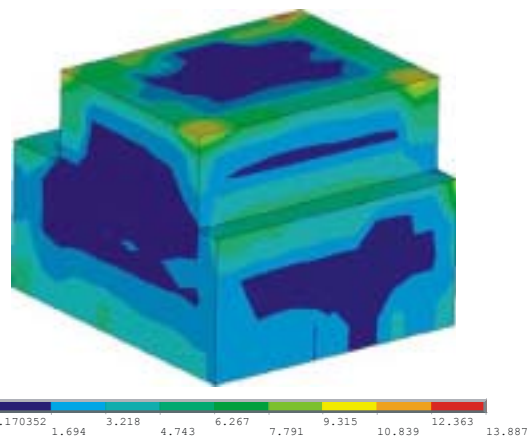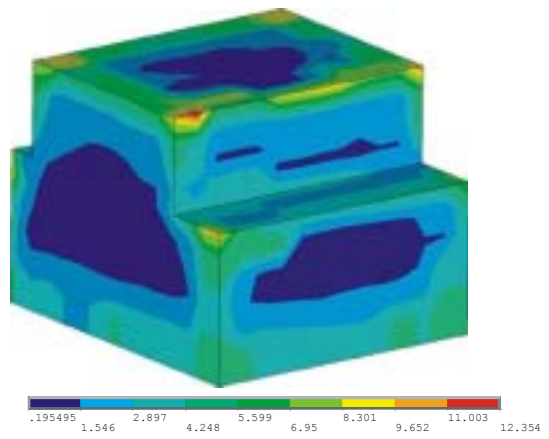
Figure D.4   125°C

APPENDIX E

MDMS FOR THE EMC USED IN THIS WORK

```
|----------------------------------------------+-----------------------|
| Tit EPOXY RESIN TABLET MP 7410 TA TABLET     | MSDS No. MSDS -0548   |
| le:                                          | Revision: 2           |
|----------------------------------------------+-----------------------|
```

```
|---------------------+---------------------+---------------------|
| Department:         |  Approved & Released |                     |
| Quality Assurance Dept|  Material Safety Data |                   |
|                     |         Sheet        |                     |
| Area:               |                      |                     |
|                     |                      |                     |
|---------------------+---------------------+---------------------|
```

Section 1: Product and Company Identification:
```
|----------------------------------+----------------------------------|
|   Search product                 | Chemical Name:                   |
| MP 7410 TA                       | EPOXY RESIN TABLETS              |
|                                  | Q3 MOLDING COMPOUNDS HC100-MP190/ |
|                                  | 7+8000                           |
|----------------------------------+----------------------------------|
```

```
|----------------------------------------------------------------------
|
| Product Use.                                                        |
| Epoxy molding compound for IC.                                      |
|----------------------------------------------------------------------
```

Section 2: Composition Information on Ingredients

A.Substances which give the product its health-risk properties:
```
|----------------------------------------------------------------------
|
| According to the European Directive 91/155/EEC, this product is a harmful|
| preparation .                                                       |
|----------------------------------------------------------------------
|
```

```
|-------------+--------------+-------------+-----------+-------------|
| Ingredient: | CAS No.      | % Weight:   |  Symbol   | R-phrase    |
|-------------+--------------+-------------+-----------+-------------|
| Antimony    | 1309-64-4    | 1,2 %       |Xn         |R40, R52, R53|
```

trioxide					
Carbon black	1333-86-4	< 1 %			
Fused silica	60676-86-0	60-95 %			
Crystalline silica	14808-60-7	< 5 %			

B.Other substances:

Ingredient:	CAS No.	% Weight:	Symbol	R-phrase
Solid epoxy resin		2-20 %		
Brominated epoxy resin		0,6 %		
Phenol resin		2-20 %		
Amine		< 1.5 %		
Phosphorous		< 1.5 %		